ABSTRACT

Title of thesis: EFFECTS OF BODY SHAPES
ON ROTOR IN-GROUND-EFFECT AERODYNAMICS

Benjamin Thomas Hance, Master of Science, 2012

Thesis directed by: Professor J. Gordon Leishman
Department of Aerospace Engineering

Videographic flow visualization and two-component particle image velocimetry (PIV) measurements were performed to examine the developing vortical wake produced by a two-bladed hovering rotor at a height of one rotor radius above a horizontal ground plane. The experiments were performed with an isolated rotor and with three different bodies placed in the wake below the rotor. The bodies examined had circular, elliptical, and rectangular cross-sections, respectively. Flow measurements were taken in planes that covered the nose and tail region of each body. The objective of the study was to gain a better understanding of the nature of the flow at the ground plane and to assess the overall effects of a body in the rotor wake, and in particular to document the nature of the unsteady, turbulent boundary layer flow over the ground. The flow visualization and PIV were performed using a Nd:YAG laser that illuminated a radial plane of the flow, with imaging performed with a CCD camera. Measurements of the spatial locations of the tip vortices as a function of wake age were obtained to quantify the wake distortion produced by each body shape. The outward flow over the ground plane was shown to have similar characteristics to a classical turbulent wall-jet; these similarities were especially apparent

further downstream on the ground plane away from the rotor. The results showed that the flow over the nose of each of the bodies was similar to that of the isolated rotor, but with some minor differences in the flow at the ground. The slipstream boundary was shown to be severely disrupted by the tail of each body, and showed larger variations from that produced by the isolated rotor. Wake impingement on the body was shown to cause catastrophic bursting of the blade tip vortices. The body with a rectangular cross-section was generally found to produce the greatest differences in the overall flow characteristics near the ground plane compared to that of the isolated rotor. The work has relevance to the better understanding the problem of rotorcraft brownout, where the near-wall flow drives the mobilization and uplift of dust.

EFFECTS OF BODY SHAPES ON ROTOR IN-GROUND-EFFECT AERODYNAMICS

by

Benjamin Thomas Hance

Thesis submitted to the Faculty of the Graduate School of the
University of Maryland, College Park in partial fulfillment
of the requirements for the degree of
Master of Science
2012

Advisory Committee:
Professor J. Gordon Leishman, Chair/Advisor
Associate Professor James Baeder
Professor Roberto Celi

Acknowledgments

First I would like to thank my advisor and thesis committee chair, Professor J. Gordon Leishman, for giving me the chance to work on this project. Working in the lab as a Graduate Research Assistant has been a wonderful learning opportunity.

I would like to thank Associate Professor James Baeder and Professor Roberto Celi for their contributions as members of my thesis committee.

I would additionally like to thank the U.S. Air Force Office of Scientific Research, who supported this work under a Multi-Disciplinary University Research Initiative, Grant No. FA9550-08-1-0406. Dr. Douglas Smith was the contract monitor.

I'd like to thank all the guys in the lab for all their work and help. Special thanks to Joe Milluzzo for assisting in the experiments, and to Nick Amen and Grant Barrett for all of the "grunt" work. Additional thanks to David Mayo, Joseph Ramsey, and Anish Sydney for welcoming me to the team and showing me the ropes. Thanks to Ajay Baharani, Bharath Govidarajan, and Jürgen Raulader for their help and friendship.

I want to thank my good friends Pratik Bhandari and Mark Glucksman-Glaser for their encouragement and for sharing the graduate school experience with me.

I want to give my deepest thanks to my parents Bruce and Debbie, my brother Cody, and my wonderful fiancée Rosa for their unending love and support. I would not have made it this far without you.

Table of Contents

List of Figures

Nomenclature

A	Rotor disk area, πR^2, m^2 or ft^2
C_{F_b}	Vertical force coefficient on body, $F/\rho A\Omega^2 R^2$
C_P	Rotor power coefficient, $P/\rho A\Omega^3 R^3$
C_{P_0}	Profile power coefficient, $P_0/\rho A\Omega^3 R^3$
C_T	Rotor thrust coefficient, $T/\rho A\Omega^2 R^2$
c	Rotor blade chord, m or ft
F_b	Vertical load on body, lb
M	Image magnification factor
N_b	Number of blades
P	Measured rotor power, lb fts^{-1} or hp
R	Radius of blade, m or ft
r	Radial distance downstream from rotor shaft axis, m or ft
Re_{tip}	Tip chord Reynolds number, $\rho V_{\text{tip}} c/\mu$
T	Rotor thrust, lb
$\overrightarrow{U}$	Instantaneous flow velocity, ms^{-1}
$\overline{U}$	Average flow velocity, ms^{-1}
u	Velocity in the r direction, ms^{-1}
$u_\star$	Friction velocity, $\sqrt{\tau_w/\rho}$
v	Velocity in z direction, ms^{-1}
V_{tip}	Blade tip speed, ms^{-1}
z	Vertical distance above the ground, m or ft

Γ_w Total wake strength, $\mathrm{ft}^2\mathrm{s}^{-1}$

Δt Pulse separation time, s

ΔU Uncertainty in flow velocity, ms^{-1}

ΔV Velocity excursion from average, ms^{-1}

Δx, Δy Grid spacing, m

$\Delta\varepsilon_M$ Uncertainty in magnification factor

$\Delta\varepsilon_{\Delta t}$ Uncertainty in pulse separation time, s

$\Delta\varepsilon_{\Delta x}$ Uncertainty in pixel displacement, m

θ_0 Blade collective pitch, deg

θ_{tw} Linear blade twist rate, deg

κ Induced power factor

μ Dynamic viscosity, $\mathrm{kg\ m}^{-1}\mathrm{s}^{-1}$

ν Kinematic viscosity, $\mathrm{m}^2\mathrm{s}^{-1}$

ρ Flow density, $\mathrm{kg\ m}^{-3}$

σ Rotor solidity, $N_b c/\pi R$

τ_w Wall shear stress, $\mu\left(\frac{\partial u}{\partial z}\right) \mid_{z \to 0}$

ψ_b Blade azimuth angle, deg

Ω Rotational speed of the rotor, $\mathrm{rad\ s}^{-1}$

ζ Wake age, deg

Abbreviations

CCD	Charge Coupled Device
DAQ	Data Acquisition
FFT	Fast Fourier Transform
fps	Frames-Per-Second
FV	Flow Visualization
PIV	Particle Image Velocimetry

Chapter 1

Introduction

1.1 Preamble

Understanding the aerodynamic characteristics of a rotor operating in-ground-effect (IGE) has been the subject of significant research over many years, and the overall behavior is now well understood from the perspective of performance. However, recently there has been interest in gaining an understanding of the behavior of the detailed flow structures near that ground that are produced by a rotor when operating IGE. In particular, recent research has focused on how the flow beneath the rotor affects the mobilization of dust particles as it influences the problem of "brownout." Brownout is characterized by the onset of a blinding dust cloud that occurs when a rotorcraft lands or takes off over surfaces covered in loose material such as sand. However, there is currently very little work that has quantitatively examined the nature of the rotor flow field at the ground, and even less work that has examined the effect of placing a body (such as a fuselage or airframe) in the flow below the rotor. To this end, two main questions arise: Does the shape of a body beneath the rotor affect the evolution of flow structures near the ground? If so, will the effects obtained also influence the mobilization of dust, and hence the problem of brownout?

1.2 The Rotor In-Ground-Effect

When a rotorcraft enters ground effect, its rotor wake is significantly distorted by the proximity of the ground, as shown in Fig. 1.1. As a consequence of this wake distortion, the inflow velocities and angles of attack at the rotor blades are altered, which results in reductions in the power required for the rotor to produce a given thrust. These effects generally become more prominent as the rotor comes closer to the ground. Studies focusing on measuring and calculating the performance or a rotor in-ground-effect [1–6] have found that rotors at heights of less than one rotor diameter can experience significant benefits in terms of overall performance. In general, rotors operating at low enough heights above the ground to alter the rotor aerodynamic performance are defined as operating in-ground-effect (IGE). Rotors operating away from the ground in clean air conditions are defined as operating out-of-ground-effect (OGE)

Knight and Hefner [1] performed the first systematic study of the thrust and torque characteristics of a rotor operating in ground effect. Cheeseman and Bennett [2] documented the decreases in the benefit of ground-effect with increasing forward airspeed. Hayden [3] summarized the power decreases that were noted in flight test data for a variety of helicopters that were operating IGE. However, there has been far less work done towards the goal of understanding the fluid dynamics of a rotor operating IGE, including the flow field produced near the ground [7–14]. It is toward this end that the present research is directed.

Even less work has been done to investigate the nature of the rotor wake IGE as it interacts with a surface covered by loose sediment or dust, i.e., to simulate the problem

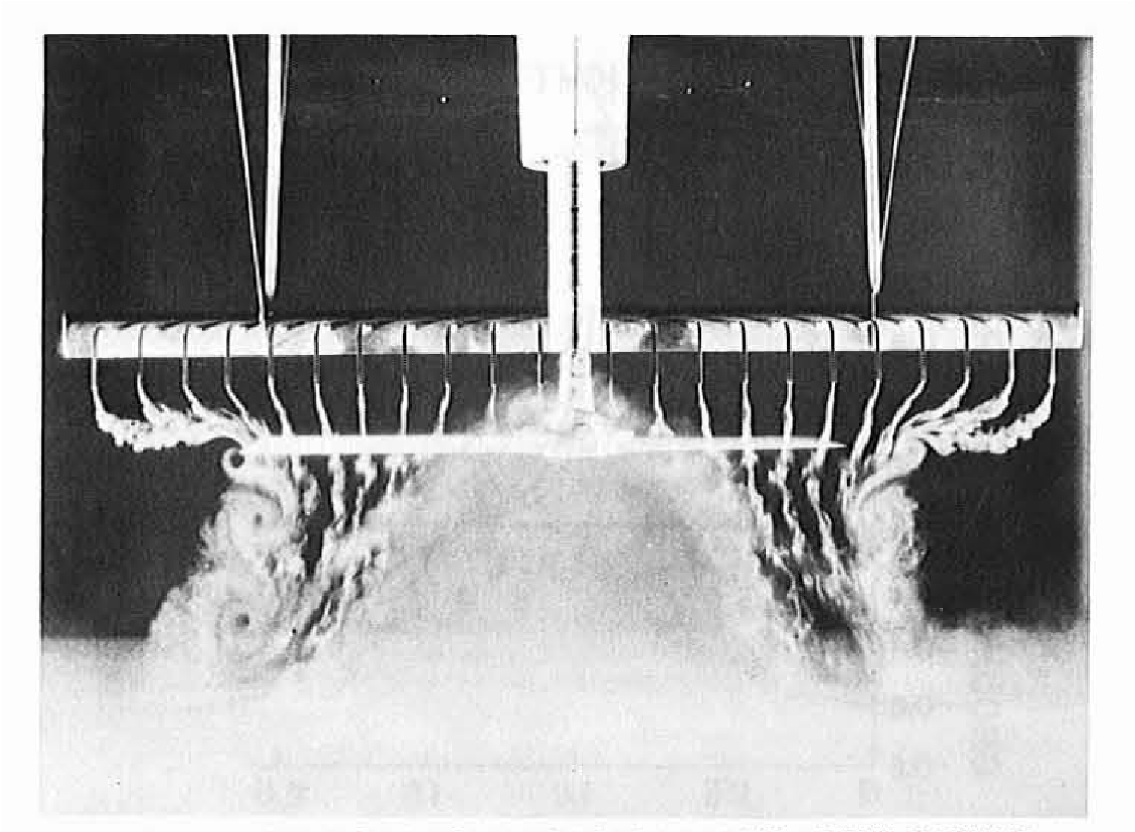

Figure 1.1: An example of the flow visualization of a rotor when operating IGE as performed by Fradenburgh [4].

of brownout [15, 16]. It is now known [16] that the action of the vortical aspects of the rotor wake as it impinges on the ground is fundamental to the mobilization of sediment particles, the uplift of dust, and the creation of brownout conditions. Therefore, to develop a better understanding of the problem of brownout, a prerequisite is to understand the evolution and dynamics of the rotor wake as it approaches and interacts with the ground. While many aspects of the rotor design that can affect the detailed structure of the rotor wake, the present work focuses on the aerodynamics a simple two-bladed rotor operating in the presence of a bluff body that represents a fuselage of a helicopter that is situated in the wake below the rotor.

Smoke flow visualization of the wake of a laboratory-scale rotor operating OGE is shown in Fig. 1.2, which is taken from Ref. [10]. This image shows a radial plane through the wake below the rotor. The flow was seeded with smoke and a thin laser sheet was used to illuminate the flow with the blade locked to a given azimuthal position. Visible in this image are the blade tip vortices, the turbulent vortex sheets from the inner parts of the blades, and the slipstream boundary that demarcates the rotor wake from the more quiescent outer flow. The blade tip vortices follow the path of the slipstream boundary for two to three rotor revolutions before significant diffusion of the vorticity occurs. As the far wake expands, the tip vortices increasingly diffuse their vorticity and become more turbulent. Eventually, the downstream wake becomes more like a turbulent jet.

Figure 1.3 shows the same rotor when it is operated in IGE conditions. As for the OGE case, the slipstream boundary experiences an initial contraction in the near field immediately below the rotor. However, because of the presence of the ground, the slipstream boundary is turned rapidly to flow in a more radial direction away from the rotor and more

parallel to the ground. The wake then becomes a radially expanding turbulent jet. Furthermore, when the rotor is operated IGE, the tip vortices do not become significantly diffused until six to eight rotor revolutions after their creation, and much longer than for when the rotor operates in OGE conditions. Previous work [17, 18] has found that as the wake of a rotor approaches a ground plane, the tip vortex filaments are stretched and their vorticity is reintensified. This stretching process can reduce, balance, or even counter the normal diffusion of vorticity. The vortices then tend to persist in the flow to relatively older wake ages. While there has been a recent increase in research focusing on the understanding the fluid dynamics of a rotor wake under IGE conditions [10–13, 15, 16], there is still much to learn about the details of the flow environment there.

A schematic of the flow field of a rotor operating IGE is shown in Fig. 1.4. The trailed tip vortices significantly affect the flow near the rotor, and potentially have large influences on blade loads and rotor performance. In addition to the generation of unsteady airloads and rotor noise [19, 20], the tip vortices can also cause rotor-airframe interactions [21–23]. Studies of the near-field flow of the rotor wake have been performed [24–36], much of it focused on documenting the structure of the blade tip vortices [37–42]. However, there is a dearth of information on the structure of the rotor wake at significantly older wake ages, and very little information on the detailed action of the rotor wake upon the ground, which is highly relevant to the problem of brownout.

Lee et al. [10] have recently investigated the flow generated by a small-scale rotor operating at different heights above a ground plane. This work described the evolution of the wake and the dynamics of the tip vortices as they interacted with the ground plane. A preliminary analysis of the development of the wall-jet flow was also given. Milluzzo et

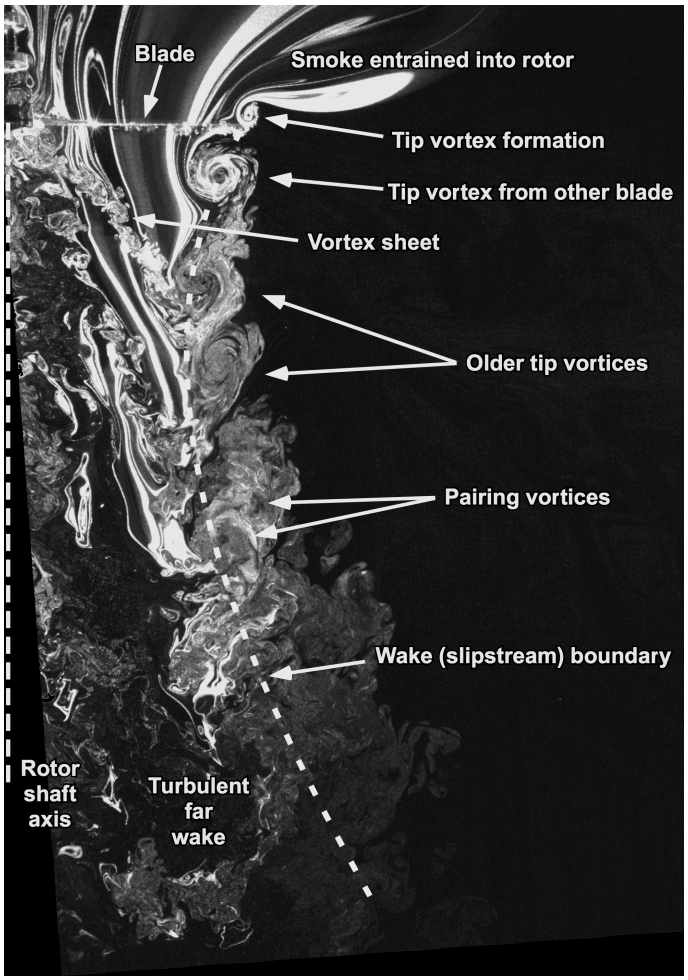

Figure 1.2: Representative flow visualization of a 2-bladed rotor wake when operating OGE [10].

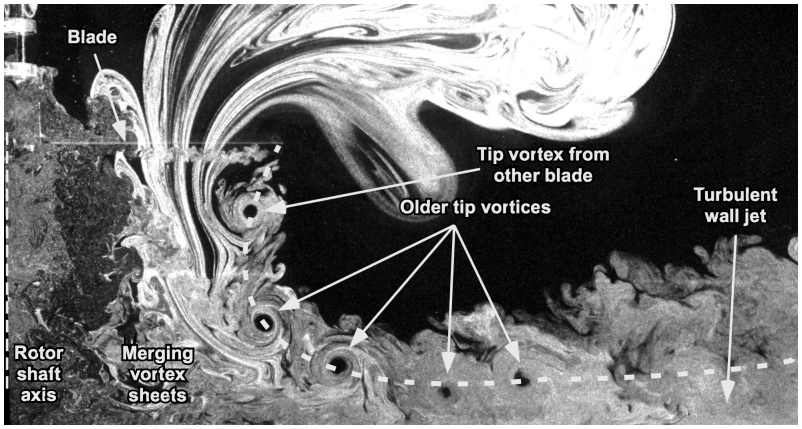

Figure 1.3: Representative flow visualization of a 2-bladed rotor wake when operating IGE [10].

al. [11] further explored the evolution of the blade tip vortices for a rotor in IGE conditions and also for different blade tip shapes. The core size and velocity profiles of the tip vortices were measured, as well as the effect that the tip shape had on the velocity profiles at the ground plane. However, few studies have investigated, as the present study does, the detailed interactions of the rotor wake and the ground when there is a fuselage or body present in the flow below the rotor.

1.3 Effect of a Body on a Rotor In-Ground-Effect

Previous work has examined the effects that the presence of a bluff body in the rotor wake may have in terms of rotor performance [4, 9]. In particular, Fradenburgh [4] made performance measurements of rotors operating in both IGE and OGE. This work examined the changes in performance experienced by rotors as they were brought closer to a ground plane. In addition, Fradenburgh compared the performance of rotors operating IGE with and without a body (in this case a circular disk) placed in the rotor wake. These

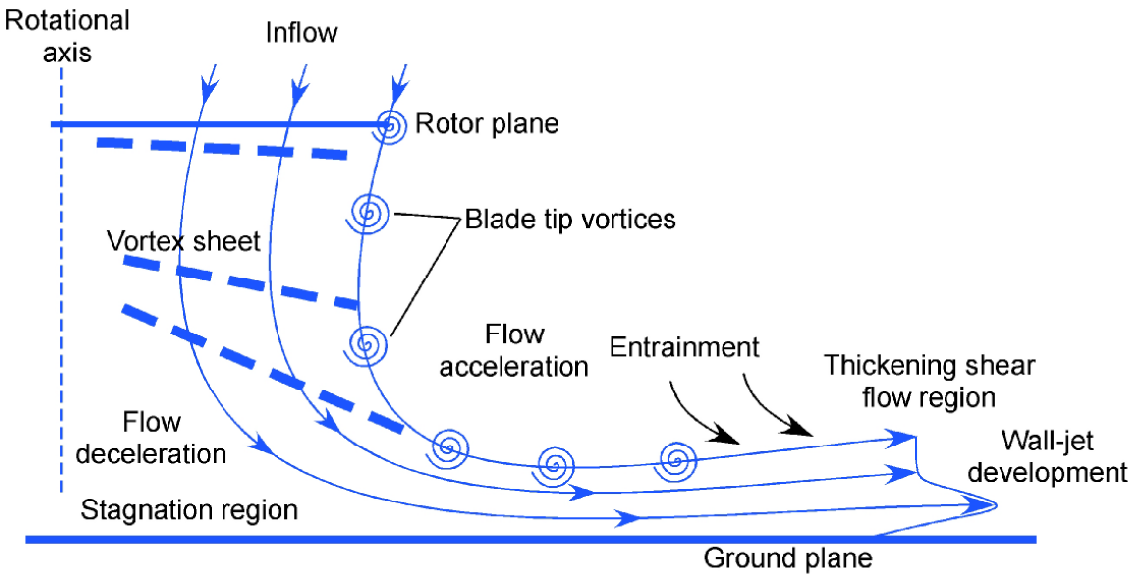

Figure 1.4: A schematic of the rotor wake for hover in IGE conditions.

studies showed that the presence of an object in the rotor wake can augment the benefits of ground effect through a so-called "thrust recovery effect." When a rotor and body are operated out of ground effect, the vertical drag on the body produces a net down-force that counters the thrust of the rotor. However, at lower heights above the ground, the body will begin to produce a net upward thrust or thrust recovery effect that can augment the thrust produced by the rotor itself; see Fig. 1.5. The reason for this behavior is because of the disruption of the separated wake below the body by the ground plane. While Fradenburgh made some flow visualization of the rotor wake (see Fig. 1.1 for an example), no quantitative measurements of the flow field were made.

Prior work has shown the wake below a rotor to be rather complicated [10, 11, 15–17] because of the presence of various vortical flow structures, including the tip vortices and regions of turbulence; see Fig. 1.4. It is reasonable to assume that the addition of a body below the rotor will further alter the flow field, and will potentially have a large

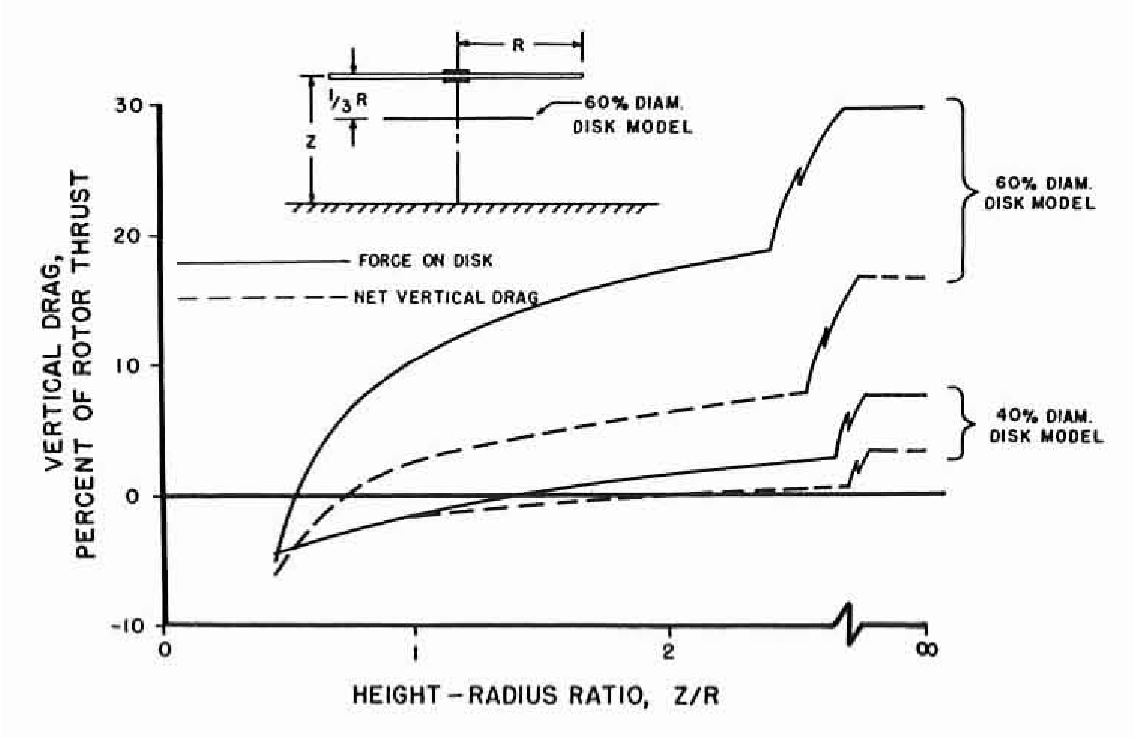

Figure 1.5: A plot of the vertical drag on a circular disk under a rotor at various heights off a ground plane [4].

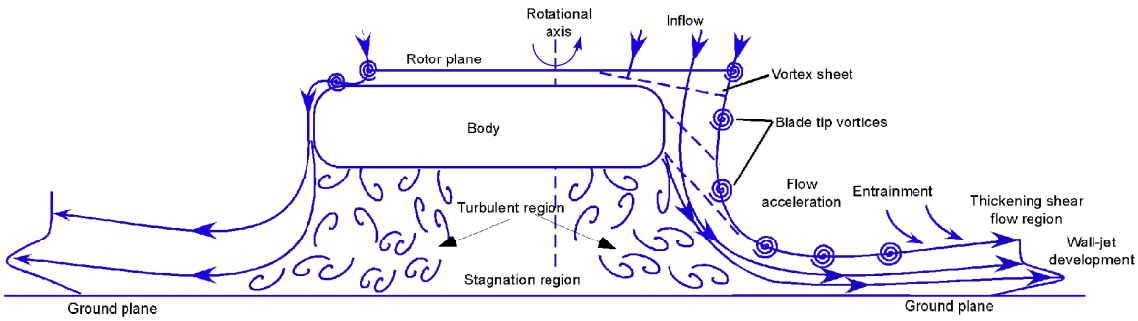

Figure 1.6: Schematic of the wake of a rotor and body when operating IGE.

effect on the development of the flow. In the schematic in Fig. 1.6, it can be seen that the presence of the body may distort the slipstream boundary of the rotor flow, and also change the trajectories of the tip vortices. On the left of the schematic, the body extends beyond the radius of the rotor. In this case, the slipstream boundary may be significantly distorted and it is likely that the blade tip vortices will impinge directly upon the body. The wake of the body may also create regions of eddies and turbulence of greater intensity than those produced by the rotor itself

1.4 Problem of Rotorcraft Brownout

The phenomenon of "brownout" occurs when rotorcraft operate over unprepared ground surfaces that are covered in loose sediment such as sand. When the rotorcraft flies close enough to the ground such that the rotor wake impinges on the surface, the fluid dynamic forces there can be sufficient to cause sediment particles to be mobilized and uplifted, culminating in the rapid development of a dense dust cloud. In this context, "dust" refers to small sediment particles that are more easily suspended.

An example of a helicopter encountering brownout conditions during a landing in

Figure 1.7: A helicopter generating a brownout dust cloud while landing in the desert. (Image courtesy of Optical Air Data Systems LLC.)

the desert is shown in Fig. 1.7. As the brownout dust cloud develops, it can interfere with the pilot's ability to see the ground, as well as creating spurious sensory cues and vection (i.e., apparent motion) illusions. In particular, the sudden loss of visual references can pose a serious safety of flight risk. It has been reported that brownout is the leading cause of human-factor related mishaps during military operations [43]. Civil rotorcraft have also been reported to suffer from the problem of brownout when operating over unprepared surfaces [44], especially during MEDEVAC operations.

There have been several recent attempts [45–49] to mitigate the problem of brownout, although none have yet addressed the problem from the perspective of rotorcraft design. Pilots have developed strategies to reduce the severity of the problem, including flying closer to the ground at higher airspeeds to outpace the developing dust cloud, or using an

increased rate of descent to land before the dust cloud can fully form. These operational strategies may, however, require the pilot to perform unsafe maneuvers and execute a hard landing, and in practice they have served to mitigate brownout only to a limited extent.

While the factors responsible for creating different brownout cloud intensities is still the subject of research, it is the fluid dynamics of the rotor wake that are directly responsible for the production of the brownout dust cloud. The rotor wake in terms of its strength and structure is known to vary depending on parameters such as number of rotors, blade number, blade twist, blade tip shape, fuselage shape, and rotor height off the ground. However, definitive conclusions on the sensitivities of these parameters are difficult to draw because of a dearth of really useful measurements of rotorcraft experiencing actual brownout conditions. While Refs. [47–49] provide at least some results on the topic, the lack of comprehensive quantitative measurements still makes it difficult to understand the physical mechanisms that underlie the brownout problem.

Attempts have still been made to understand why some rotorcraft generate more intense brownout signatures than others. Milluzzo and Leishman [50] have investigated the effect of rotor operating conditions on the relative severity of the brownout dust cloud. For example, Fig. 1.8 shows how average downwash velocity of the rotor is related to the total wake strength. This figure also shows three regions of severity of brownout, which were determined by a subjective assessment of photographic and videographic evidence of rotorcraft experiencing actual brownout conditions. Because the total wake strength is a consequence of several factors, including blade chord, radius, blade number, blade loading coefficient, and rotational tip speed, all of these parameters can, ultimately, affect the problem of brownout.

Figure 1.9 shows a schematic that summarizes the fluid dynamic processes involved in the phenomenon of brownout. Particles will become mobilized if the forces that result from the rotor flow interacting with the sediment bed become greater than those forces caused by interparticle cohesiveness and weight. While significant previous work has been done on wind-driven sands and riverine flows with the purpose of identifying the mechanisms responsible for sediment mobility [52–54], only recently have studies begun to examine the flow field beneath a rotor to investigate how sediment mobility and uplift may differ from the wind-driven environment [15, 16]. In particular, Sydney et al. [16] has identified several fluid dynamic mechanisms below a rotor that are pertinent to the development of brownout conditions.

Another effect, and one not considered by Milluzzo and Leishman [50], is that the shape of the airframe may also affect the flow and the ground and hence the development of brownout conditions. Heavy-lift cargo and transport rotorcraft often have fuselages with relatively bluff, rectangular cross-sections that can produce significant turbulent wakes in the slipstream of the rotor. Most helicopters, however, tend to have narrower and more elliptical fuselages, and would be expected to produce wakes that less disturb the overall flow. Nevertheless, the effects of the fuselage shape on the flow near the ground and problem of brownout, at least at this point, is unknown. The present work addresses some of these issues by making detailed flow measurements near the ground.

From these foregoing studies, it is now known that the structure and composition of the vortical rotor wake has a significant influence on the uplift of sediment particles. Specifically, the development of a radial flow along the ground influences the initial mobilization of the particles, while a majority of particle uplift and entrainment is caused

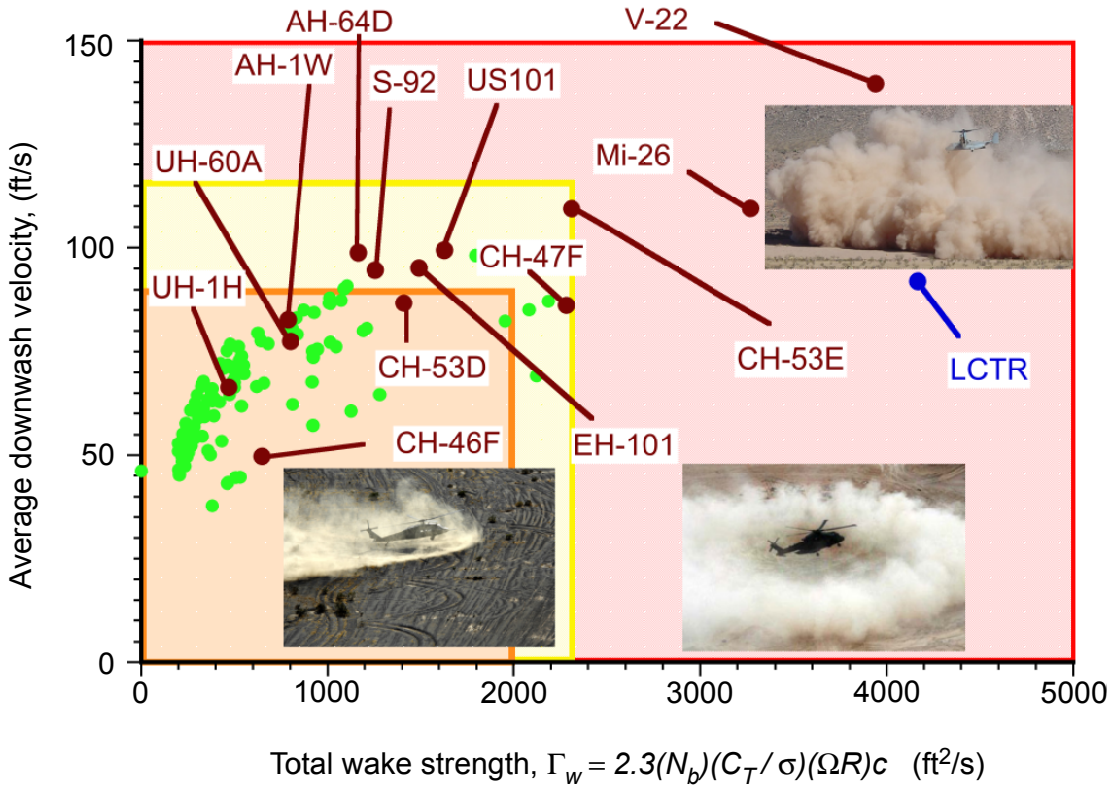

Figure 1.8: Severity of brownout as a function of downwash velocity and total wake strength. (From Milluzzo [51]. Cleared for public release.)

by the action of the tip vortices. If these uplifted particles remain uplifted long enough, they may be reingested by the rotor. Once this occurs, the rotor wake bombards the particles back onto the sediment bed, ejecting many more particles in the process and rapidly causing more severe brownout conditions [55].

1.5 Objectives of the Present Work

The goal of the present research was to perform a detailed investigation of the fluid dynamic environment of a rotor wake interacting with a ground plane and, more specif-

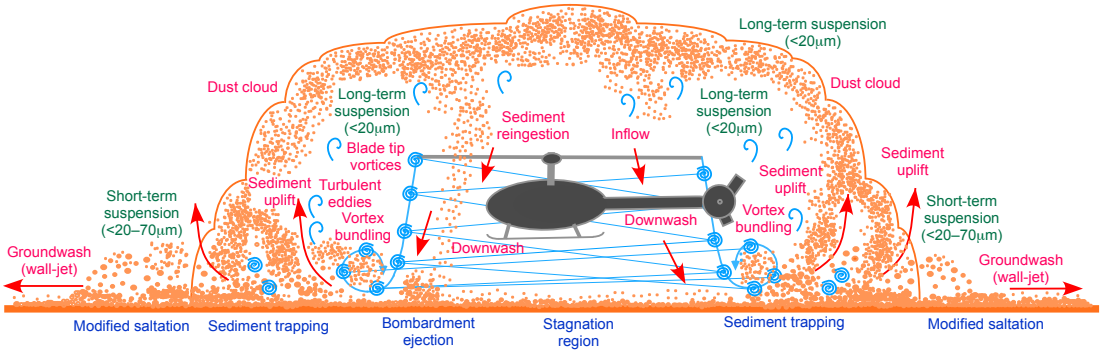

Figure 1.9: Schematic showing the fluid dynamic mechanisms and modes of sediment particle motion produced by the rotor wake from a helicopter hovering over a sediment bed.

ically, to examine the effect that the presence of a bluff body beneath the rotor would have on the resulting flow field. The primary goal of the study was to investigate the fluid dynamics of the wake produced by a rotor operating in-ground-effect. Specifically, the work examined the alterations to the structure of the rotor wake and the flow at the ground that were caused by the introduction of a body into the flow below the rotor.

Three body shapes with different cross-sections, but representative of those used on contemporary helicopters, were examined in comparison to the baseline case without a body in the flow. A detailed study of the flow was undertaken using particle image velocimetry with a two-bladed rotor system operating in-ground-effect at one rotor radius above a ground plane. Planar cuts were made in the region beneath the rotor, and discretized into specific regions of interest so that the flow could be examined in the near-field of the rotor and at various wake ages as it convected toward the ground plane.

1.6 Organization of Thesis

This introductory chapter has introduced the fluid dynamic aspects of a rotor operating in ground effect conditions and also the closely connected problem of rotorcraft brownout. A summary of prior research work on the two problems has also been given. Chapter 2 gives a description of the experimental set up used in the present research, and the techniques that were used to acquire the flow and performance measurements. Detailed descriptions of the principles of flow visualization and phase-resolved PIV are given. Chapter 2 also explains the technical challenges that were experienced during the experiments, and how these challenges were addressed. Chapter 3 discussed the experimental results, focusing on the characterization of the flow field and the presentation of the flow measurements, especially near the ground. Finally, Chapter 4 discusses the conclusions that were drawn from the present study, and also suggests future experiments to improve the understanding of the aerodynamic flow fields generated by rotors in-ground-effect conditions.

Chapter 2

Description of the Experiments

2.1 Introduction

To gain a better understanding of the flow below a rotor operating in-ground-effect and in proximity to a bluff body, phase-resolved flow visualization (FV) and particle image velocimetry (PIV) experiments were performed. This chapter describes the rotor system, the body shapes that were used, the general experimental setup and instrumentation, the experimental techniques, and the various technical challenges that were encountered during the work.

2.2 Rotor System

The experiments were conducted using a two-bladed rotor system mounted on a teetering rotor hub. The rotor had variable collective pitch capability, which allowed its thrust to be changed. The blades were untwisted with constant chord from root to tip and had a NACA 2415 airfoil cross-section. The rotor had a radius of 16 inches (0.408 m) and a chord of 1.752 inches (0.0445 m), giving a solidity, σ, of 0.0694. A sketch of the rotor blades used in the experiments is shown in Fig. 2.1. The rotor system was driven by a 3-phase, variable speed electric motor. Thrust and power measurements were made using an integrated load and torque cell.

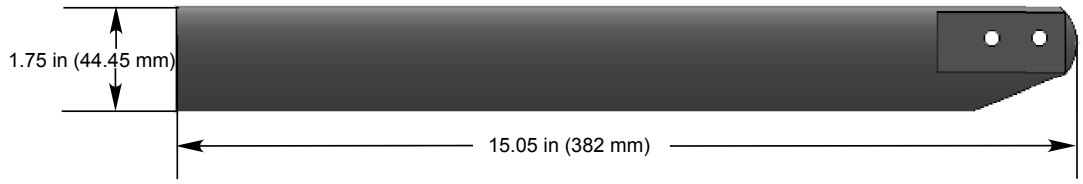

Figure 2.1: Rectangular rotor blade used for the present experiments with its characteristic dimensions.

The rotor was operated in the hovering state at a rotational frequency of 35 Hz (2,100 rpm), producing a blade tip speed of 89.72 ms^{-1} (294.36 fts^{-1}). The tip Mach number was approximately 0.27 and the tip chord Reynolds number, Re_{tip}, was 285,000. For all of the experiments, the rotor was operated at a disk loading, T/A, of 0.756 lb ft^{-2} and a blade loading coefficient, C_T/σ, of 0.0533. The IGE experiments were all conducted with the rotor plane at a height of one rotor radius above a circular ground plane.

2.3 Ground Plane

The ground plane used in the experiments had a diameter that was twice the rotor diameter. A schematic of the setup of the rotor, the ground plane, and one of the bodies is shown in Fig. 2.2. Notice that the rotor was tested with its axis of rotation being horizontal rather than vertical. While the current work focused on measurements at a single rotor height, the ground plane could also be repositioned to allow experiments to be performed at different rotor heights.

Flow diverters were installed around the periphery of the ground plane to redirect the remnants of the wake behind the plane and so limit the recirculation of any flow in

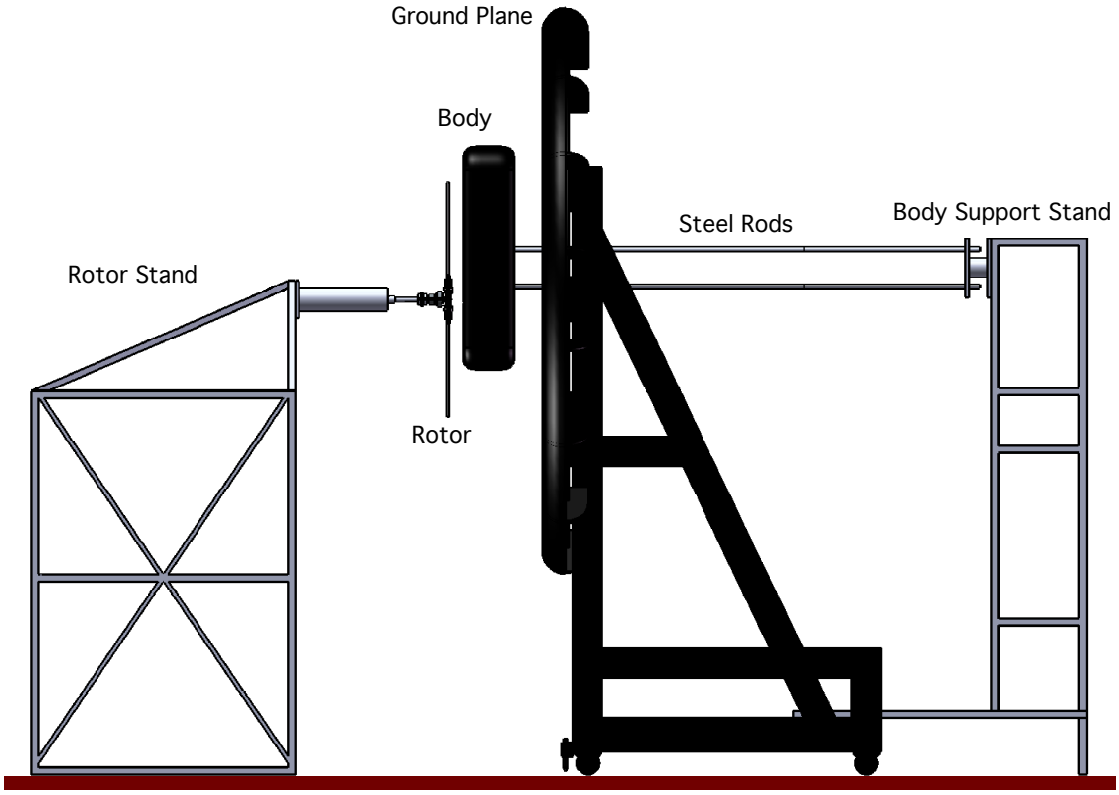

Figure 2.2: A schematic of the position of the rotor, the body, and the ground plane.

the test cell. Taking measurements of the flow field close to the ground required that reflections of the laser off of the ground plane needed to be reduced to acceptable levels. This goal was accomplished by painting the ground plane with a flat-black paint, as well as by judicious adjustment of the orientation of the laser sheet. Other challenges in dealing with surface reflections are discussed later in this thesis.

The bodies representing the fuselage of a helicopter were mounted on two steel rods that extended horizontally from an independent support stand through holes cut in the center of the ground plane. These rods were 0.5 inches in diameter and were located below the axis of rotation of the rotor to minimize their influence on the flow. Both rods were painted with anti-reflective paint to reduce surface reflections. The various bodies could be positioned below the rotor at various heights and orientations, as required. For the present experiments, the interest was in the flow around the front and rear parts of each body.

2.4 Test Cell

The rotor was tested in a flow conditioned test cell. The cell consisted of a wooden frame filled with aluminum honeycomb screens. The screens served as flow conditioners that reduced turbulence in the air that entered the test cell upstream of the rotor. To quantify the turbulence, several PIV measurements were taken in a region of quiescent flow outside of the rotor wake, as shown in Fig. 2.3. The measured excursions from the average flow velocity in this region are shown in Fig. 2.4. Such excursions represent the value of free-stream turbulence and result in only small variations in the local flow

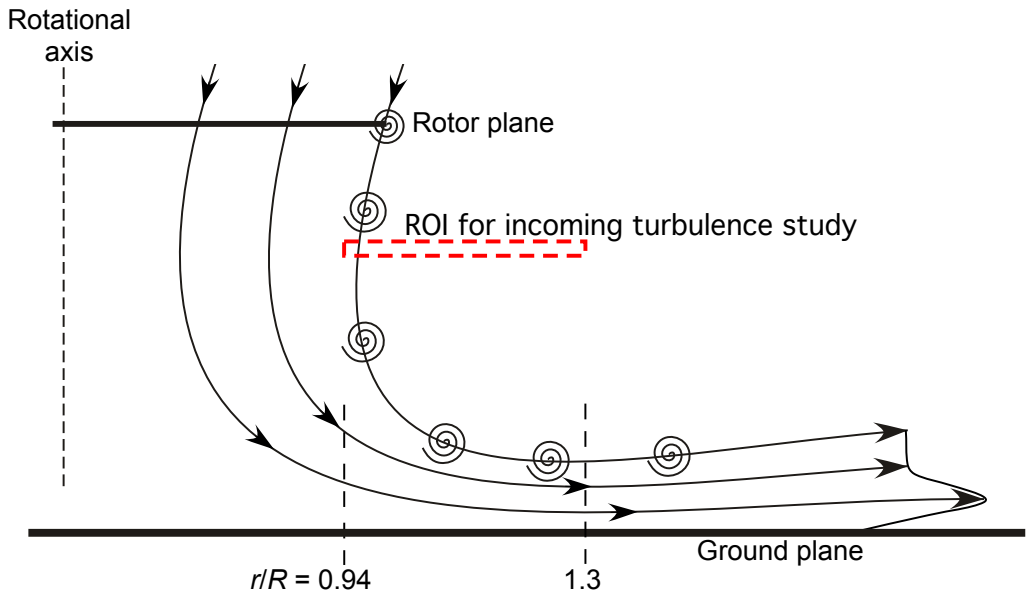

Figure 2.3: A schematic of the region of interest (ROI) used to measure representative turbulent velocities.

velocities. For the present experiments, the turbulence intensity of the incoming flow found to be less than 1% of the rotor tip speed.

2.5 Body Shapes

Three different body shapes were used in the present experiments. A side view of each body is shown in Fig. 2.5. The cross-sections of the bodies were circular, elliptical, and rectangular, respectively.

The body dimensions and their placement relative to the rotor were determined using historic data of existing helicopters [56]; see Fig. 2.7. Over 100 civilian and military helicopters were examined, covering a wide range of vehicle gross weights and rotor diameters. The dimensions and placement of the fuselage with respect to the rotor were

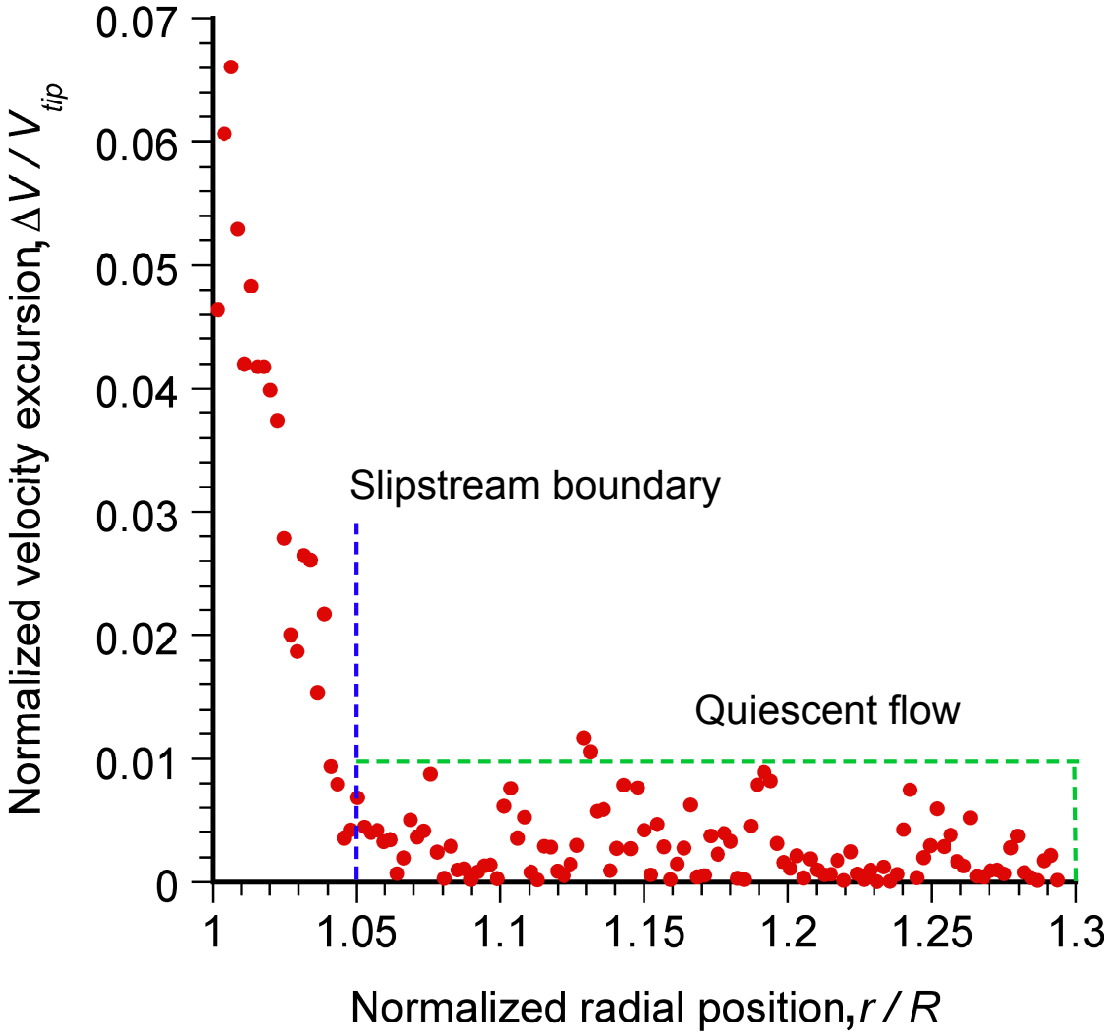

Figure 2.4: A plot of normalized turbulence velocity of the flow at a normalized height from the ground of $z/R = 0.6$.

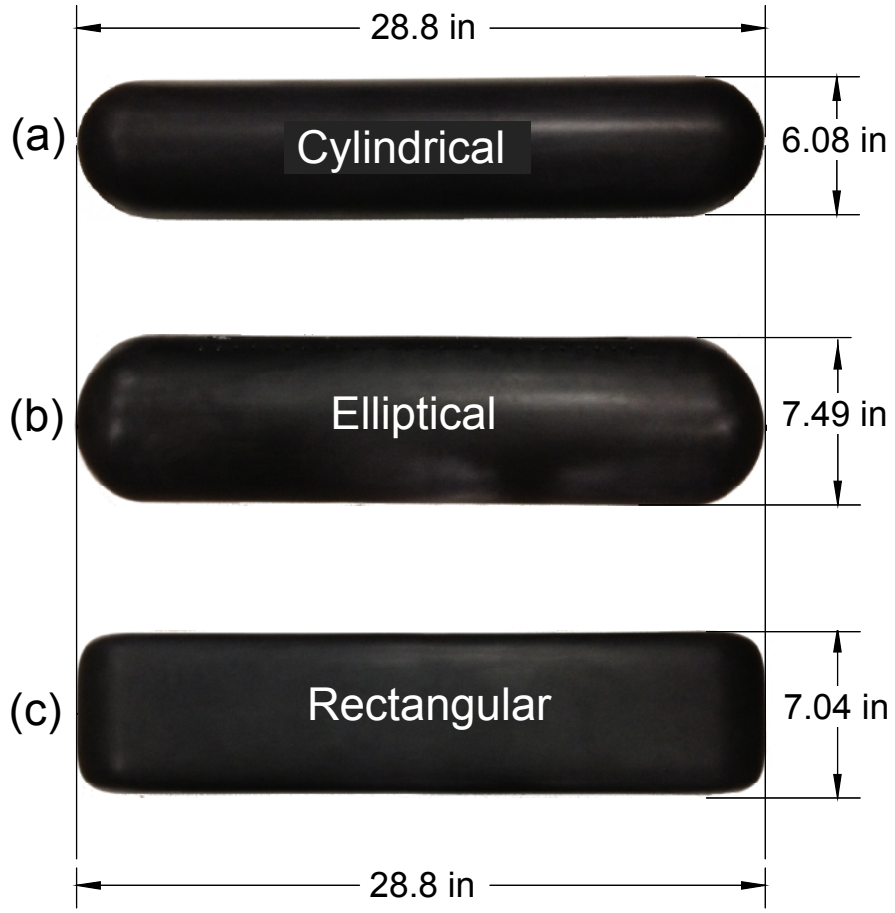

Figure 2.5: Side view of the three bodies used in the present experiments: (a) circular, (b) elliptical, (c) rectangular.

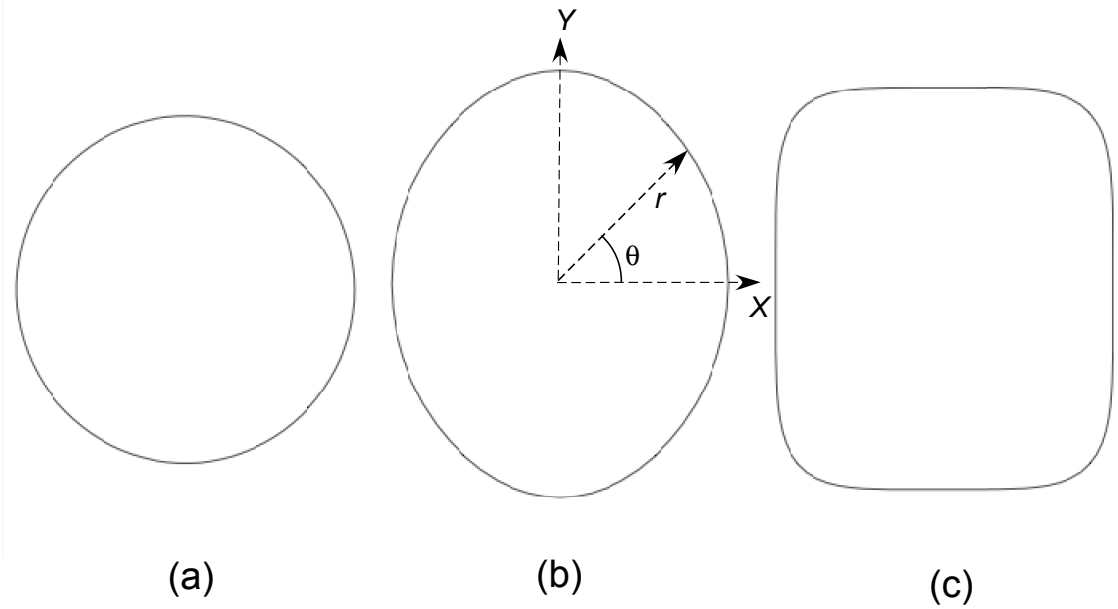

Figure 2.6: Cross-sectional viewspf the body shapes: (a) circular, (b) elliptical, and (c) rectangular.

Cross-section	m	n_1	n_2	n_3	a	b	Height (in)	Width (in)
Elliptical	2	5	5	5	3.04	3.04	7.49	6.08
Rectangular	4	5	5	5	3.04	3.52	7.04	6.08

Table 2.1: Super-ellipsoid equation input values and resulting dimensions.

averaged to determine representative dimensions that were ultimately used for the bodies that were tested in the present experiments.

Based on these historical data, the body length used was 0.9 rotor diameters, and the body width was 0.19 rotor diameters. The top surface of each body was positioned 0.125 rotor radii from the rotor plane (0.875 rotor radii from the ground plane). The front and rear of each body was 0.6 and 1.2 rotor radii from the rotational axis, respectively, as shown in Fig. 2.8.

A super-ellipsoid was used to define the shapes of the elliptical and rectangular body cross-sections by using the equation

$$r(\theta) = \left[\left| \cos(\frac{1}{4} m\theta)/a \right|^{n_2} + \left| \sin(\frac{1}{4} m\theta)/b \right|^{n_3} \right]^{-1/n_1} \tag{2.1}$$

Table 2.1 shows the values used in Eq. 2.1 and the resulting dimensions of the cross-sections of each body. The circular cross-section had a diameter of 6.08 inches (0.19 rotor diameters).

The bodies were manufactured using rapid prototyping from a honeycombed structural plastic with a high strength-to-weight ratio. They were painted with an ultra-flat black paint and given a matt finish to reduce reflections from the laser light sheet. The bodies could be mounted in two orientations with respect to the rotor, as shown in Fig. 2.8. These orientations allowed for investigation of the flow over the front and rear of each

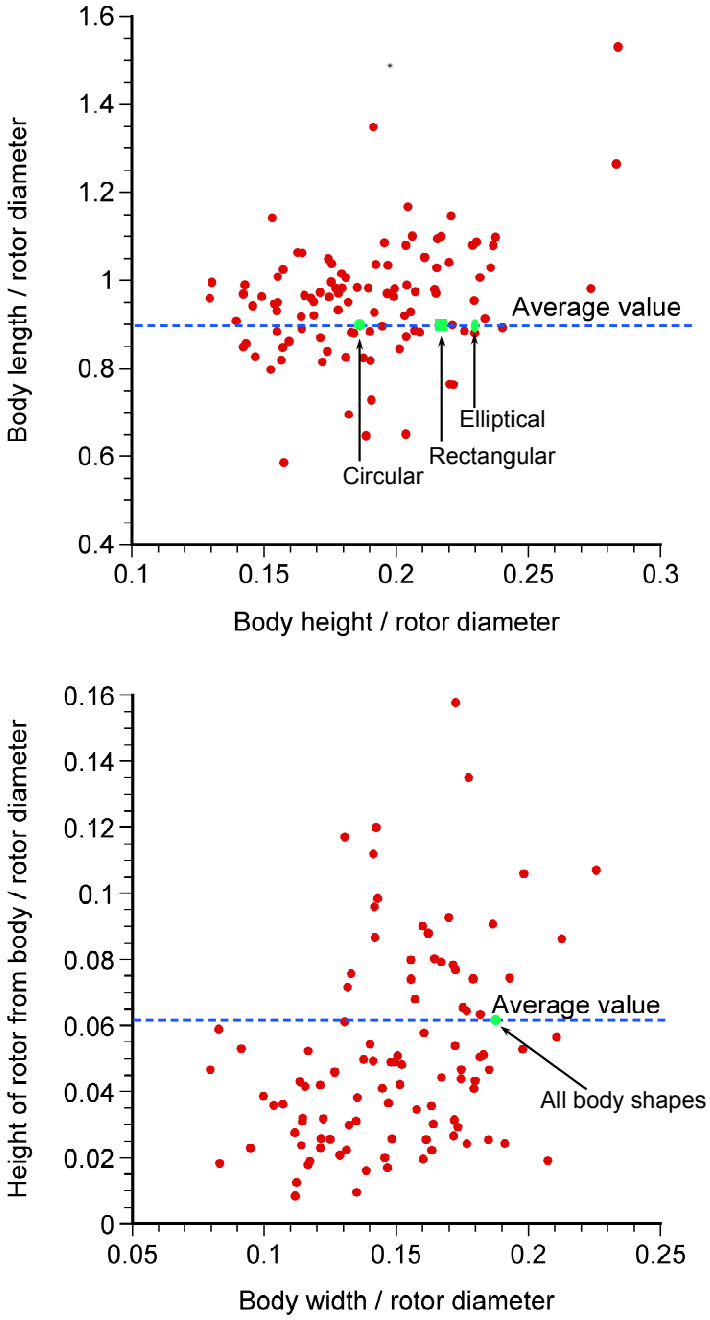

Figure 2.7: Historical fuselage dimensions for helicopters and the chosen representative dimensions of the bodies used for the current experiments.

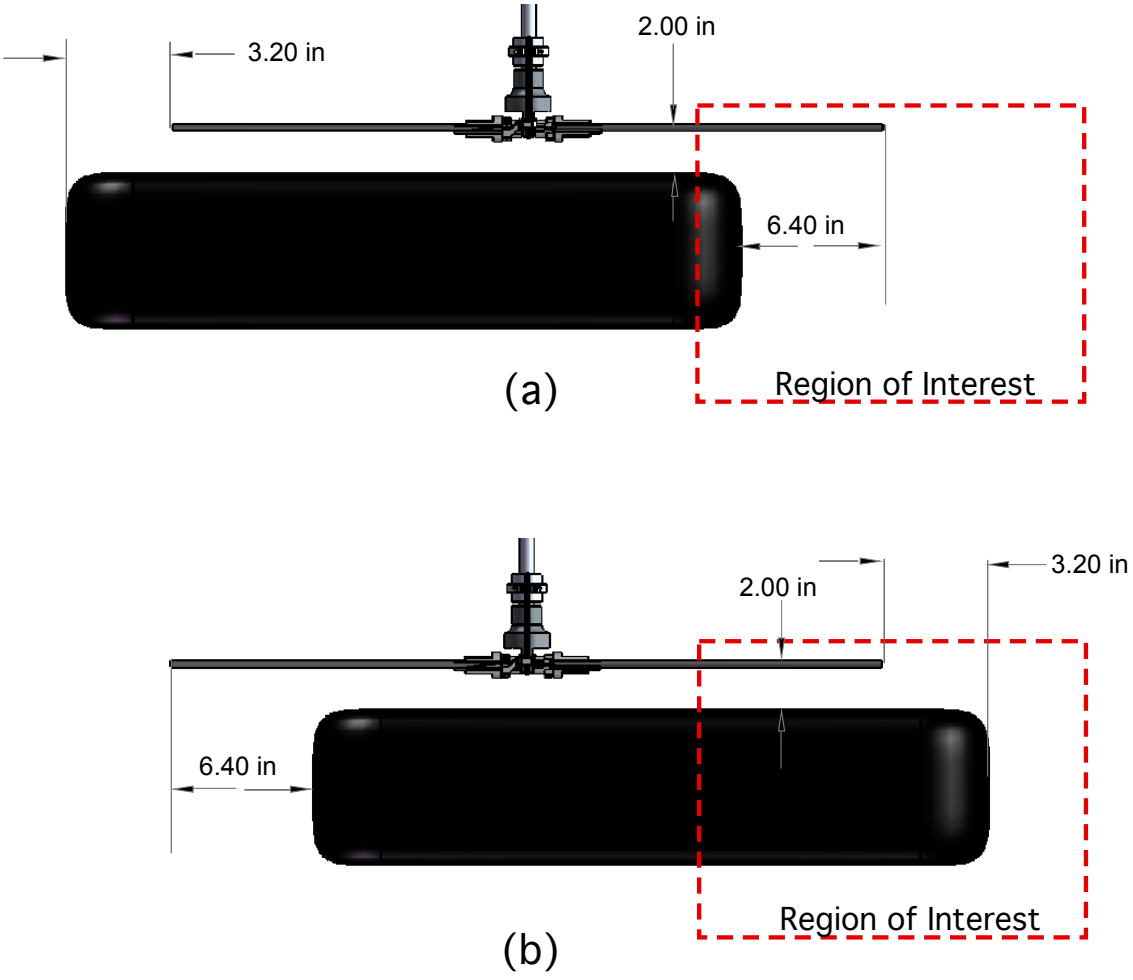

Figure 2.8: Schematic of the body location for the investigation of the flow field: (a) nose and (b) tail.

body without having to move the camera and optics.

2.6 Performance Measurements

To ensure that the rotor thrust and blade loading coefficient were constant throughout the testing, both OGE and IGE, it was necessary to determine the relationship between the rotor collective pitch angle and the rotor thrust. To this end, performance measurements were taken to determine the thrust and power for the rotor system as a function of collective pitch for the isolated rotor, as well as with each body in turn.

The rotor was mounted horizontally in a cantilevered position, so a load cell that could withstand large extraneous loads was necessary. A combination load/torque cell was installed that could measure up to 500 lb of thrust and 500 in-lb of torque. The output of the load cell was conditioned and passed through a 32 bit analog-to-digital (A/D) converter. The A/D converter was sensitive to small changes in the output voltage from the load cell, allowing it to read small output signals without the use of an amplifier. However, a low-pass filter was also employed to remove any noise.

The integrated load/torque cell was calibrated using known weights to determine a relationship between the applied loads and the output voltages. Thrust and torque tares were performed without rotor blades at rotational frequencies between 25 and 35 Hz; the tares have been removed from all of the balance measurements that are shown and discussed in this thesis.

A laboratory barometer and thermometer were used to measure the temperature and barometric pressure, respectively, which were used to calculate the density of the air

using the equations of the standard atmosphere. During testing, the collective pitch was periodically adjusted to keep thrust and blade loading coefficient constant.

2.7 Instrumentation and Setup

The two measurement techniques used in the present experiments utilized the same instrumentation and experimental setup. To illuminate the flow, a Nd:YAG laser that emitted light with a wavelength of 532 nm with 200 mJ/pulse at a rate of 15 Hz was used. A 4 mega-pixel (4 Mp) CCD camera that could capture 15 frames/second at a resolution of 2,048-by-2,048 pixels was used to image the flow. The FV measurements used a wide angle 28 mm camera lens with an f-stop of 2.8, and the PIV measurements used a 105 mm lens with an f-stop of 2.8.

The laser light was thinned into a sheet to illuminate the desired region of interest (ROI), as shown in Fig 2.9. To this end, the laser was fired off a mirror and through spherical and convex lenses. The spherical lens converted the beam into a light sheet and the convex lens thinned the sheet to a thickness of approximately 1 mm at its waist [10, 57]. The viewing axis of the camera was oriented orthogonally to the plane of the light sheet, and carefully focused on the desired region of interest in the rotor wake.

For both the FV and the PIV, the light sheet was aligned such that the cameras could capture images of the flow along the longitudinal axis of each body. This position was chosen because any effects in the flow that arises from differences in body shape are likely to be most pronounced along the longitudinal axis compared to laterally.

Because the laser repetition rate (15 Hz) was less than the rotational frequency of

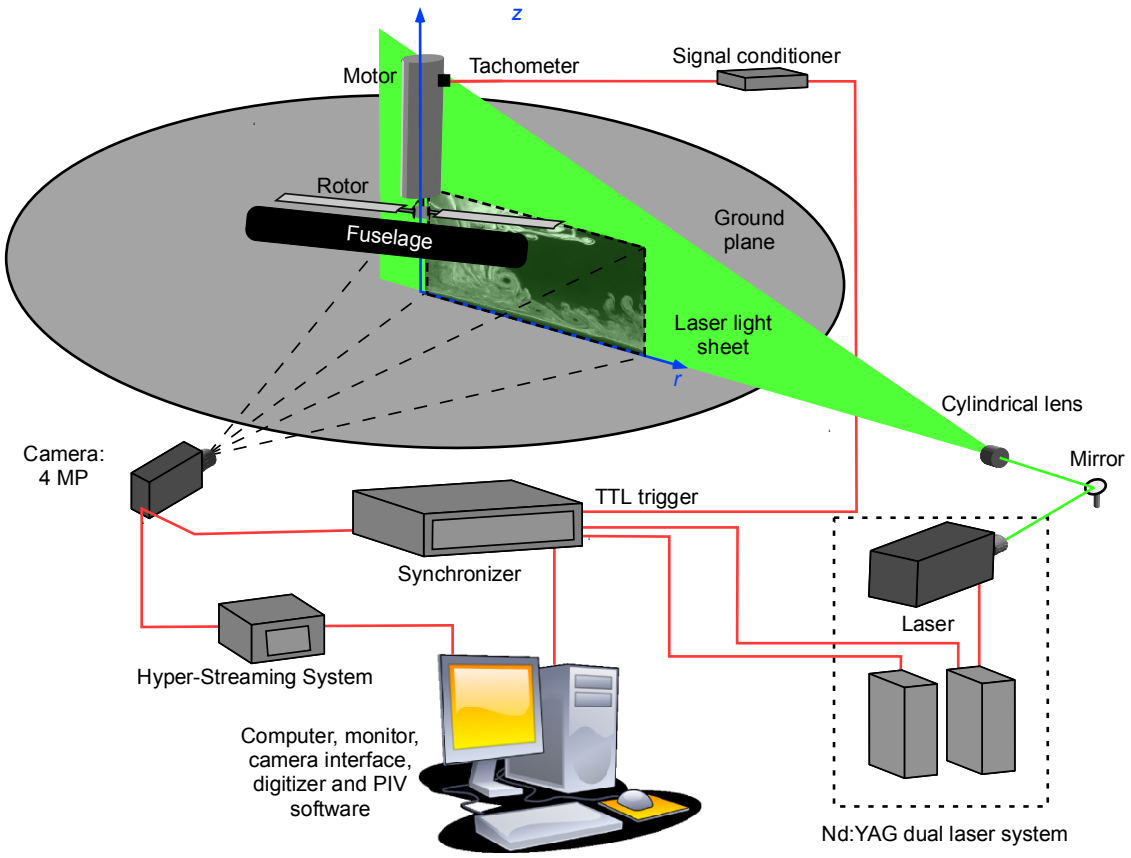

Figure 2.9: Schematic of the experimental setup showing the rotor, body, and the circular ground plane.

the rotor (35 Hz), it was necessary to synchronize the rotor and imaging system using a combination of electronics and software. The rotational frequency of the rotor was measured with an infra-red sensor, which output a once-per-revolution signal. This signal was converted into a square-wave signal and read into a timing hub that converted it into a TTL signal to trigger the laser, which could also be modified with a phase delay. This delay allowed for the selection of any blade azimuthal position, ψ, which enabled measurements to be taken at different wake ages, ζ. Notice that wake age is defined as the time in degrees of rotor rotation that has passed since the development of a vortex element in the flow. In the present work an azimuthal increment of 30° was used, so that for the present experiments the flow could be measured at wake ages of $\zeta = 30^\circ, 60^\circ, 90^\circ$, etc.

2.8 Seeding

To produce seed particles for both the FV and PIV, a mixture of pressurized nitrogen gas and a mineral oil were heated until the oil vaporized. The vaporized mixture was then ejected into the cooler ambient air, where the temperature decreased rapidly and the mixture condensed into a thick white fog. Over 95% of the seed particles produced by this method have been shown in previous work [58] to have diameters of 0.2 μm, small enough to minimize the particle tracking errors.

The FV and PIV required different flow seeding techniques. For the FV, a large amount of seed was injected quickly into the flow using a series of ducts. This technique produced concentrated bands of seed particles that became entrained into the flow and

could be used to visualize the pertinent flow structures. For the PIV measurements, the seeding was more uniformly dispersed. In this case, with the seed particles dispersed throughout the flow, the flow structures were not easily identified. However, this seeding produced the "star field" patterns needed to perform successful cross-correlations with the images for making PIV measurements.

2.9 Flow Visualization (FV)

Detailed FV experiments were performed in the rotor wake with a wide-angle lens that could view the entire plane of the wake illuminated by the laser sheet. The objective here was to obtain a qualitative view of the rotor wake as it interacted with the ground plane, as well as to compare the wake of the rotor in the presence of a body. Of particular interest were the trajectories of the tip vortices as they convected towards the body and toward the ground plane along a longitudinal plane passing through the body.

2.10 Particle Image Velocimetry (PIV)

While the FV provided good qualitative insight into the flow structures present in the rotor wake, quantitative measurements were obtained using PIV. PIV is a non-intrusive technique that allowed for the measurement of the flow velocities in a plane at a single instant in time. PIV is also a planar measurement method and has a significant advantage over other types of point-by-point flow field measurement techniques like laser Doppler velocimetry (LDV) or hot wire anemometry.

Stereosopic PIV, which measures velocity components in all three dimensions would

be the ideal measurement technique for these experiments. However, stereoscopic PIV would require significant experimental complexity and processing time greater than that available for the current experiment. Because this experiment was mainly a scoping experiment to develop a fundamental understanding of the effect of body shapes on the flow under a rotor, 2-D PIV was deemed to be sufficient for the current purposes.

To perform the PIV measurements, the flow was seeded with sub-micron particles. The flow was illuminated by the laser twice over a short time, Δt, on the order of microseconds, and a pair of images is generated from the Mie scattering by the particles. To extract the velocity fields, the images were sub-divided into many small interrogation areas (i.e., 16x16, 32x32 pixels) [59]. To calculate the pixel displacements of the seed particles between the two images, a cross-correlation algorithm was employed. The displacements were calculated to sub-pixel accuracy for each interrogation area, assuming the particles are displaced an equal amount between the two images. This process yielded a single velocity vector for each interrogation area.

The cross-correlation was performed using a Fast Fourier Transform in the frequency domain, and then converted to the spatial domain [60, 61]. Using the pixel displacements Δx and Δy, the local velocity vectors are calculated using

$$(U,V) = \frac{(\Delta x, \Delta y)}{M\Delta t} \tag{2.2}$$

where M is the image magnification calculated by determining the number pixels in the image that correspond to the size of an object of known dimensions (i.e., a scale). A schematic of the process is shown in Fig. 2.10. This basic procedure was followed for all interrogation regions.

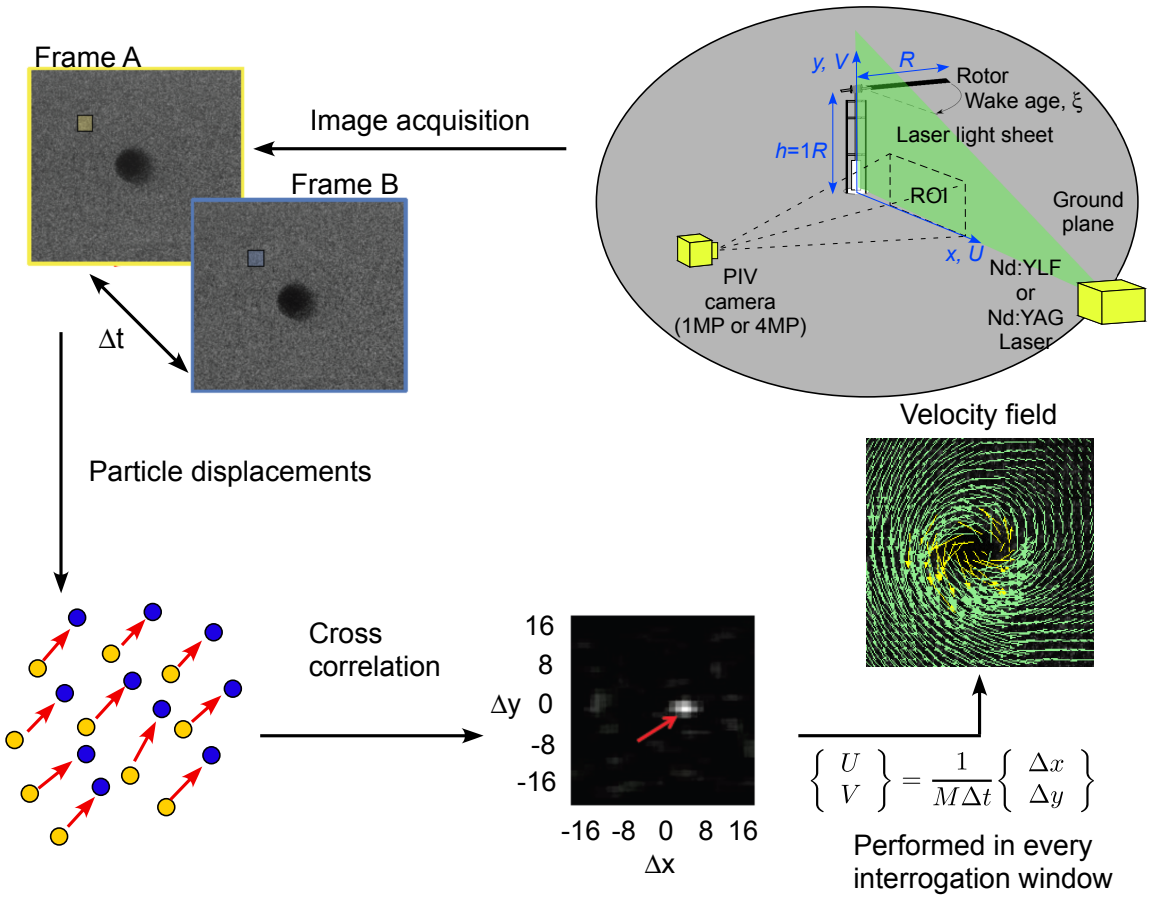

Figure 2.10: Schematic of the PIV measurement process.

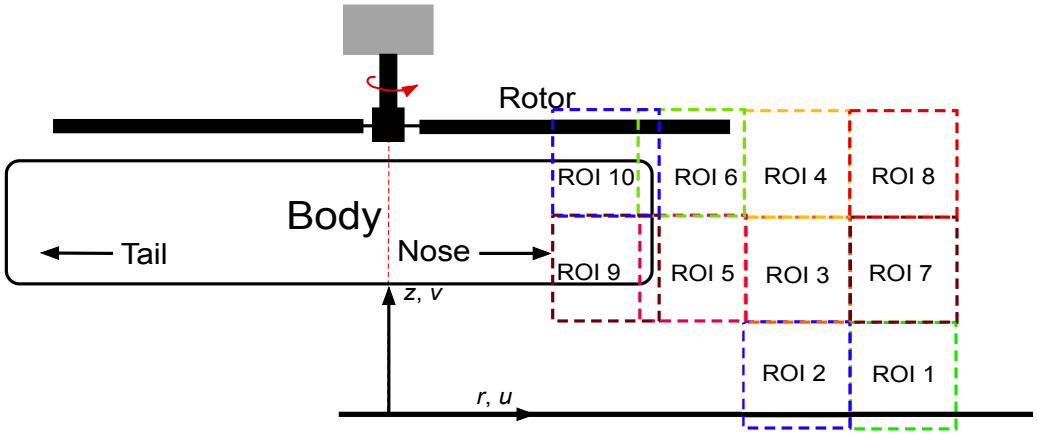

Figure 2.11: Regions of interest (ROI) in the present work, which encompassed the wake near the rotor, the body, and the ground plane.

While PIV allows for quantitative analysis of the flow structures in the rotor wake, the spatial resolution necessary to track the seed particles required that smaller regions of the flow be investigated. As shown in Fig. 2.11, the area of investigation was subdivided into ten ROIs. For each ROI, measurements were taken with the isolated rotor first, and then with each body in sequence. Measurements were taken at the front and rear of each body so that the flow beneath the rotor could be analyzed in both areas. These regions provided a full coverage of the desired section of the rotor wake, and allowed for the tracking of the wake down to the ground plane while still maintaining sufficient spatial resolution with the 4 Mp camera to resolve the vortices in the flow. Using PIV, the flow structures near the ground could be resolved to as close as 0.2% R (0.032 inches) from the ground plane.

For each ROI, 500 PIV image pairs were taken at azimuthal increments of 30°. Previous work [62] has shown that 500 image pairs provide sufficient statistical data to

ensure the accuracy of the measurements in a vortex flow. ROI 2–10 used interrogation windows of size 24-by-24 pixels; this grid provided the necessary spatial resolution to resolve the flow structures in the rotor wake. The flow analysis for ROI 1 was more difficult, and will be discussed further in the next section.

An image deformation method with a 50% overlap was used for the cross-correlation processing [63]. This method began with an interrogation window size of 48-by-48 pixels and iterated to a 24-by-24 pixel window size. Local vector validation was performed using the universal median test with a 3-by-3 vector neighborhood, and output to a vector conditioning program. The conditioning program used a local median test with 3-by-3 neighboring vectors. A Gaussian peak with a signal-to-noise ratio of 1.5 was used to identify spurious vectors, and images with more that 5% spurious vectors were removed from the analysis. Fewer than 1% of the images taken during the present experiments were rejected because of spurious vectors.

A disadvantage of the PIV system used here was that only a small section of the flow could be observed at one time. Therefore, the images could not yield flow measurements that were temporally correlated. Furthermore, as with the flow visualization, the PIV system could only acquire data at a sub-multiple of the rotor frequency, so the developments of individual flow structures could not be tracked in time.

2.10.1 Challenges with PIV

Several challenges arose while performing PIV measurements, particularly when measurements were taken near solid boundaries such as the body or a ground plane. One

significant problem is the surface reflections produced by the laser sheet, which may be of a higher intensity than the Mie scattering from the seed particles in the flow. Such reflections can create difficulties in obtaining good cross-correlations. An example of reflections off the ground plane is shown in Fig. 2.12.

During testing, several methods were found to reduce such reflections. Several types of paints were tested to determine their reflective properties, and a specific anti-reflective flat black paint was finally selected. Periodic cleaning of the surface also proved to be an effective means of minimizing reflections; during testing some of the seed particles would condense on the ground plane and a thin film of oil would develop. Oil has much stronger reflective properties than the paint, and so the oil was removed periodically by wiping the surface with damp rags and then drying it with a lint-free cloth.

The most effective technique for reducing reflections was judicious laser alignment. The laser optics were positioned such that the surface of the ground plane bisected the laser light sheet. Therefore, the light rays were more parallel to the surface, significantly reducing reflections. Figure 2.12 shows an example of the reduced reflections after the laser alignment had been performed.

Reflections from the bodies and the body mounting structures were also of concern. While the mounting rods supporting the bodies were painted flat black, there were still some reflections. To remove these reflections, all surfaces were covered with a reflection absorbing cloth. To remove reflections from the bodies themselves, it was necessary to treat the body surface with an ultra-flat black paint with a matt finish similar to that used for the ground plane. The outcome was that reliable PIV measurements could be taken much closer to the surface of the body.

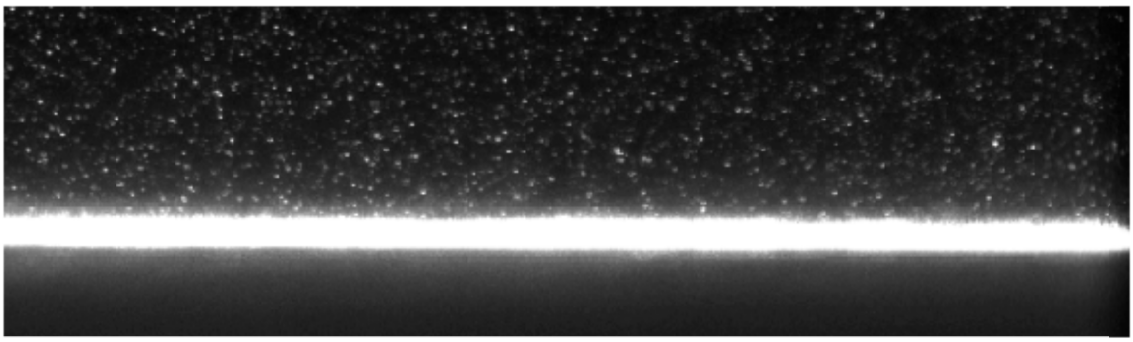

(a) Before

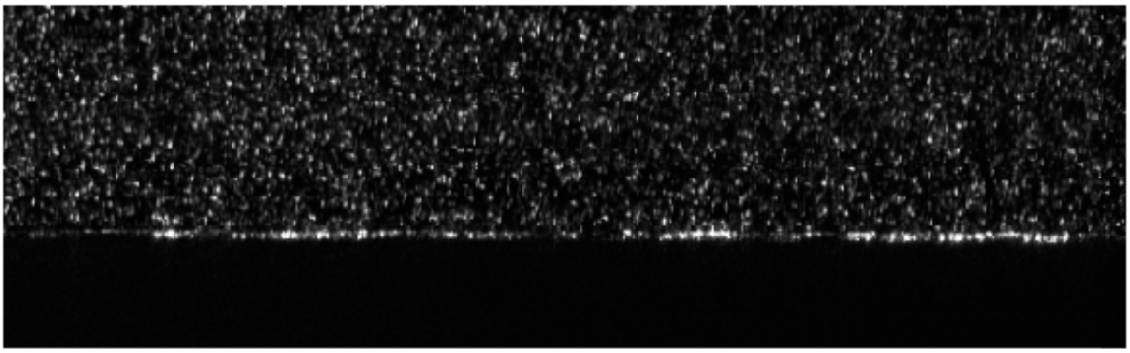

(b) After

Figure 2.12: Reflections off the ground plane: (a) before and (b) after the implementation of reflection reduction techniques [15].

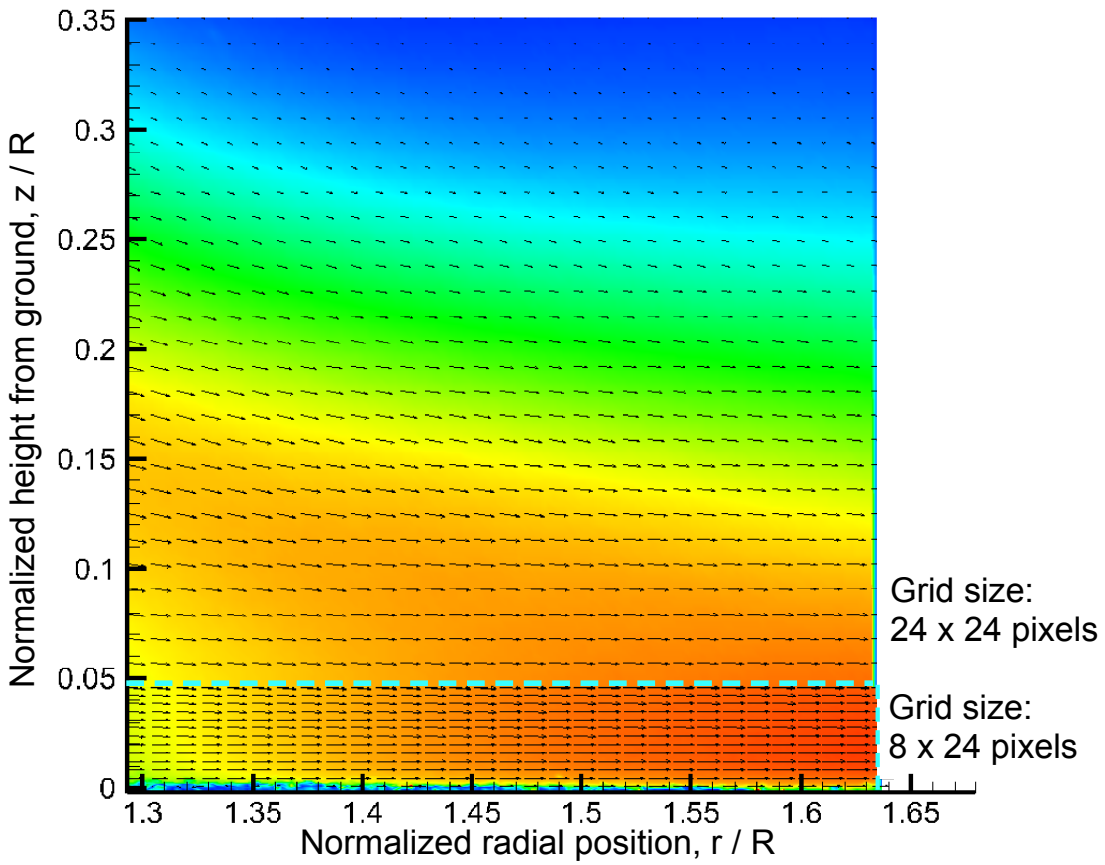

Figure 2.13: PIV image showing the two grid sizes.

A different cross-correlation technique was used for making PIV measurements in ROI 1 [64] because this region had sections of both axial (downward) and radial (outward) flows. To resolve both flow types, it was necessary to divide this ROI into two sections. To this end, a primary cut was made approximately 20 mm above the ground plane; see Fig. 2.13. Above this cut, the flow was primarily in an axial direction and contained significant influences from the tip vortices. This region was analyzed with the same cross-correlation technique as used in the other regions, as described in previously.

Below the cut, the flow had turned to form an outward moving wall-jet type of turbulent flow along the ground plane with high wall-normal velocity gradients. To measure

this flow, rectangular PIV interrogation windows were required to obtain the necessary spatial resolution to resolve small-scale fluctuations in the boundary layer. To this end, the interrogation windows were modified to a size of 8-by-24 pixels. Rectangular interrogation windows were not used for ROI 2. Although this region was also near the ground, at these locations the flow was still in the process of turning outward and so they contained significant axial (downward) velocities. When rectangular interrogation windows were used in ROI 2, inaccurate cross-correlations were obtained.

2.11 Uncertainties in the PIV Measurements

There are several sources of measurement uncertainty that arise when using PIV to measure the flow. These sources include particle tracking errors, laser reflections, background noise, laser pulse separation time (from uncertainties in the software), and interrogation window size. Errors occur when the seed particles do not accurately follow the flow. In the present tests, however, the seed particles that were used have been shown in previous work [58] to produce small tracking errors.

Background noise, which may result in inaccurate cross-correlations and erroneous vectors, arises from electrical noise in the camera CCD that may create artificial intensities in the image pair. Background noise errors were reduced by implementing a strict signal-to-noise ratio when assessing vector validity.

To minimize the resulting errors, an image deformation method was implemented. The estimated pulse separation uncertainty was 0.005% and the magnification factor error was 0.95%. Along with the estimated pixel displacement uncertainty of 4.7%, these val-

ues can be used to determine the total uncertainty in measurements of flow velocity (U) by using the equation

$$\Delta U = \sqrt{\left(\Delta\varepsilon_{\Delta x}\frac{\partial U}{\partial \Delta x}\right)^2 + \left(\Delta\varepsilon_{\Delta t}\frac{\partial U}{\partial \Delta t}\right)^2 + \left(\Delta\varepsilon_{M}\frac{\partial U}{\partial M}\right)^2} \tag{2.3}$$

where $\varepsilon_{\Delta x}$,$\varepsilon_{\Delta t}$, and ε_M are the pixel displacement, pulse separation time, and magnification factor, respectively. The total error in the flow velocities was estimated to be approximately 4.9% for the present experiments.

2.12 Summary

The present chapter has discussed the experimental setup, techniques, and methodologies used to obtain measurements of the flow below a rotor operating in-ground-effect conditions. The rotor was examined in isolation, as well as in the presence of three bodies with three different cross-sections namely circular, elliptical, and rectangular, respectively. The body dimensions and placement were chosen based on historic data trends from contemporary helicopters. The technical challenges encountered during the experimental process were discussed, and estimates of the sources of error were presented. The results obtained from the measurements are discussed in the following chapter.

Chapter 3

Results and Discussion

3.1 Introduction

As discussed in Chapter 1, the structure and characteristics of the wake generated by a hovering rotor in-ground-effect can be affected by the presence of a body in the wake below the rotor. The resulting velocity field at the ground may also be affected by the body, and so the body may potentially affect the brownout signature that would be generated by the rotor if was operating over a mobile sediment bed. To this end, the present study has measured the flow fields generated by a two-bladed rotor in isolation over a ground plane and also in proximity to three bodies of different cross-sectional shapes, the experimental setup having been described in Chapter 2.

3.2 Performance Measurements

Rotor performance measurements were taken, the procedures being discussed in Section 2.6. Power polars for the isolated rotor and with the three body shapes are shown in Fig. 3.1. It can be seen that the presence of the bodies had relatively small effects on the thrust generated by the rotor or the power required for its operation. The trend lines shown in this figure were calculated by using the momentum theory for a hovering

Body Shape	C_{P_0}	κ	C_{d_0}
Isolated Rotor	0.0001210	1.1394	0.01395
Circular	0.0001105	1.1459	0.01273
Elliptical	0.00012063	1.1704	0.01390
Rectangular	0.0001106	1.1906	0.01275

Table 3.1: Profile power coefficient and induced power coefficient, and profile drag coefficient for the isolated rotor and the rotor with each body shape.

rotor [65], i.e.,

$$C_P = C_{P_0} + \frac{k{C_T}^{3/2}}{\sqrt{2}} \tag{3.1}$$

where C_{P_0} is the profile power coefficient and κ is the induced power factor. Confidence in this fit, quantified as the coefficient of determination, R^2, was over 0.995 for all cases.

The resulting values of C_{P_0} and κ are presented in the Table 3.1. All cases had similar values of C_{P_0} and profile drag coefficient, C_{d_0}. The bodies caused an increase in induced power coefficient, which is expected, as a body under the rotor must alter the rotor inflow distribution to some degree. Inflow distribution is strongly linked to induced power coefficient. The body with the rectangular cross-section was noted to require the most power. The values of κ are typical of what might be expected from a rotor with untwisted blades such as the one used in the present experiments.

Performance measurements were taken by varying the collective pitch while maintaining the rotor a constant rotational frequency (in this case, a rotational frequency of 35 Hz or 2,100 rpm was used). This approach allowed for the relationship between the blade loading coefficient, C_T/σ, and the collective blade pitch, θ_0, to be established,

which shown in Fig. 3.2. Using blade element momentum theory (BEMT) from Ref. [65], a trend line was created using the equation

$$\theta_0 = \frac{6C_T}{\sigma C_{l\alpha}} - \frac{3}{4}\theta_{tw} + \frac{3}{2}\sqrt{\frac{C_T}{2}} \tag{3.2}$$

Notice that $\theta_{tw} = 0$ in this previous equation because the blades are untwisted. A least-squares fit was used to match the trend line to the data. The coefficient of determination for each case was over 0.995. Using this relationship, collective pitch could be adjusted as desired to ensure that such that all of the measurements were taken at a constant blade loading coefficient, which in this case was $C_T/\sigma = 0.0533$.

The vertical force acting on each of the bodies that were beneath the rotor was also measured. Figure 3.3 shows the variation of the body forces as a function of blade loading coefficient. The body force coefficient was calculated using

$$C_{F_b} = \frac{F_b}{\rho A {V_{tip}}^2} \tag{3.3}$$

where F_b is the vertical force on the body and the other symbols have their usual meaning.

It is interesting to note that for Fig. 3.3, the bodies with circular and elliptical cross-sections experienced similar loads for at the same values of C_T/σ. Furthermore, at the higher values of C_T/σ both bodies develop an up-force, which is an indication of the Fradenburgh "thrust recovery effect." The difference in the loads between the circular and elliptical cross-sections is likely a result of differences in wake shape caused by the different curvature of the cross-sections. In particular, the body with the elliptical cross-section has more shallow curvature, causing the flow to stay attached longer to the body and resulting in a smaller wake. However, the body with the rectangular cross-section showed a different trend in the vertical force over the same range of C_T/σ. After an

initial small increase in up-force at low blade loading coefficients, the body developed a downforce as C_T/σ increased. In this regard, the circular and elliptical cross-sections are more similar in shape, so that the force on the body with rectangular cross-section expected to behave differently when it is located inside the rotor wake. The wake structure below each of the bodies is discussed later in this chapter.

3.3 Rotor Wake Structure

Before investigating the details of the rotor wake, it was first necessary to examine the general structure of the wake as a whole. To this end, phase-resolved flow visualization of a large section of the rotor wake was conducted. The flow visualization produced images of the rotor wake as it convected towards the ground plane. It is important to note that the field of view for the flow visualization images covered all of the ten ROIs used for the PIV; see Fig. 2.11.

To provide a baseline for comparison, flow visualization (FV) was first conducted on the isolated rotor. Figure 3.4 shows and example of FV that was taken at a blade azimuth angle, ψ_b, of 0°. Each blade trails a wake dominated by helicoidal tip vortex that intersects the light sheet at wake ages $\zeta = (\psi_b + 360°)/N_b$, where N_b is the number of rotor blades. Recall that a 2-bladed rotor was used, therefore, for $\psi_b = 0°$ the present rotor produced vortex filaments that intersected the light sheet at $\zeta = 180°$, 360°, 540°, etc.

The tip vortices could easily be distinguished by the dark seed "void" that forms because of the small centrifugal accelerations acting on the seed particles at the center of

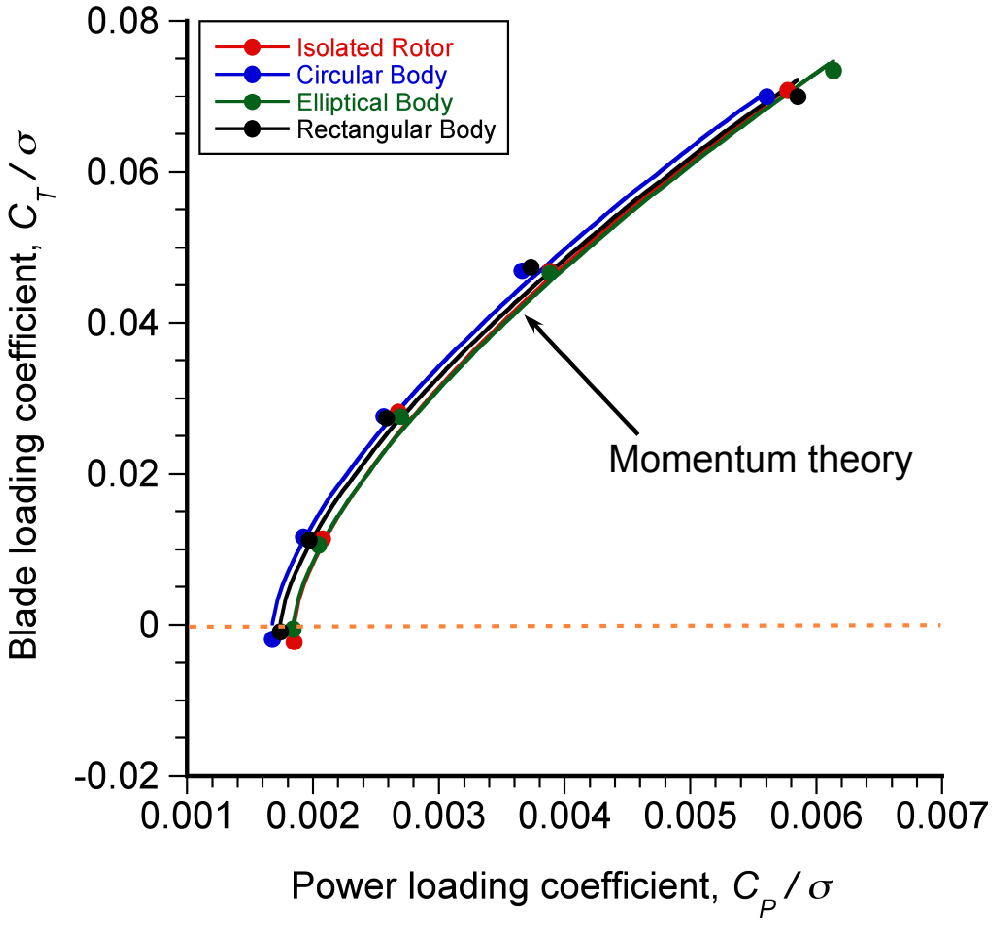

Figure 3.1: Plot of power polars for the isolated rotor and for the rotor with the three body shapes, with curve fits from momentum theory.

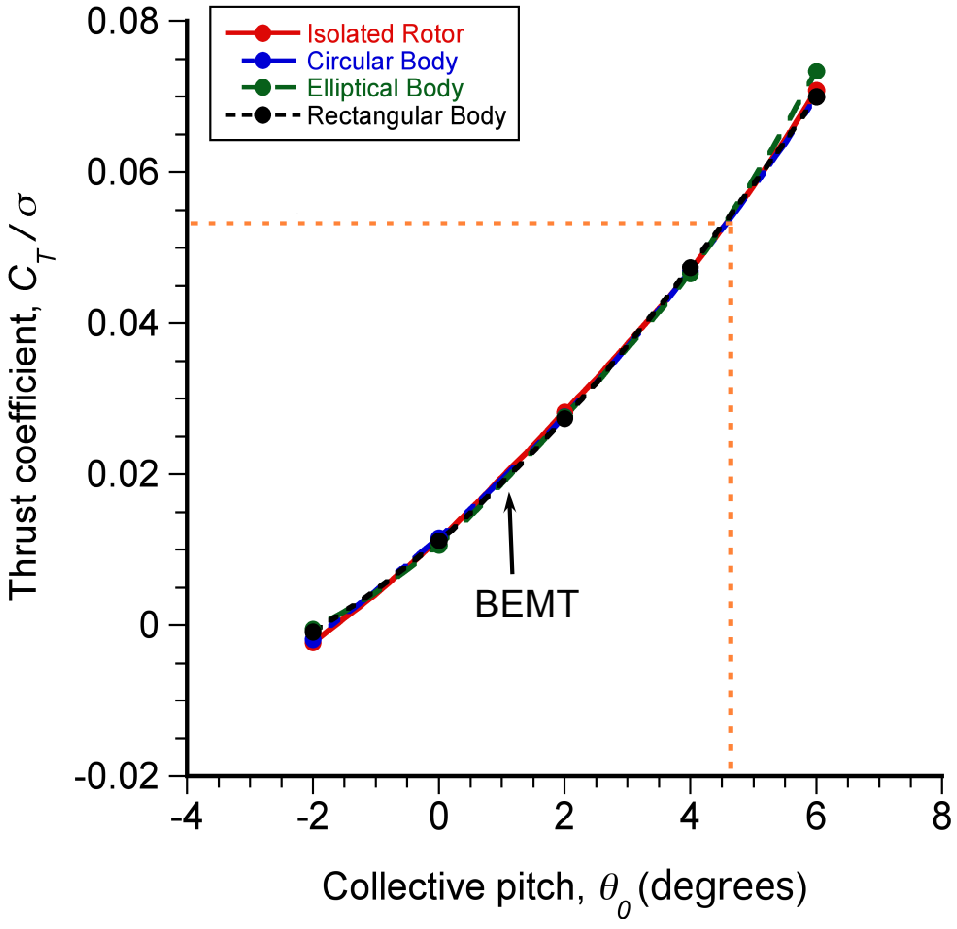

Figure 3.2: Plot of thrust coefficient versus collective pitch with curve fits from the BEMT.

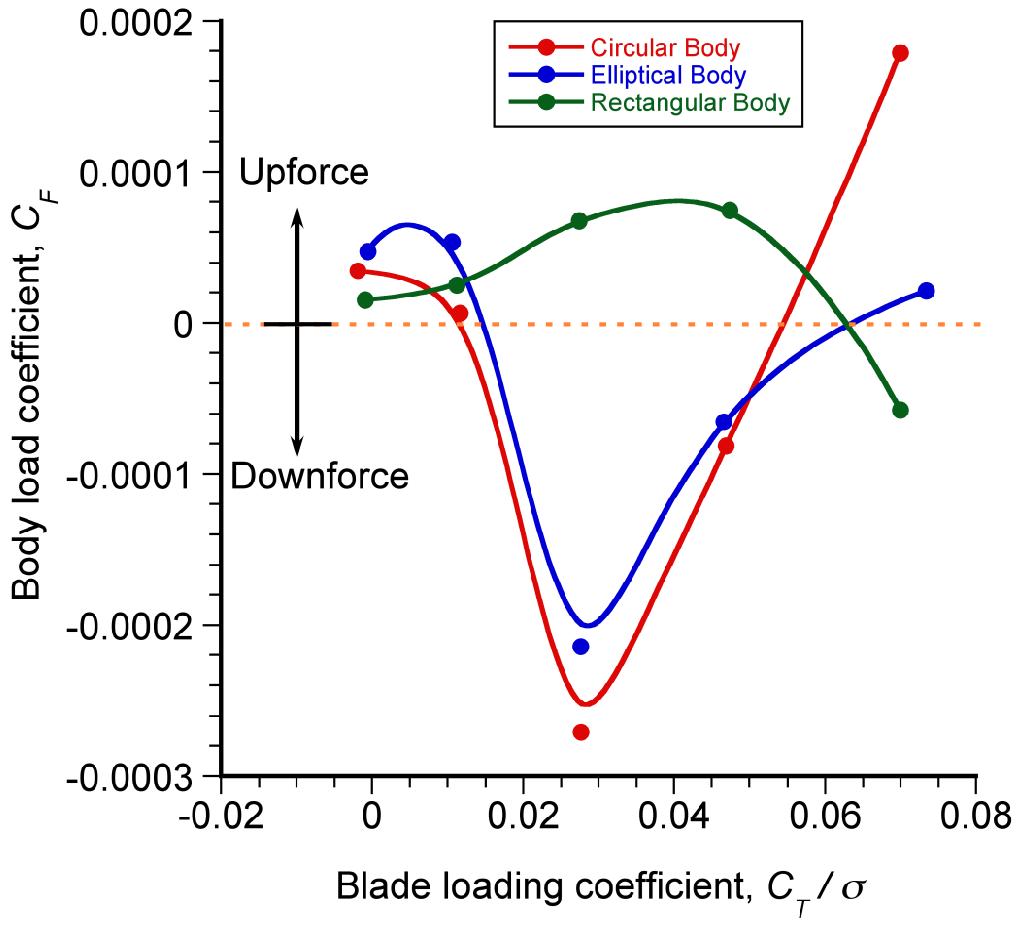

Figure 3.3: Vertical loads on each of the three body shapes over a range of rotor blade loading coefficients.

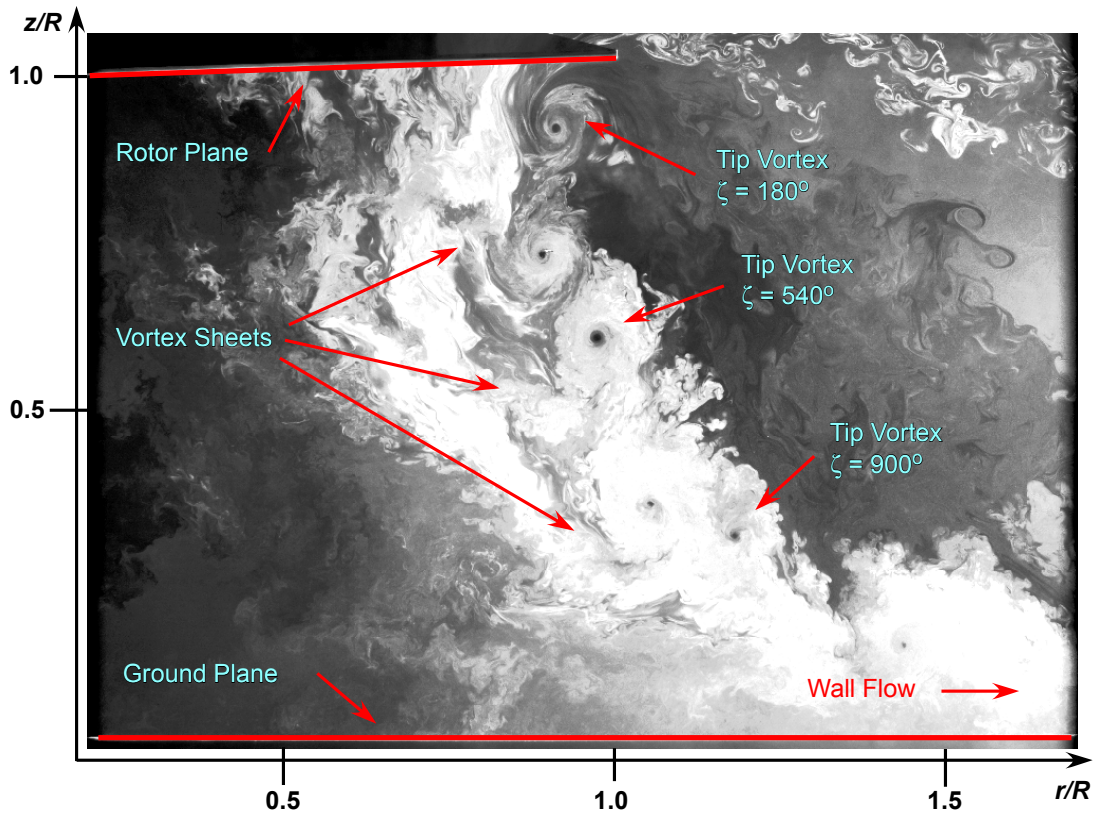

Figure 3.4: Flow visualization image of the isolated rotor wake at a blade azimuth angle of $\psi_b = 0^\circ$.

the vortex flow. Although there appear to be no seed particles in the vortex core as seen in the flow visualization, this area can still be seeded sufficiently to make PIV measurements, i.e., to enable successful cross-correlations of the PIV image pairs.

From an examination of the results shown in Figs. 3.5, 3.6 and 3.7, it is evident that the rotor wake is qualitatively similar as it approaches the nose of each body as compared to the wake obtained with isolated rotor. Both the trailed tip vortices and turbulent wake sheet can be clearly seen. Notice that apparent differences in the size of the seed voids do not necessarily reflect any variations in the strength or structure of the tip vortices because seeding distributions can vary between the various tests. (Consistency of seeding

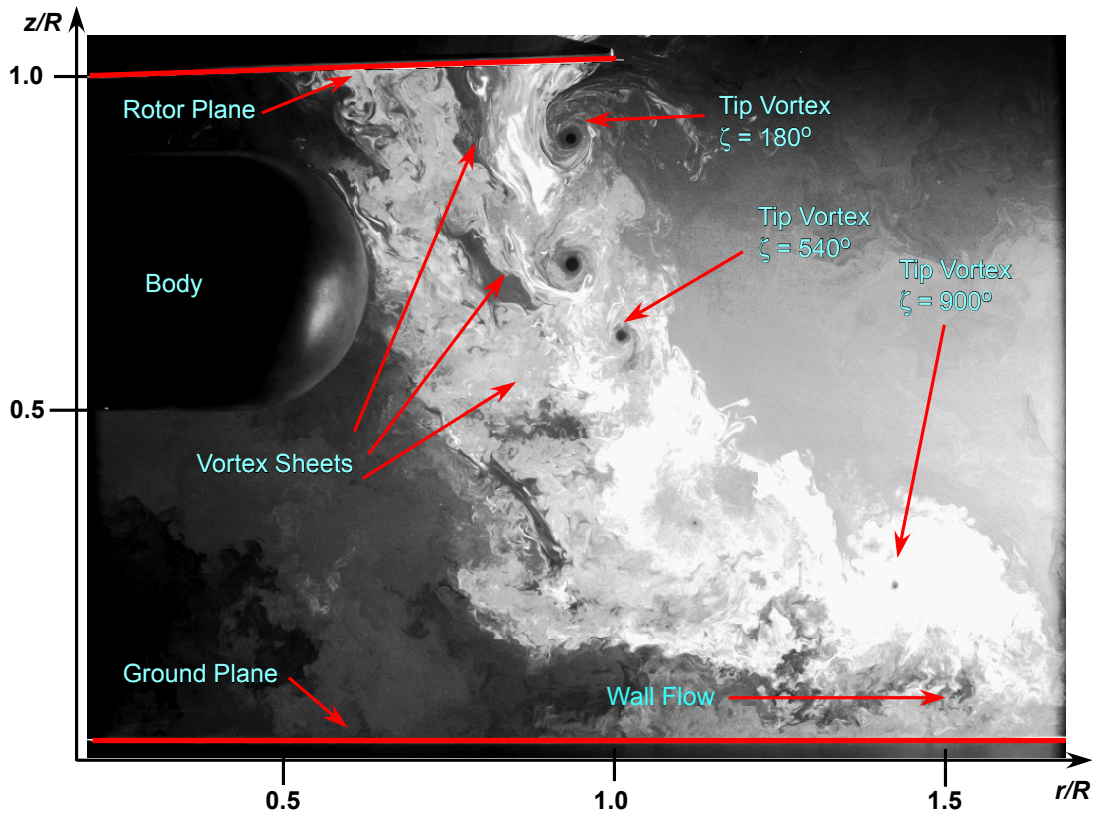

Figure 3.5: Flow visualization of the rotor wake over the nose of the body with the circular cross-section at a blade azimuth of $\psi_b = 0°$.

is almost impossible to achieve.) In all cases, the wake then convects towards the ground plane, where it then turns radially outward to become more of a wall-parallel flow as it develops over the ground.

Further examination of the flow visualization shown in Figs. 3.5–3.7 reveals that the tip vortices obtained with the bodies with the circular and elliptical cross-sections followed similar trajectories as they convected towards the ground. However, with the body with the rectangular cross-section, the tip vortices were clearly located farther inboard radially with less overall expansion of the rotor wake.

Using a number of instantaneous PIV realizations of the flow, it was possible to

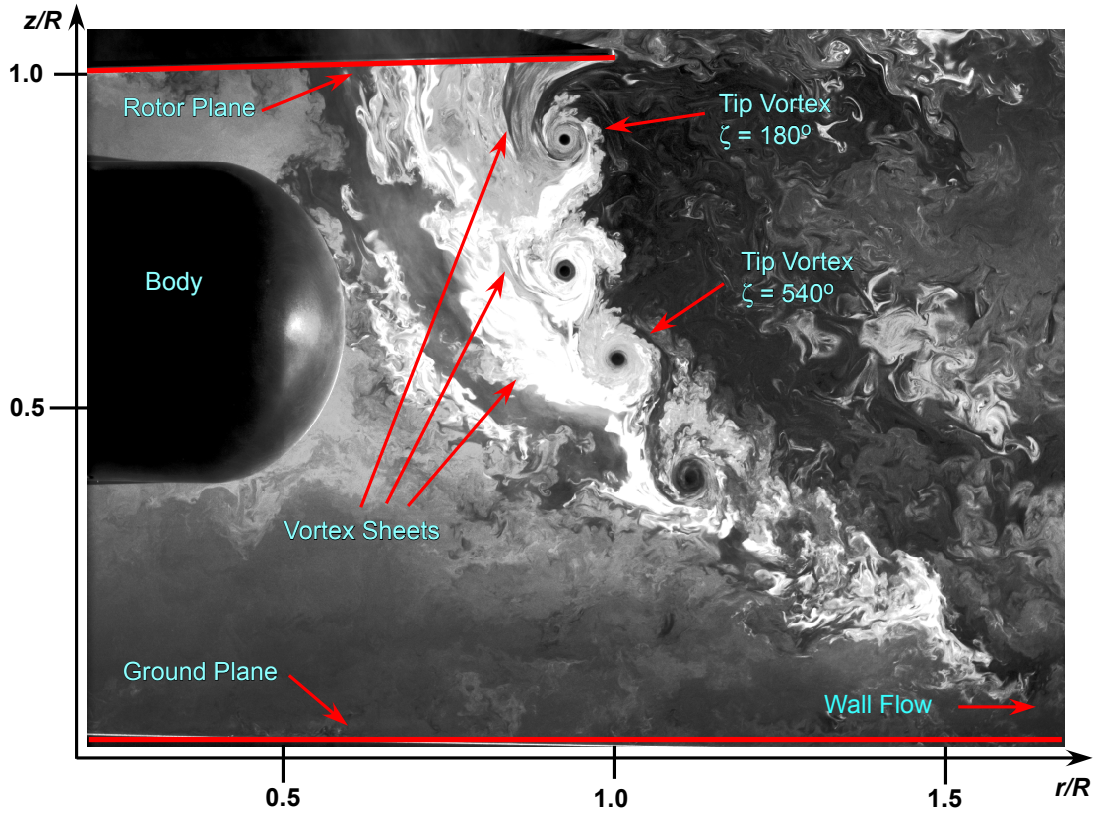

Figure 3.6: Flow visualization of the rotor wake over the nose of the body with the elliptical cross-section at a blade azimuth of $\psi_b = 0°$.

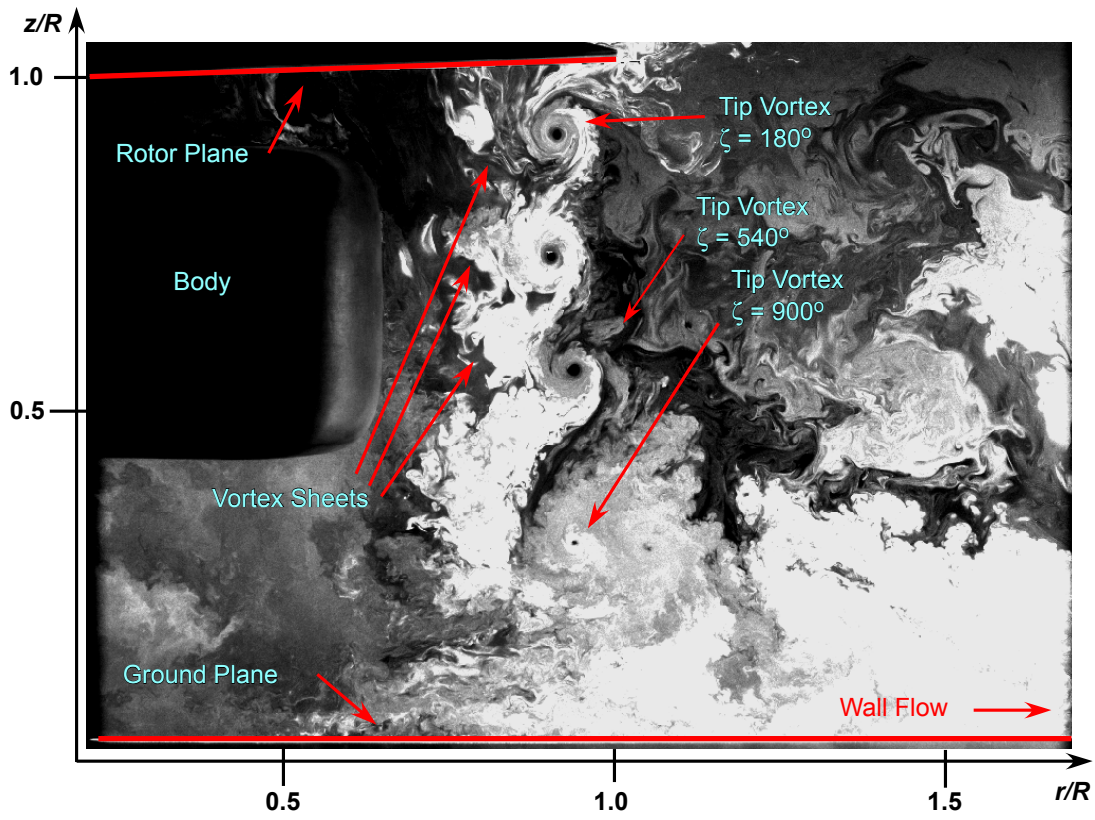

Figure 3.7: Flow visualization of the rotor wake over the nose of the body with the rectangular cross-section at a blade azimuth of $\psi_b = 0°$.

calculate the average spatial locations of the vortices in terms of their axial displacements below the rotor (or height from the ground plane) and distance from the rotational axis of the rotor. The centers of the vortices (i.e., the place where vorticity is at a maximum) were identified using the two-dimensional Q-criterion, which is discussed in Appendix A. This method was chosen because it can be used to accurately calculate the center of a vortex flow when using a minimum number of PIV realizations [12]. Using this method, vortex centers could be located to wake ages in excess of 1000°.

Figures 3.8 and 3.9 show the rotor wake geometry in terms of the radial and axial locations of the tip vortices at various wake ages. As shown in Fig 3.8, the radial locations of the wake were very similar for each of the three body shapes, as well as for the isolated rotor. However, the wake geometry produced with the body with the rectangular cross-section are located further inboard radially compared to the isolated rotor or the other bodies; these differences are particularly evident from $\zeta = 450°$ to $\zeta = 900°$. As shown in Fig. 3.9, the axial displacements of the wake in all cases are similar over a the range of wake ages that were measured.

Figure 3.10 shows the radial and axial locations of the vortices with respect to the rotor for the isolated rotor and beyond the nose of each of the body shapes. It can be seen that the wake in all cases is typical of a hovering rotor IGE. As was previously noted, a significant portion of the wake boundary for the body with the rectangular cross-section was noticeably further inboard compared to the wake boundaries that were obtained with the isolated rotor or with the other two bodies.

Flow visualization at the tail of each body in the rotor wake, which is given in Figs. 3.11 through 3.13, showed that the tip vortices impinged on the body in this case.

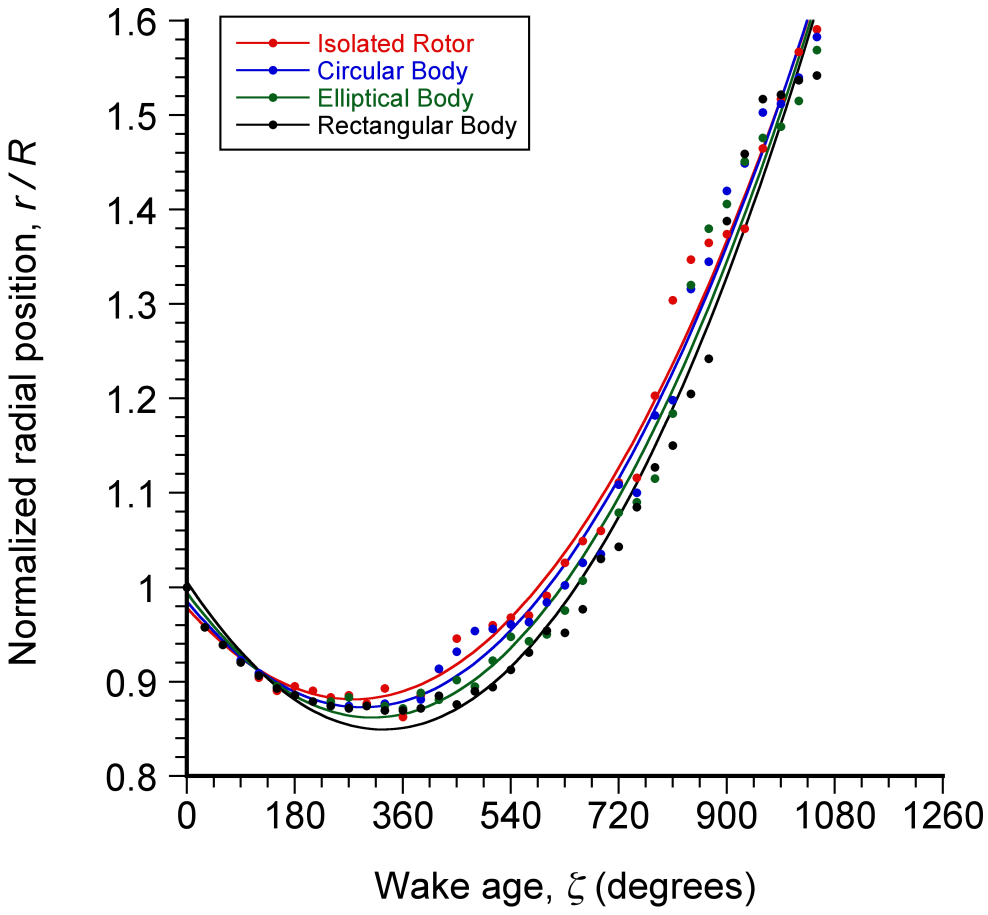

Figure 3.8: Tip vortex radial locations as a function of wake age, ζ, for the isolated rotor and at the nose (front) of each body. See Figs. 3.4–3.7.

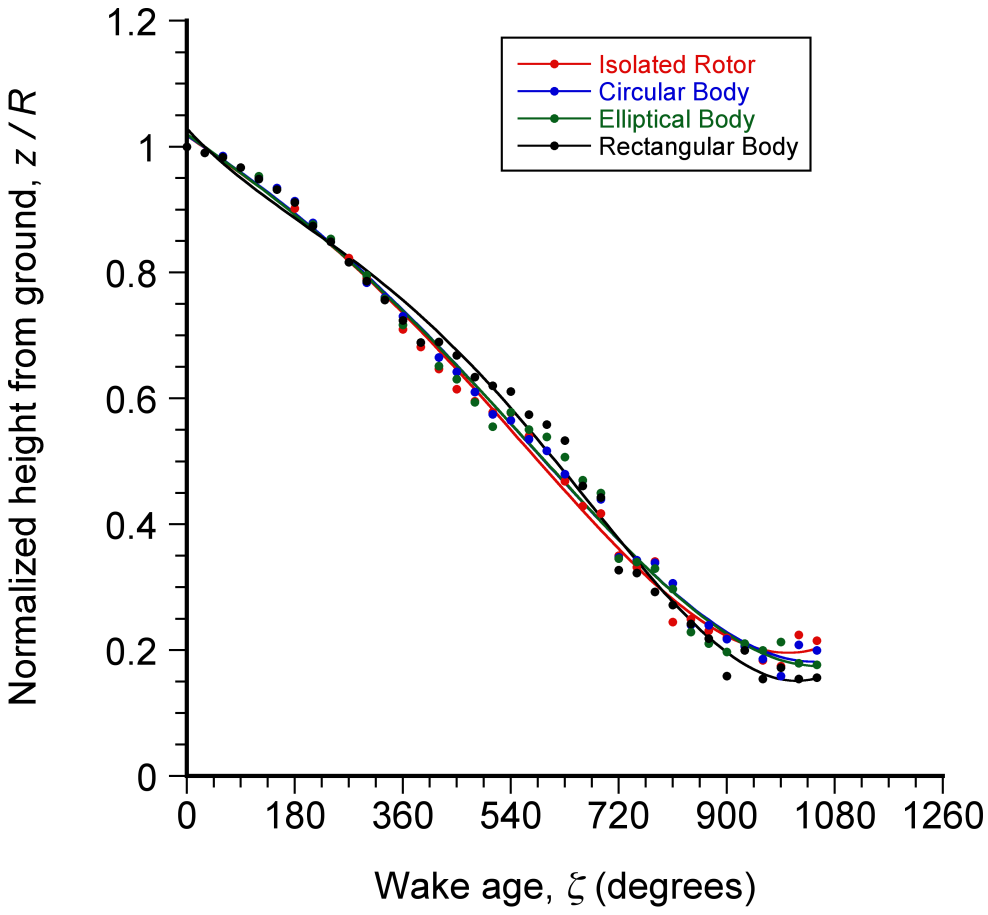

Figure 3.9: Tip vortex axial locations as a function of wake age, ζ, for the isolated rotor and at the nose (front) of each body. See Figs. 3.4–3.7.

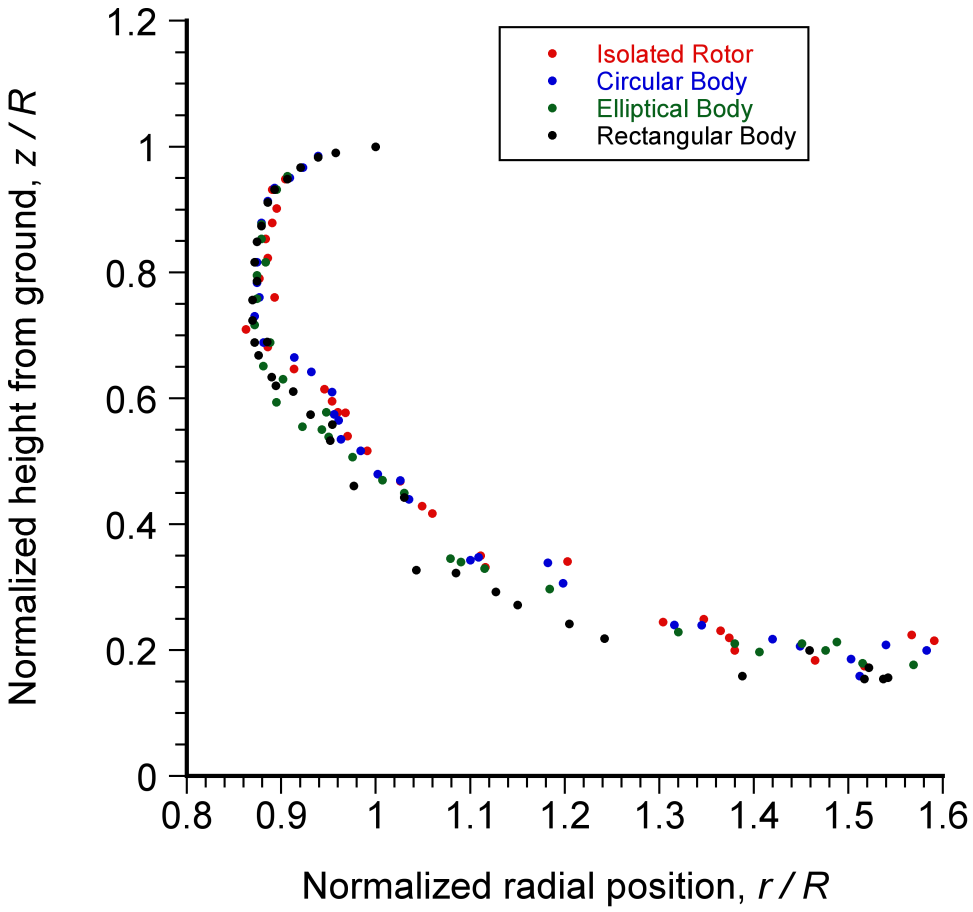

Figure 3.10: Axial and radial locations of the vortex centers along the wake boundary for the isolated rotor and at the nose (front) of each body. See Figs. 3.4–3.7.

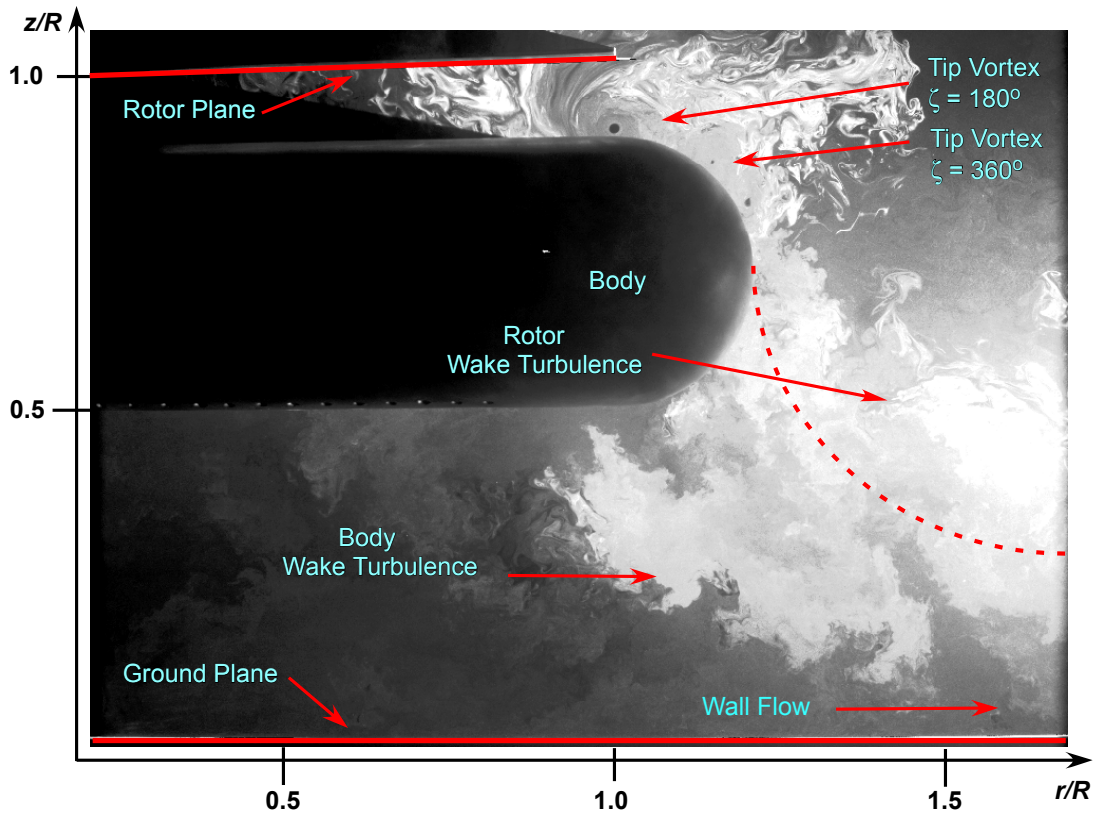

Figure 3.11: Flow visualization of the rotor wake over the tail (rear) of the body with the circular cross-section at a blade azimuth of $\psi_b = 0°$.

For the bodies with circular and elliptical cross-sections, the tip vortices could be seen to impinge upon the upper part of the body and then convect a short distance radially outward along the body surface. With the body with the rectangular cross-section, the vortices directly impinged upon the top of the body and then were very rapidly diffused, i.e., they effectively burst. In each case, there was a large area of turbulent flow below the body that resulted from the disrupted rotor wake.

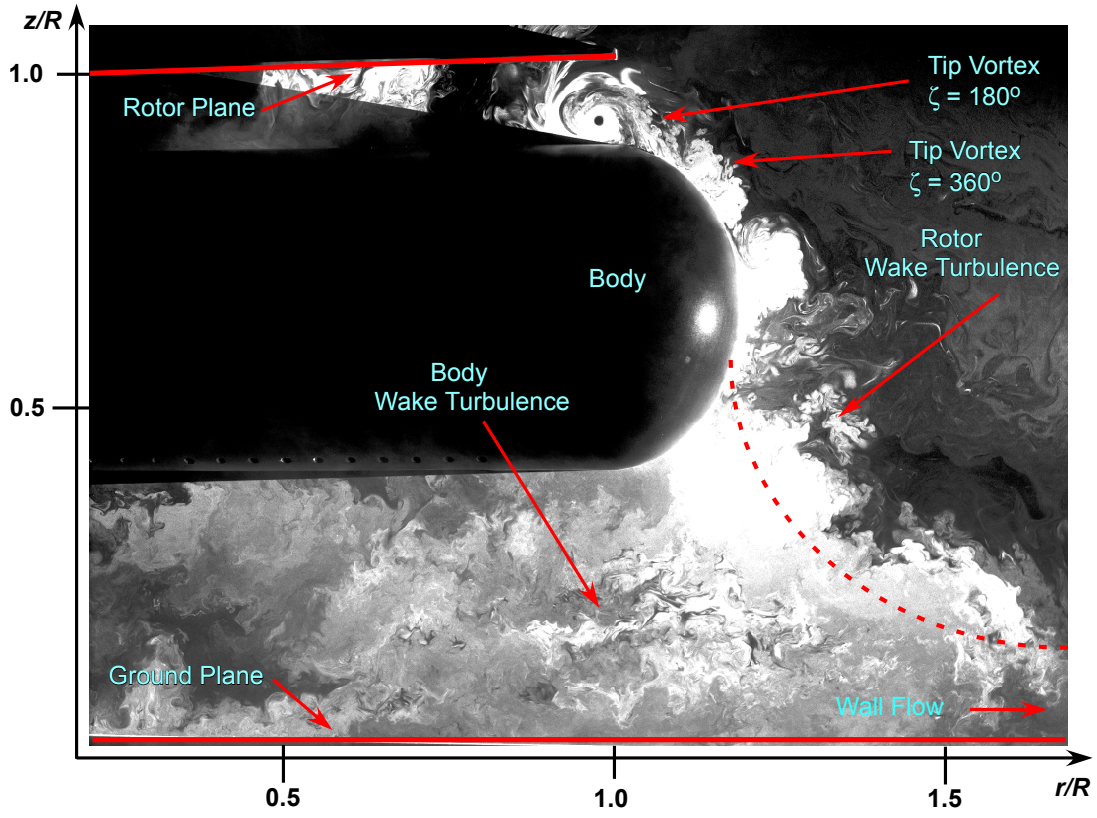

Figure 3.12: Flow visualization of the rotor wake over the tail (rear) of the body with the elliptical cross-section at a blade azimuth of $\psi_b = 0°$.

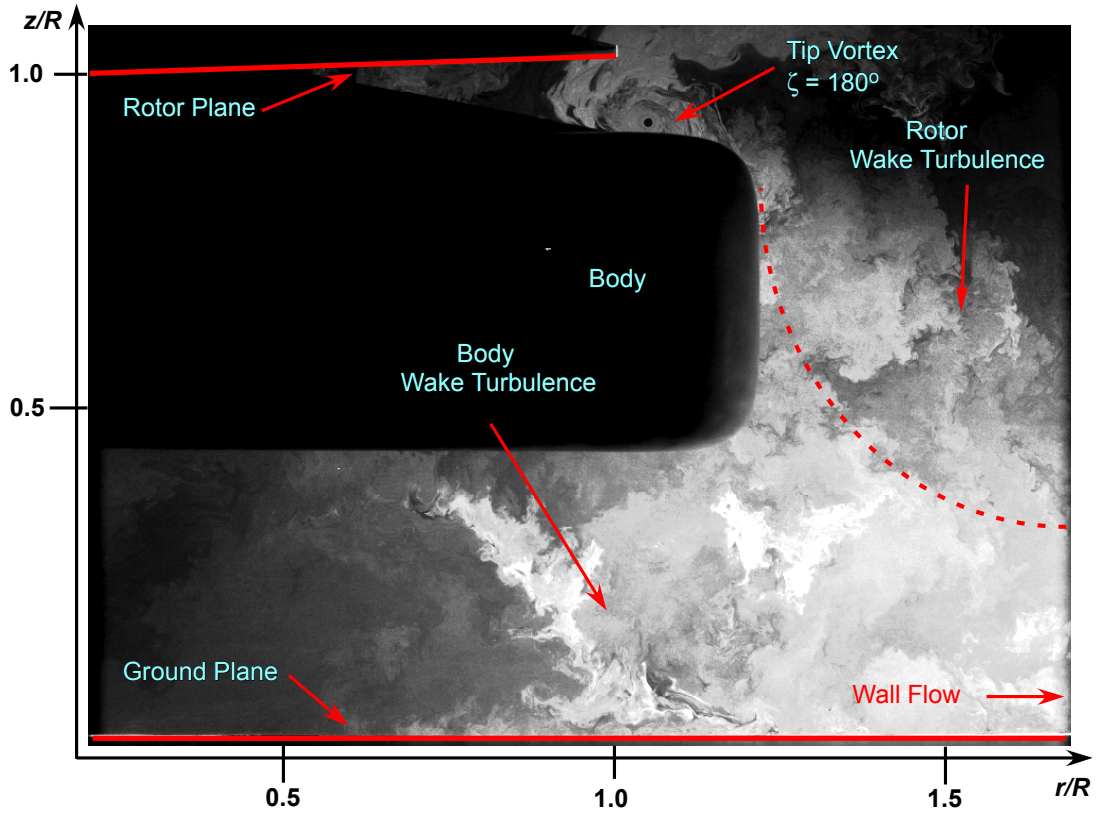

Figure 3.13: Flow visualization of the rotor wake over the tail (rear) of the body with the rectangular cross-section at a blade azimuth of $\psi_b = 0°$.

3.4 PIV Measurements

Using time-resolved ensemble averages of the PIV realizations in each ROI, it was possible to mosaic the different ROIs together to produce time-averaged velocities in a larger region of the rotor wake, similar to the larger ROI obtained using the FV. The time-averaging process can be used to calculate the average wake velocities over a full rotation of the rotor. Time-averaging was performed by first calculating the phase-resolved ensemble averages for each wake age, and then performing an ensemble average over the range of wake ages, i.e., using

$$\overline{U} = \sum_{\psi=0}^{\psi_{\text{final}}} \sum_{n=0}^{N_i} \overrightarrow{U} \tag{3.4}$$

where $\overline{U}$ is the time-averaged velocity, ψ is the wake age, N_i is the number of images, and $\overrightarrow{U}$ is the instantaneous velocity at each point in the flow. In this case, the value of ψ_{final} was 330°, representing one full revolution of the rotor. It was also necessary to position the separate ROI's together to establish a full flow field. For ROI positioning, the axial and radial locations of each ROI were measured and recorded. Small positioning adjustments were made by relocating the ROI's such that the velocity gradients in overlapping regions matched for different ROI's. The results in Fig. 3.14 show a time-averaged contour plot of the wake of the isolated rotor, the color of the contour corresponding to the magnitude of the velocity at that point.

The results shown in Figs. 3.15 through 3.17 indicate that the flows over the front of the bodies were similar to that of the isolated rotor. However, the flow over the bodies with the circular and elliptical cross-sections had slightly higher velocities as the flow neared the ground. In the case of the bodies with elliptical and circular cross-sections, the

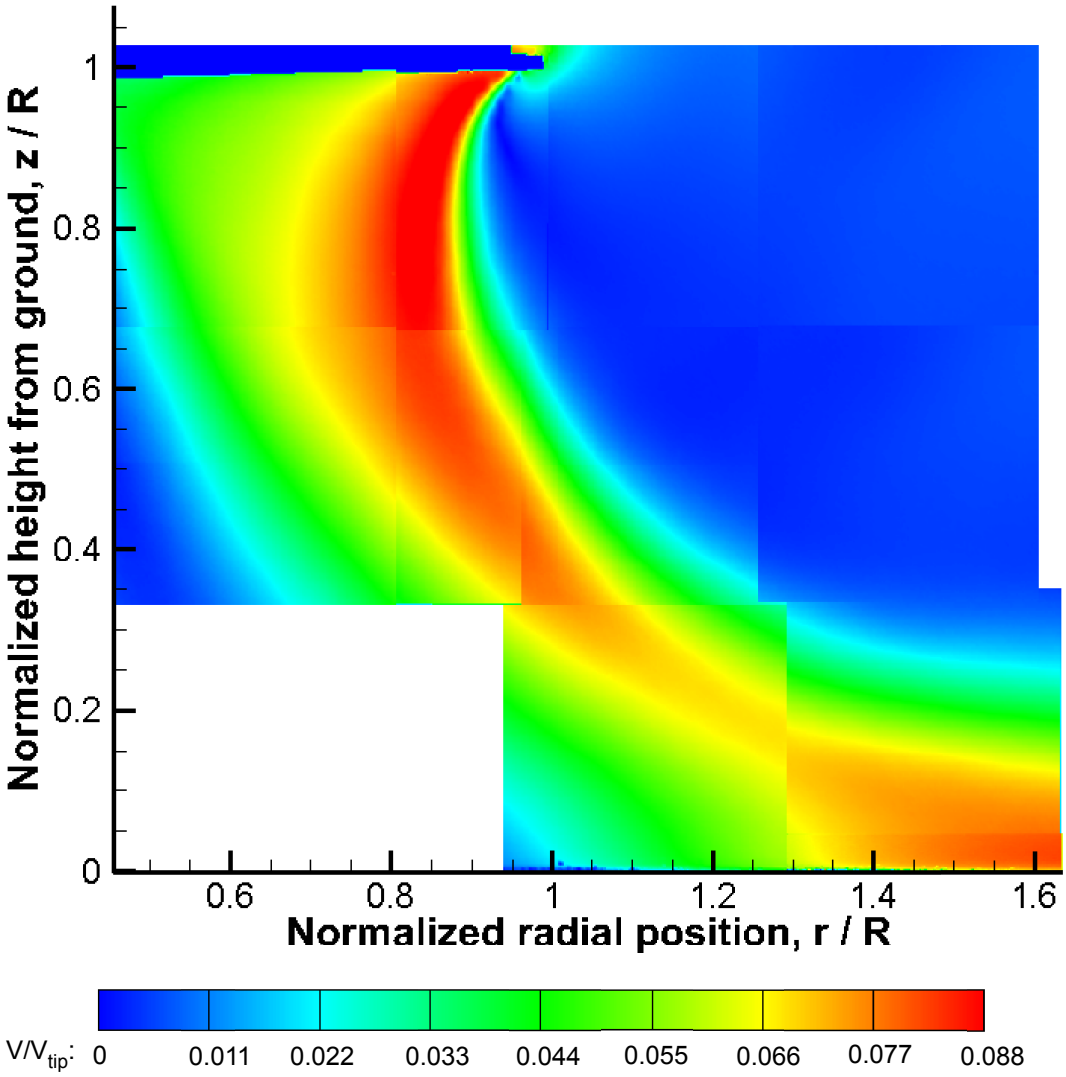

Figure 3.14: Time-averaged PIV measurements of the rotor wake for the isolated rotor.

flow appeared to separate from the body surface approximately midway down the body and close to its longitudinal centerline. flow separation was a consequence of the adverse pressure gradient that is generated as the body curves away from the flow. The wake around the body with the rectangular cross-section, however, showed regions of higher flow velocity over the body surface, which is expected as the rectangular cross-section does not curve away from the flow until near the bottom of the body. Clearly, the onset of this flow separation poses a significant modelling difficulty. As the flow neared the ground plane and turned more radially outward, regions of higher flow velocity were also found closer to the ground plane than with the isolated rotor or with the other body shapes. It is also important to note that the flow remained attached to the surface of the body with the rectangular cross-section for a greater downstream distance and, therefore, it separated later and produced a different wake size.

An examination of the time-averaged flow over the rear of the bodies, as shown in Figs. 3.18 through 3.20, helps to clarify and quantify the observations made with the FV. For the bodies with circular and elliptical cross-sections, an area of separated flow can be seen with the point of flow separation occurring close to the bottom of the body at a height of approximately $z/R = 0.5$ from the ground plane. Near the ground, there is a large region of lower-speed flow, which eventually reorganizes to form a wall jet flow with similar velocities to the wall-parallel flow found below the nose of the bodies; see Figs. 3.15 through 3.17. With the body with the rectangular cross-section, the flow separated from the upper corner of the body (Fig. 3.20), and remained separated thereafter. At more radially outboard locations the flow at the ground plane below the body with the rectangular cross-section was found to be of lower velocity than was obtained with the

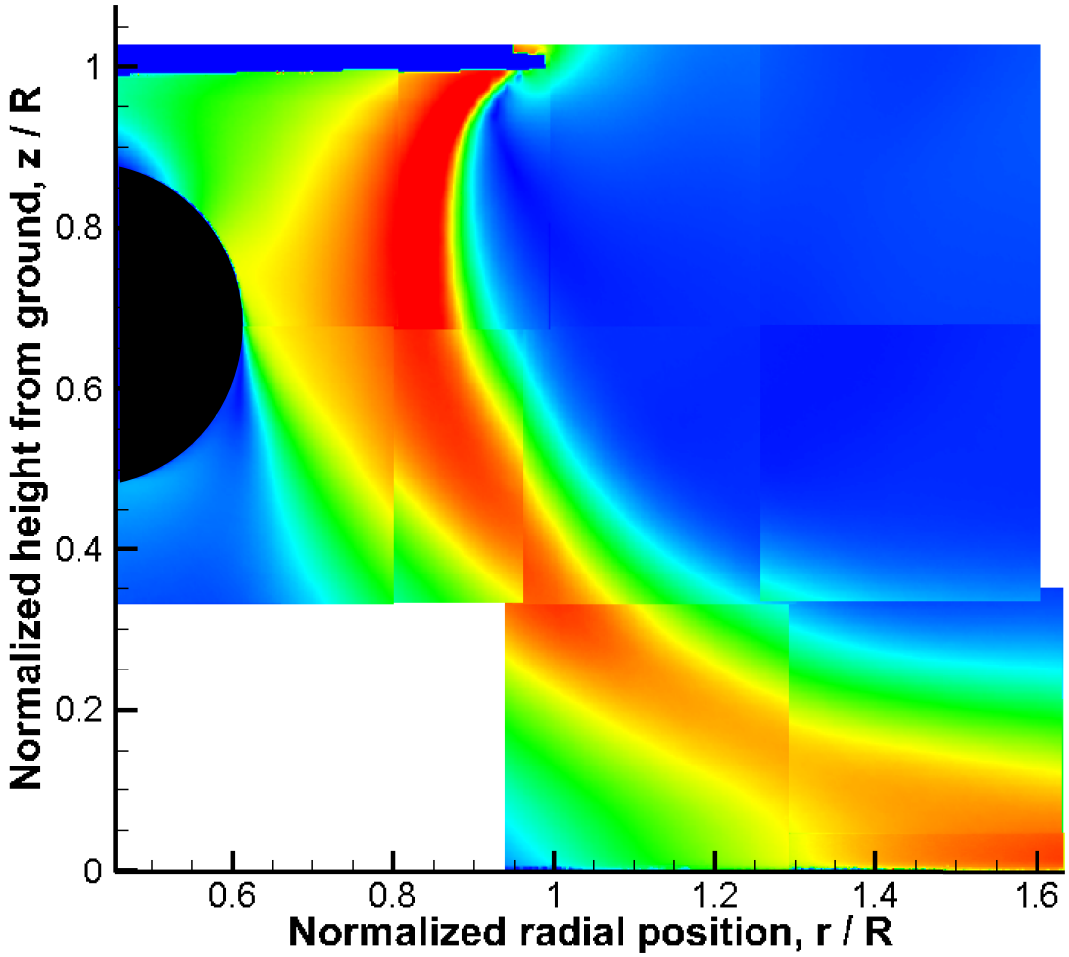

Figure 3.15: Time-averaged PIV measurements of the rotor wake over the nose of the body with the circular cross-section.

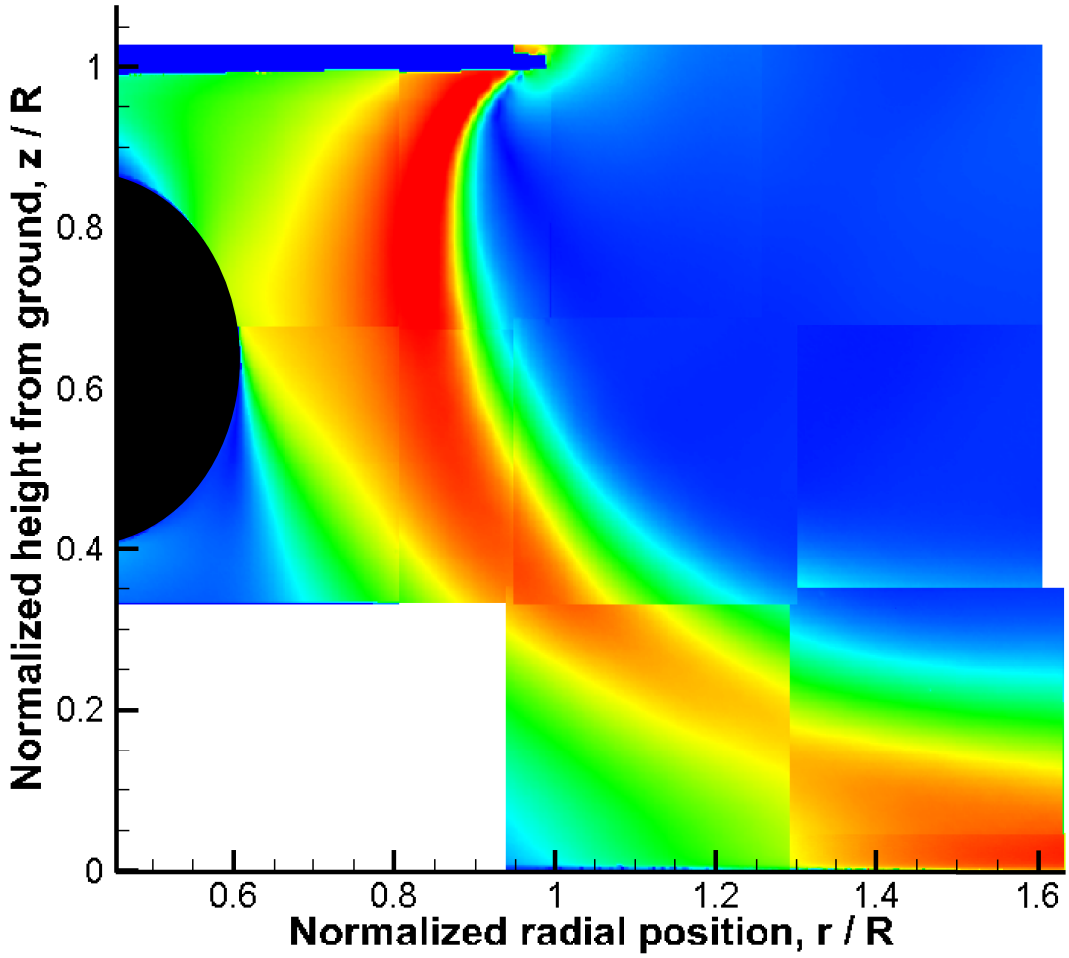

Figure 3.16: Time-averaged PIV measurements of the rotor wake over the nose of the body with the elliptical cross-section.

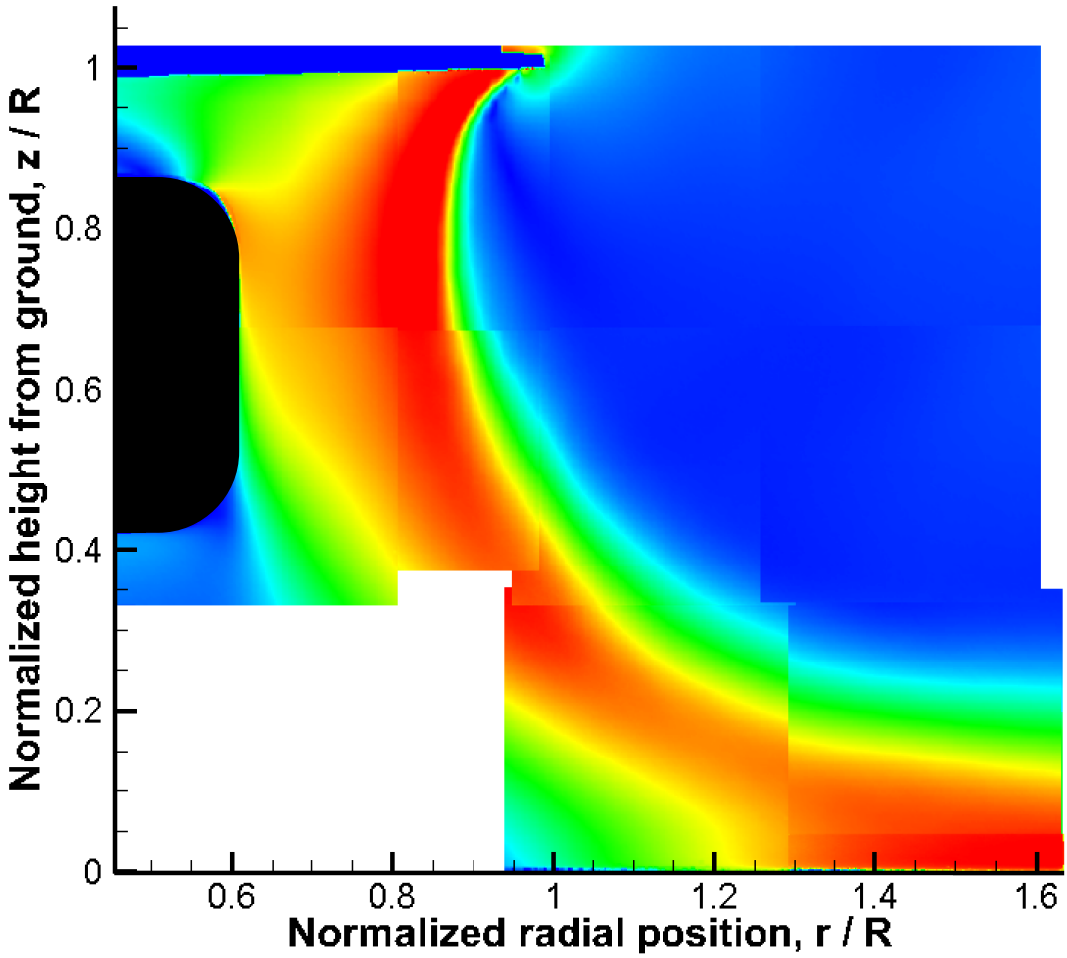

Figure 3.17: Time-averaged PIV measurements of the rotor wake over the nose of the body with the rectangular cross-section.

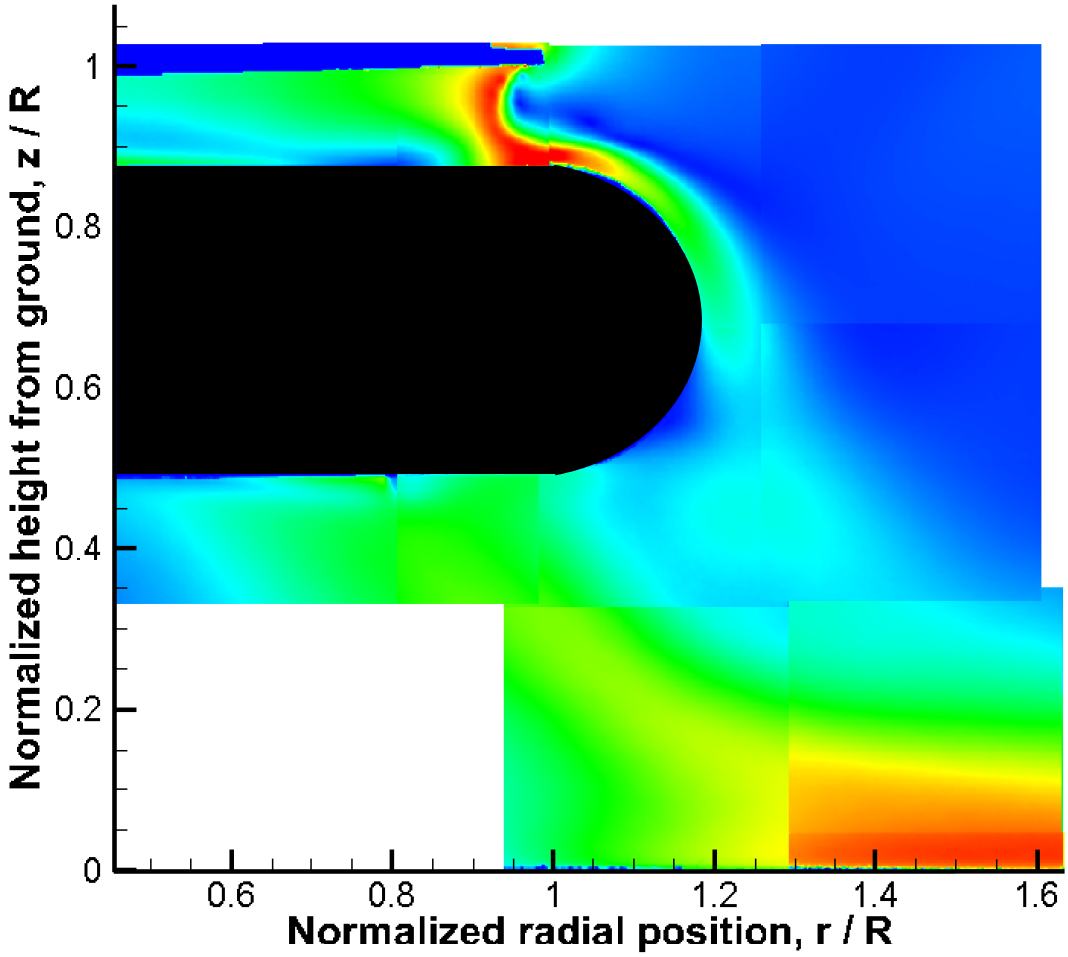

Figure 3.18: Time-averaged PIV measurements of the rotor wake over the tail of the body with the circular cross-section.

isolated rotor or with the other two bodies Figs. 3.18 and 3.19.

3.5 Details of the Flow at the Ground Plane

Figure 3.21 shows a schematic of the general flow field observed as the rotor wake convected toward the ground plane. This figure shows the ROIs where PIV measurements were performed, as well as the positions where velocity cuts were made. In this region near the ground, the rotor wake interacts with the ground plane causing the flow to rapidly

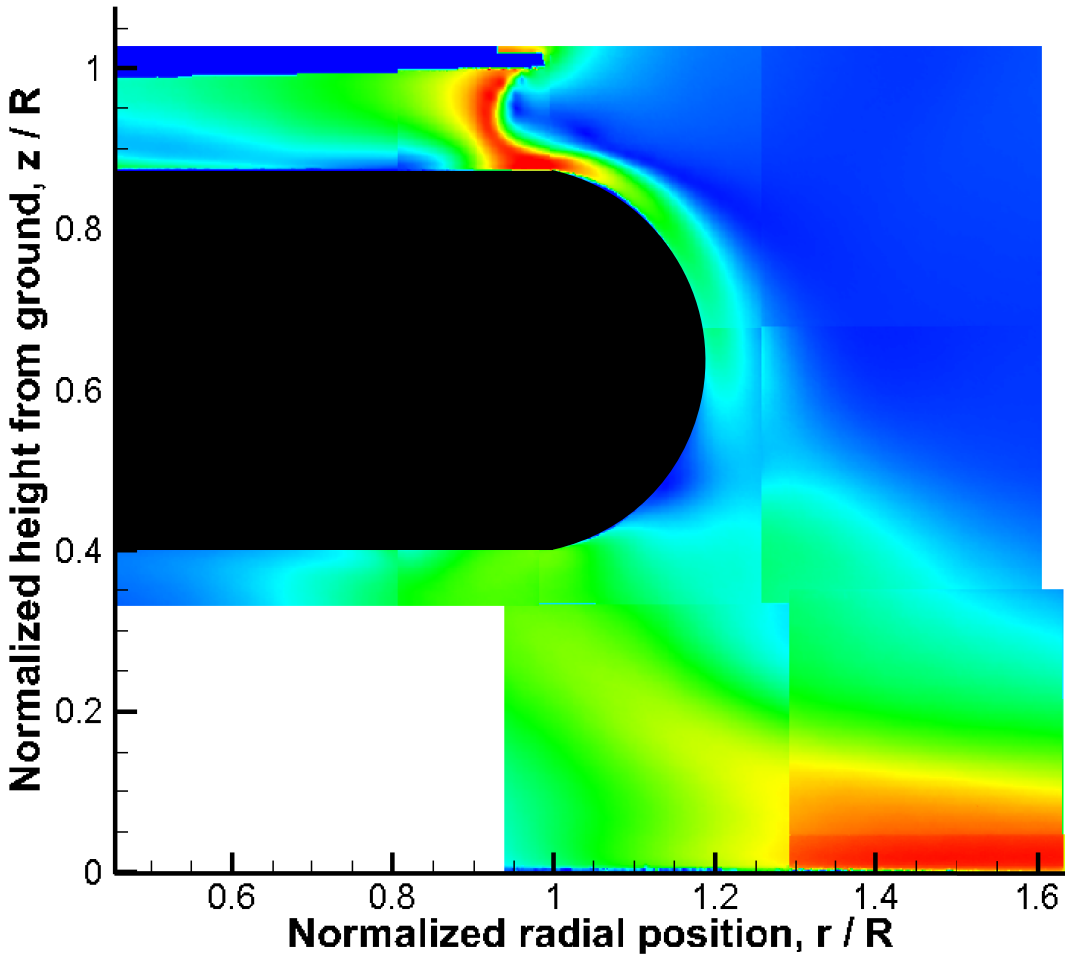

Figure 3.19: Time-averaged PIV measurements of the rotor wake over the tail of the body with the elliptical cross-section.

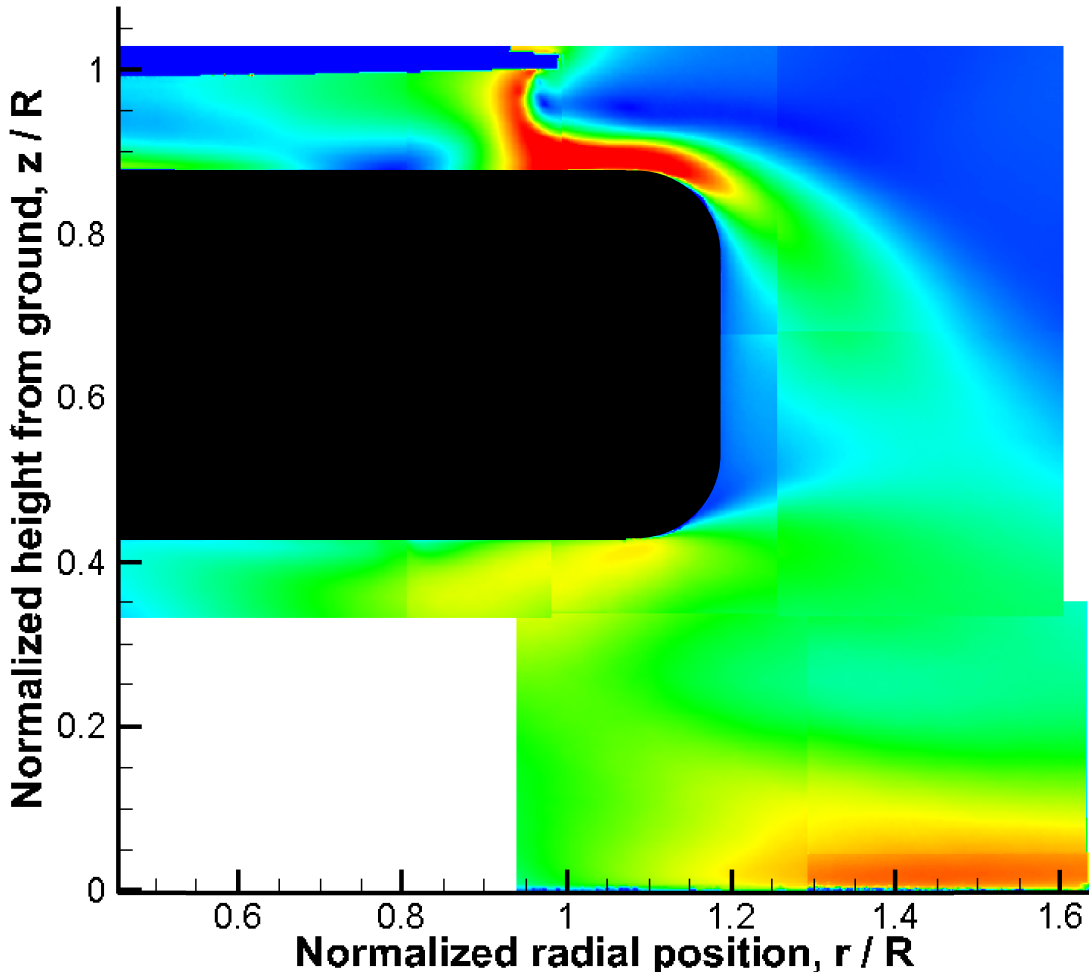

Figure 3.20: Time-averaged PIV measurements of the rotor wake over the tail of the body with the rectangular cross-section.

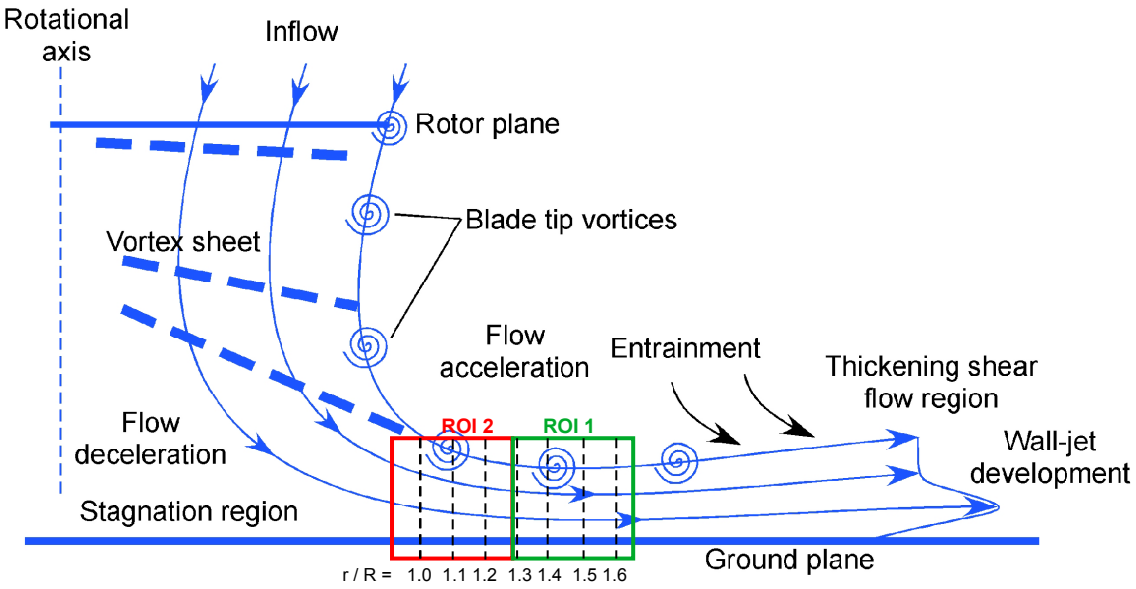

Figure 3.21: Schematic of the flow as it interacts with the ground plane showing the ROIs and positions where velocity profile cuts were made.

turn and flow outward, as well as stretching and intensifying the vortex filaments [11]. As the flow convects radially outward, it begins to develop into a wall jet type of flow. Previous work has shown that if the wall jet is viewed as boundary layer region supplied with momentum from the rotor, the local velocities are greater than the velocities in the upstream flow [66, 67]. In this case, the wall jet also contains significant vorticity that originated in the rotor wake, i.e., the tip vortices and the turbulent vortex sheets.

Time-averaged and instantaneous wall-parallel velocity profiles were obtained close to the surface of the ground. Figure 3.23 shows the time-averaged measurements of the radial flow velocities generated by the rotor at several downstream distances beyond the nose of each of the three body shapes. The slight discontinuities seen in these results are because of the change of the grid near the ground plane; the grid was altered as needed to obtain higher spatial resolution at locations very close to the ground.

At more radially inboard locations, the velocity profiles do not yet resemble those of a fully-developed turbulent wall jet, i.e., the profile shown in Fig. 3.22. At these locations, the flow is still turning from a mostly downward to an outward direction as it begins to interact with the ground plane. As the flow moves farther outward along the ground plane, the velocity profiles begin to resemble a more classical type of wall jet profile [68, 69]. As shown in Fig. 3.23, the velocity profiles below the nose of each of the three bodies are similar in shape to the velocity profiles generated by the isolated rotor. It is interesting to note that at $r/R = 1.6$, the bodies with the circular and elliptical cross-sections also produce velocities that are very similar in magnitude and form to those produced by the isolated rotor. However, it can be seen that at all radial locations the body with the rectangular cross-section produces a wall-parallel velocity of noticeably higher magnitude.

In Fig. 3.24, the time-averaged, wall-parallel velocity profiles near the ground at the tail of each body are shown. In this case, the profiles at the ground obtained with each body shape differed significantly from those obtained with the isolated rotor. Specifically, at the more inboard radial locations the flow under the bodies showed higher velocities near the ground plane. These differences are a result of the large scale disruption of the rotor wake that is caused by the presence of the body.

As the flow then moves radially outward along the ground plane, the flow begins to develop into a profile that is more similar to a classical wall jet. For each of the three body shapes, the profile develops more slowly and still shows some differences to the fully developed wall jet flow at $r/R = 1.6$. It is interesting to notice, however, that the maximum velocities at $r/R = 1.6$ are similar to the maximum wall-parallel velocities that

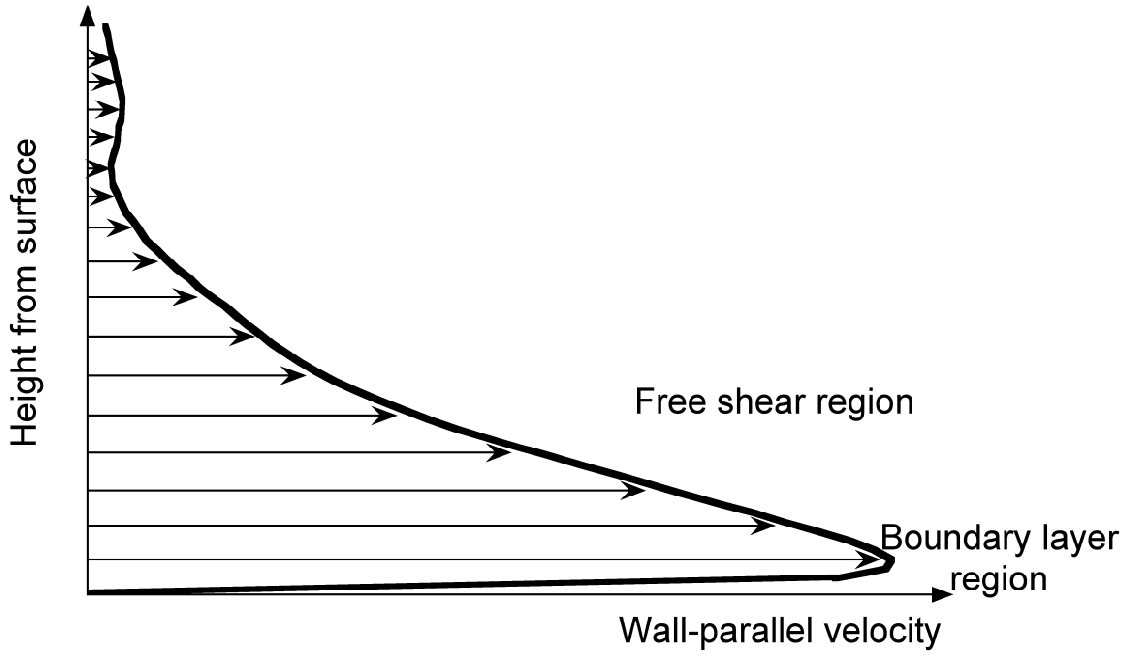

Figure 3.22: Wall-parallel velocity profile of a classical wall jet.

were obtained with the isolated rotor, as well as to the flow that was measured downstream of the nose of each body.

Figure 3.25 shows instantaneous velocity profiles of the wall-parallel velocity for the isolated rotor and at the nose of each body. These profiles now include stochastic effects such as those produced by the localized turbulence and the tip vortices that have been removed in the time-averaging process. For each body shape in turn, the instantaneous image with the largest velocity excursions was selected. This means that each velocity profile corresponds to a different wake age, and so the flows are not necessarily temporally correlated. The magnitude of the maximum fluctuations was found to be similar for the isolated rotor and for each body shape. The largest fluctuations shown in these profiles the consequence of a blade tip vortex present in the flow. The smaller fluctuations shown in Fig. 3.25 are the result of eddies and turbulence produced by the interactions of

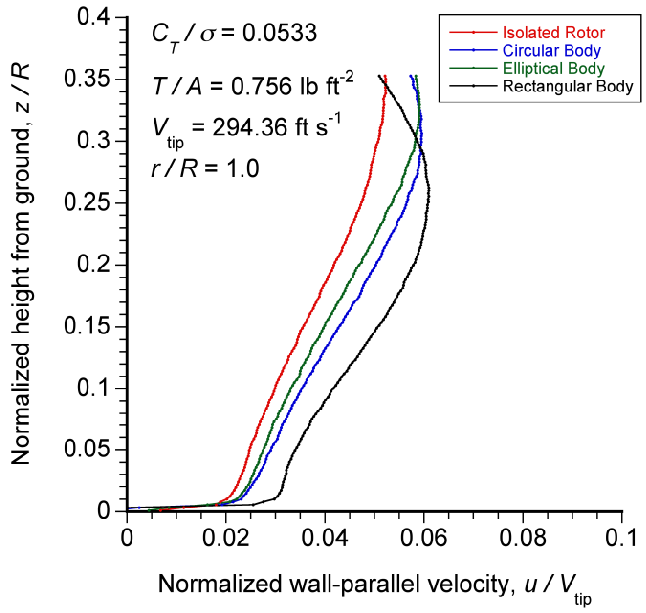

(a) $r/R = 1.0$

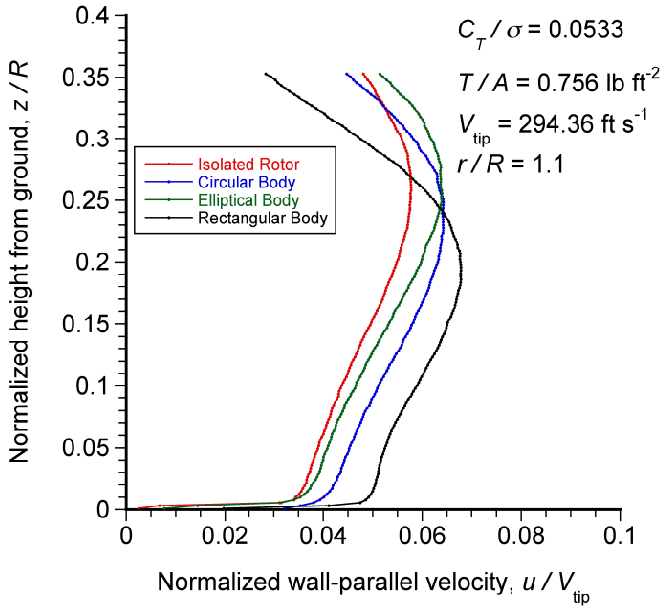

(b) $r/R = 1.1$

Figure 3.23: Time-averaged measurements of the wall-parallel flow for the isolated rotor and below the nose of each body at several downstream distances: (a) $r/R = 1.0$; (b) $r/R = 1.1$; (c) $r/R = 1.2$; (d) $r/R = 1.3$; (e) $r/R = 1.4$; (f) $r/R = 1.5$; (g) $r/R = 1.6$.

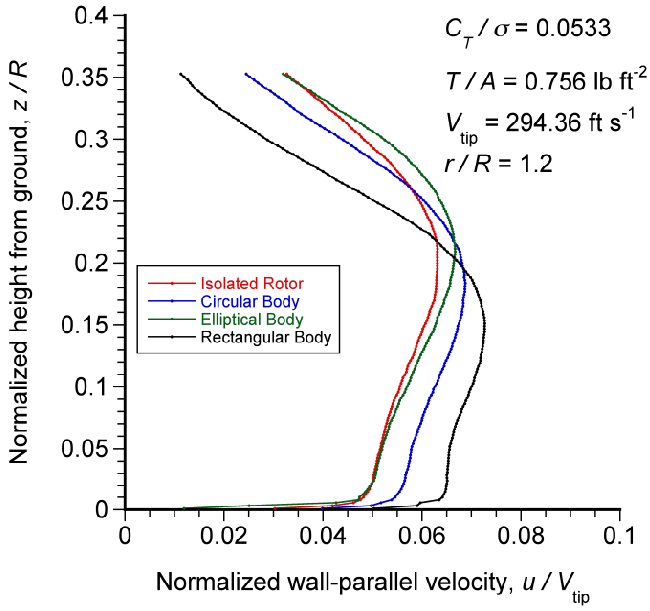

(c) $r/R = 1.2$

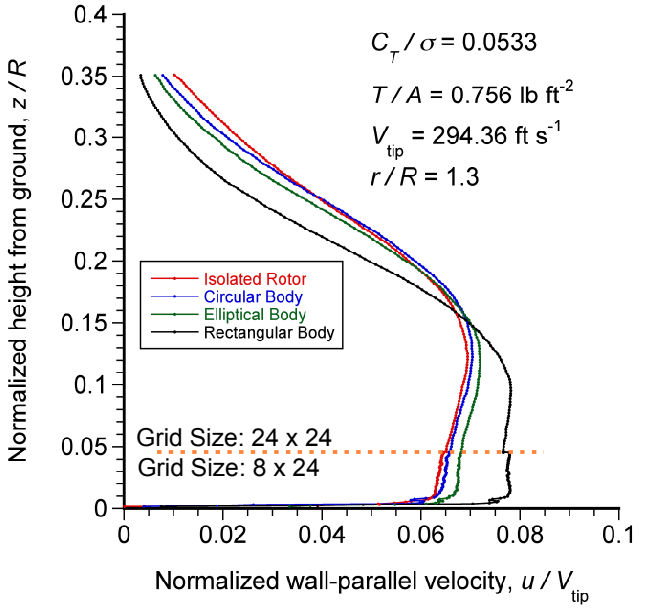

(d) $r/R = 1.3$

Figure 3.23: Time-averaged measurements of the wall-parallel flow for the isolated rotor and below the nose of each body at several downstream distances: (a) $r/R = 1.0$; (b) $r/R = 1.1$; (c) $r/R = 1.2$; (d) $r/R = 1.3$; (e) $r/R = 1.4$; (f) $r/R = 1.5$; (g) $r/R = 1.6$.

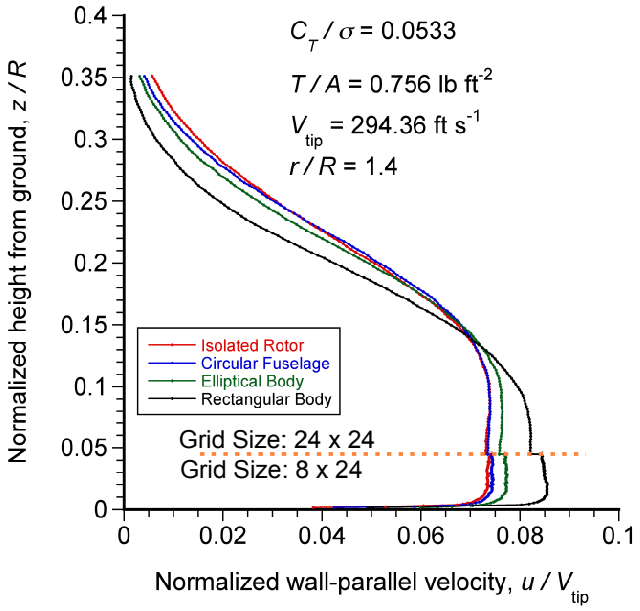

(e) $r/R = 1.4$

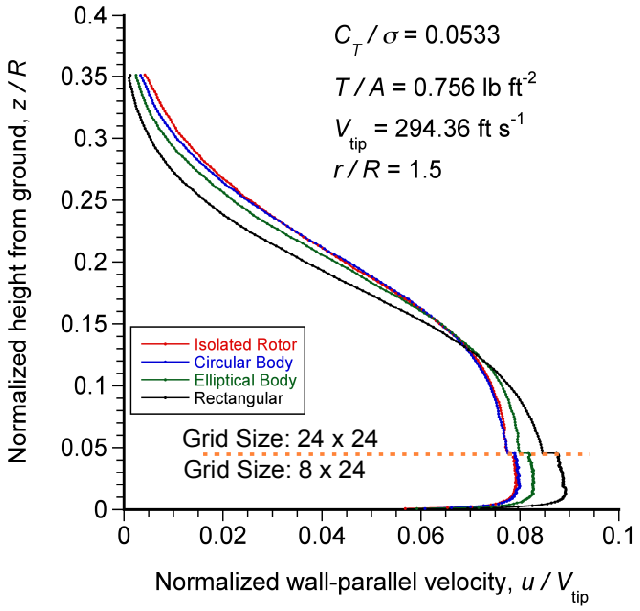

(f) $r/R = 1.5$

Figure 3.23: Time-averaged measurements of the wall-parallel flow for the isolated rotor and below the nose of each body at several downstream distances: (a) $r/R = 1.0$; (b) $r/R = 1.1$; (c) $r/R = 1.2$; (d) $r/R = 1.3$; (e) $r/R = 1.4$; (f) $r/R = 1.5$; (g) $r/R = 1.6$.

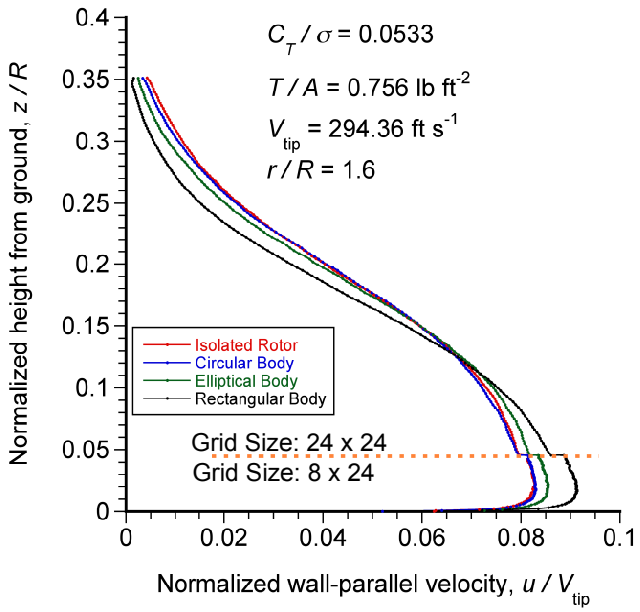

(g) $r/R = 1.6$

Figure 3.23: Time-averaged measurements of the wall-parallel flow for the isolated rotor and below the nose of each body at several downstream distances: (a) $r/R = 1.0$; (b) $r/R = 1.1$; (c) $r/R = 1.2$; (d) $r/R = 1.3$; (e) $r/R = 1.4$; (f) $r/R = 1.5$; (g) $r/R = 1.6$.

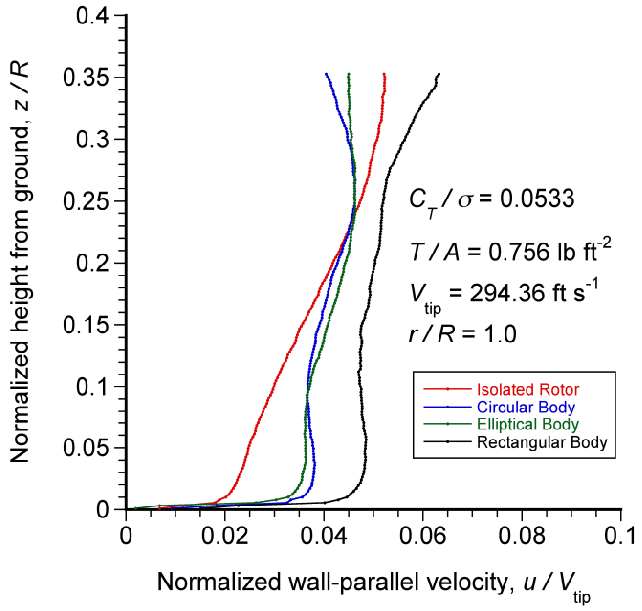

(a) $r/R = 1.0$

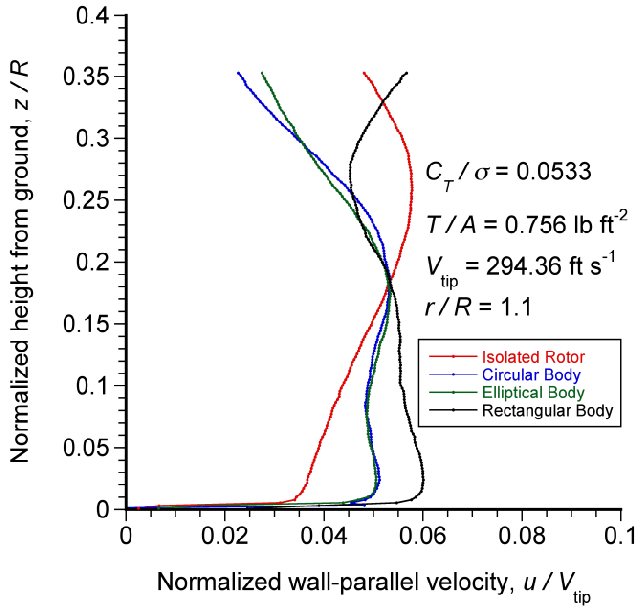

(b) $r/R = 1.1$

Figure 3.24: Time-averaged measurements of the wall-parallel flow for the isolated rotor and below the tail of each body at several downstream distances: (a) $r/R = 1.0$; (b) $r/R = 1.1$; (c) $r/R = 1.2$; (d) $r/R = 1.3$; (e) $r/R = 1.4$; (f) $r/R = 1.5$; (g) $r/R = 1.6$.

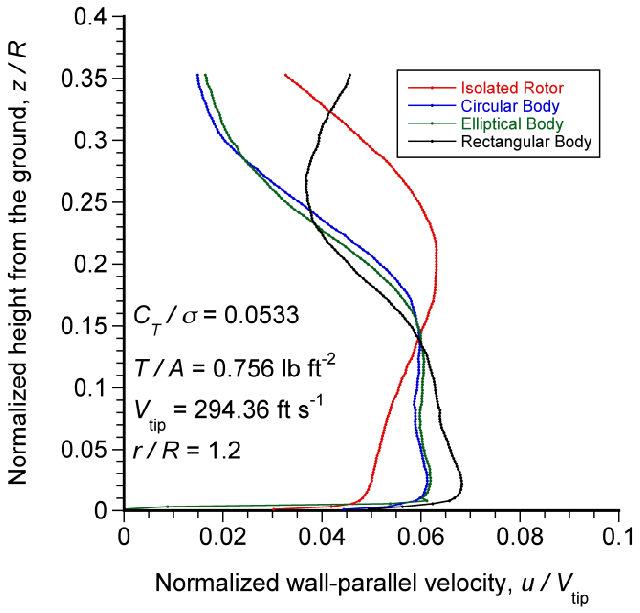

(c) $r/R = 1.2$

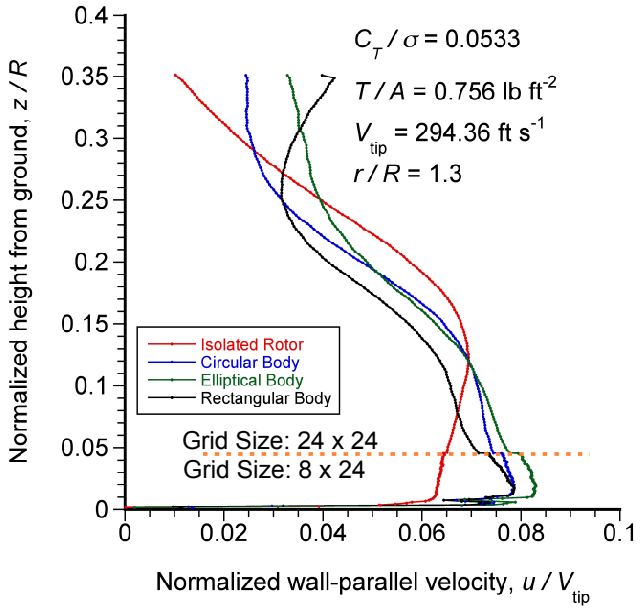

(d) $r/R = 1.3$

Figure 3.24: Time-averaged measurements of the wall-parallel flow for the isolated rotor and below the tail of each body at several downstream distances: (a) $r/R = 1.0$; (b) $r/R = 1.1$; (c) $r/R = 1.2$; (d) $r/R = 1.3$; (e) $r/R = 1.4$; (f) $r/R = 1.5$; (g) $r/R = 1.6$.

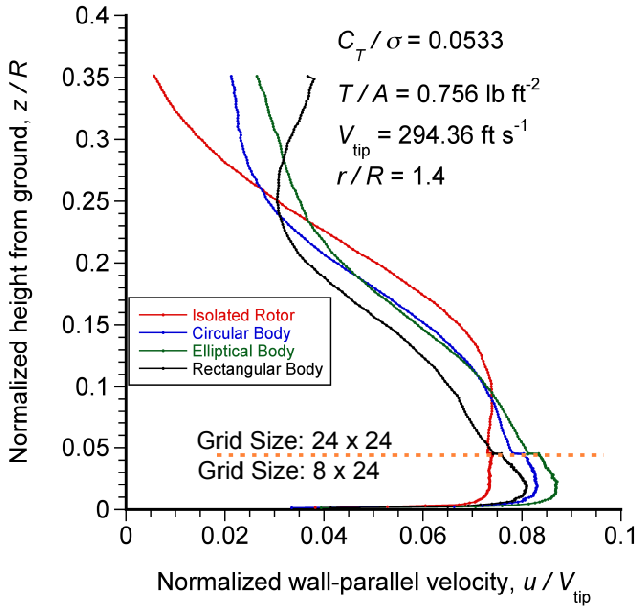

(e) $r/R = 1.4$

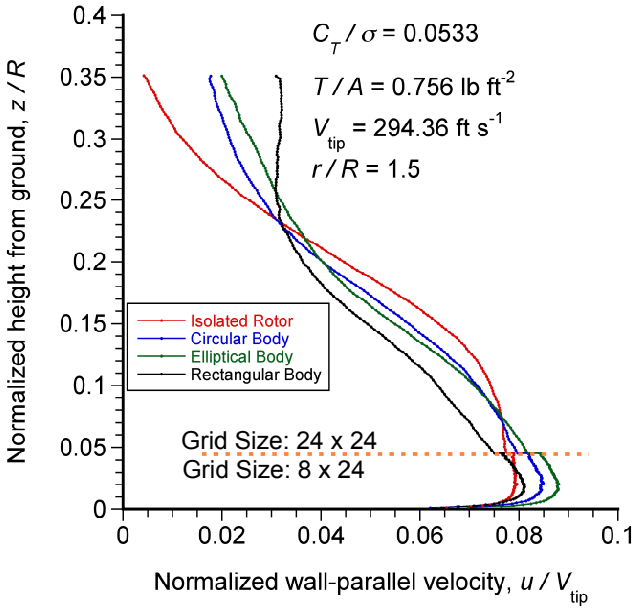

(f) $r/R = 1.5$

Figure 3.24: Time-averaged measurements of the wall-parallel flow for the isolated rotor and below the tail of each body at several downstream distances: (a) $r/R = 1.0$; (b) $r/R = 1.1$; (c) $r/R = 1.2$; (d) $r/R = 1.3$; (e) $r/R = 1.4$; (f) $r/R = 1.5$; (g) $r/R = 1.6$.

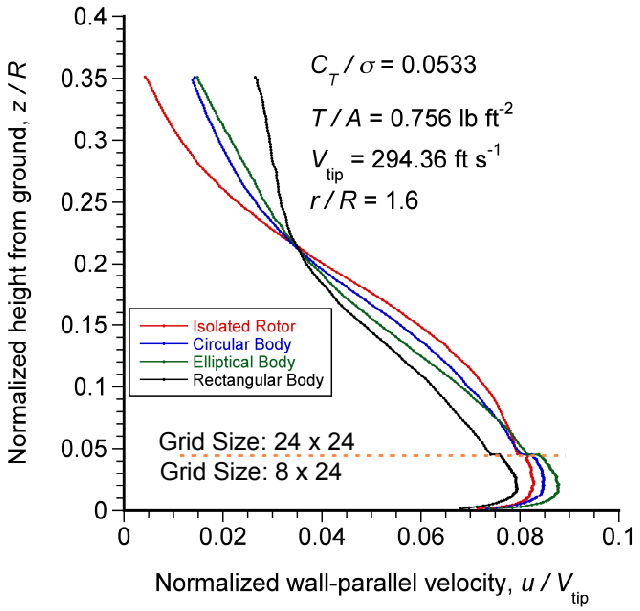

(g) $r/R = 1.6$

Figure 3.24: Time-averaged measurements of the wall-parallel flow for the isolated rotor and below the tail of each body at several downstream distances: (a) $r/R = 1.0$; (b) $r/R = 1.1$; (c) $r/R = 1.2$; (d) $r/R = 1.3$; (e) $r/R = 1.4$; (f) $r/R = 1.5$; (g) $r/R = 1.6$.

the rotor wake with the ground. It is interesting to note that for each case, the velocity profiles at $r/R = 1.6$ are dominated by turbulence in the flow rather than the effects of any coherent vortices.

In Fig. 3.26, the corresponding instantaneous velocity profiles of the wall-parallel velocity downstream of the tail each body are shown. As mentioned previously in Section 3.3, the tip vortices impinge on the rear of the body just below the rotor tip, and quickly diffuse thereafter. Therefore, as shown in Fig. 3.26, the velocity profiles to the rear of the bodies become dominated by the effects of turbulence. In this case, however, the fluctuations from turbulence are larger than was seen in front of each of the bodies; this turbulence is a consequence of the disruption of the slipstream boundary of the rotor and the turbulent wake produced below the bodies.

Measurements were also made of the wall-normal (axial) velocities at the various radial locations near the ground. Figure 3.27 shows the normalized wall-normal velocity at the points of interest. At inboard radial locations, the rectangular and circular cross-sections produce higher velocity magnitudes near the ground than the isolated rotor and the body with the elliptical cross-section. At farther downstream radial distances, the wall-normal velocity profiles converge. This suggests that the effects of a body below the rotor is limited to inboard radial locations.

In Fig. 3.28, the wall-normal velocity profiles are shown for near ground locations at the rear of each body. It is immediately clear that the wall-normal flow below the tail of the bodies with the circular and elliptical cross-sections produce lower velocity magnitudes than for the isolated rotor at inboard radial locations. The profiles obtained with these two body shapes are very similar. The body with the rectangular cross-section

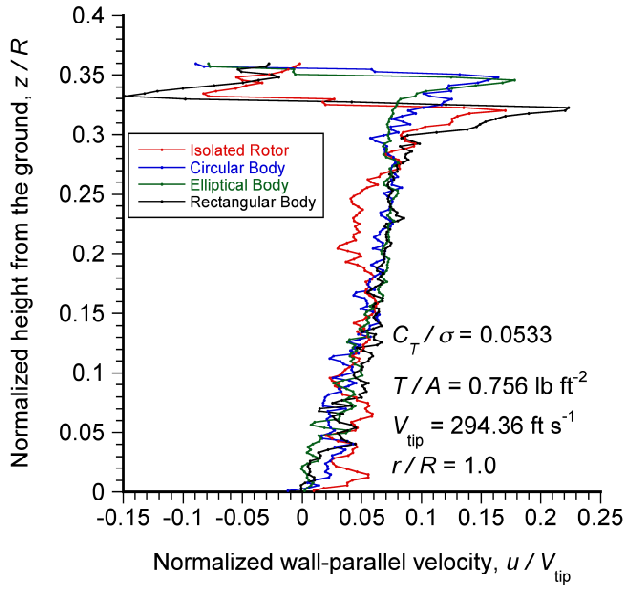

(a) $r/R = 1.0$

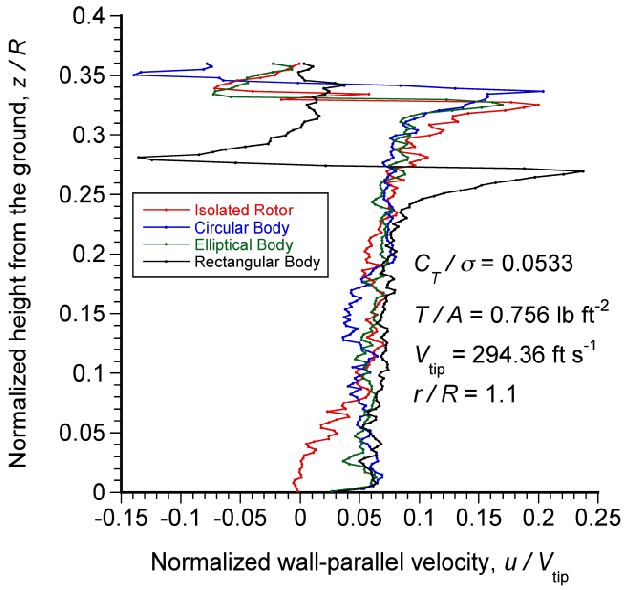

(b) $r/R = 1.1$

Figure 3.25: Instantaneous measurements of the wall-parallel flow for the isolated rotor and below the nose of each body at several downstream distances: (a) $r/R = 1.0$; (b) $r/R = 1.1$; (c) $r/R = 1.2$; (d) $r/R = 1.3$; (e) $r/R = 1.4$; (f) $r/R = 1.5$; (g) $r/R = 1.6$.

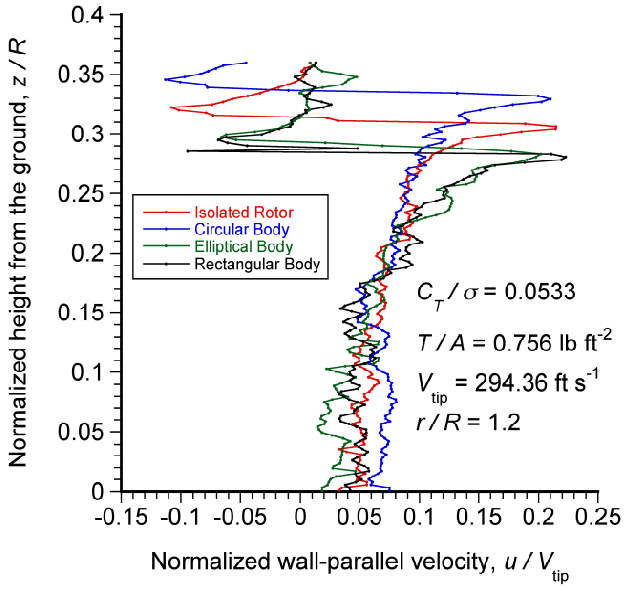

(c) $r/R = 1.2$

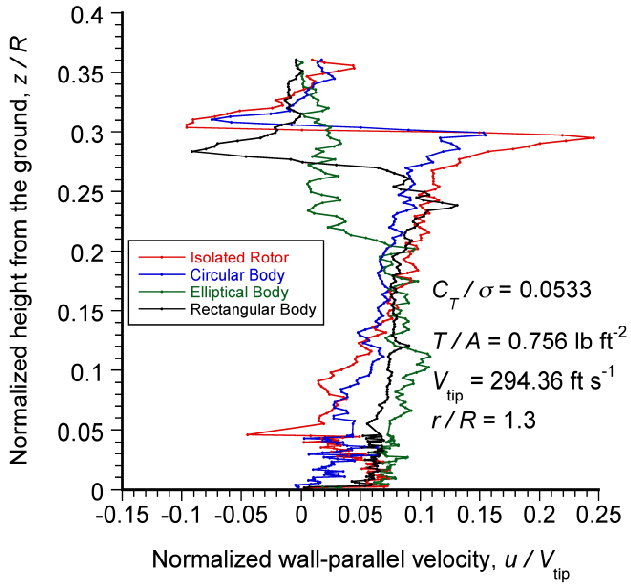

(d) $r/R = 1.3$

Figure 3.25: Instantaneous measurements of the wall-parallel flow for the isolated rotor and below the nose of each body at several downstream distances: (a) $r/R = 1.0$; (b) $r/R = 1.1$; (c) $r/R = 1.2$; (d) $r/R = 1.3$; (e) $r/R = 1.4$; (f) $r/R = 1.5$; (g) $r/R = 1.6$.

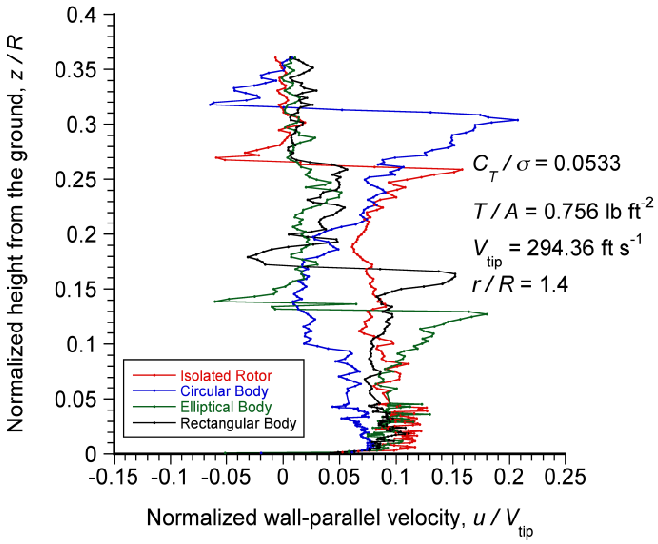

(e) $r/R = 1.4$

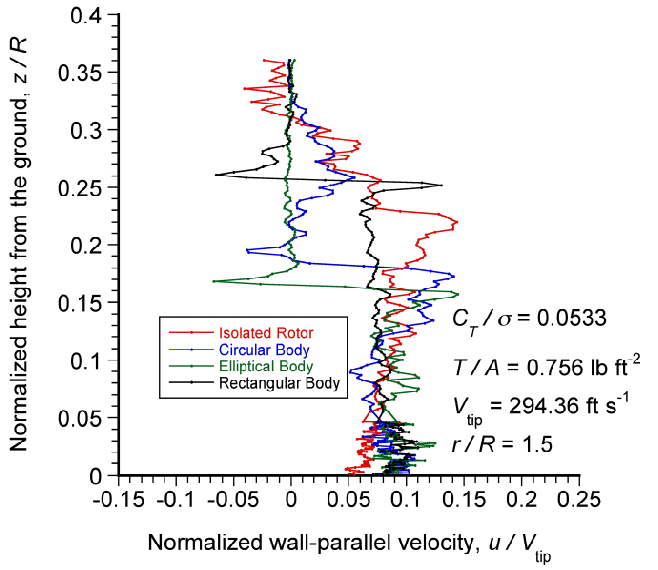

(f) $r/R = 1.5$

Figure 3.25: Instantaneous measurements of the wall-parallel flow for the isolated rotor and below the nose of each body at several downstream distances: (a) $r/R = 1.0$; (b) $r/R = 1.1$; (c) $r/R = 1.2$; (d) $r/R = 1.3$; (e) $r/R = 1.4$; (f) $r/R = 1.5$; (g) $r/R = 1.6$.

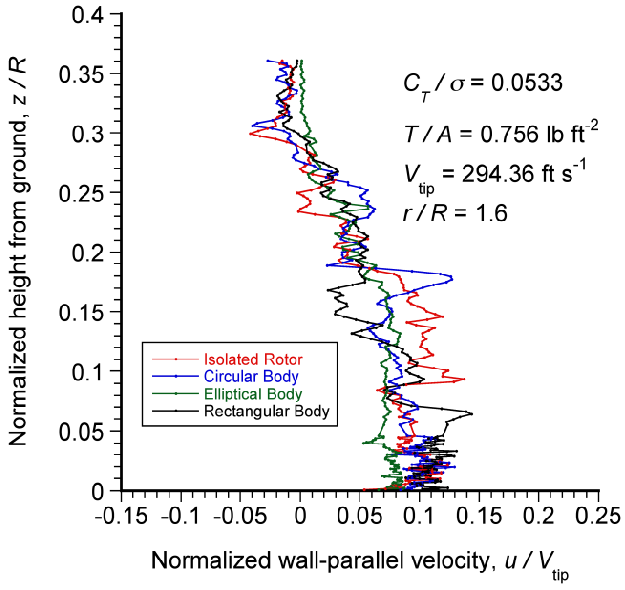

(g) $r/R = 1.6$

Figure 3.25: Instantaneous measurements of the wall-parallel flow for the isolated rotor and below the nose of each body at several downstream distances: (a) $r/R = 1.0$; (b) $r/R = 1.1$; (c) $r/R = 1.2$; (d) $r/R = 1.3$; (e) $r/R = 1.4$; (f) $r/R = 1.5$; (g) $r/R = 1.6$.

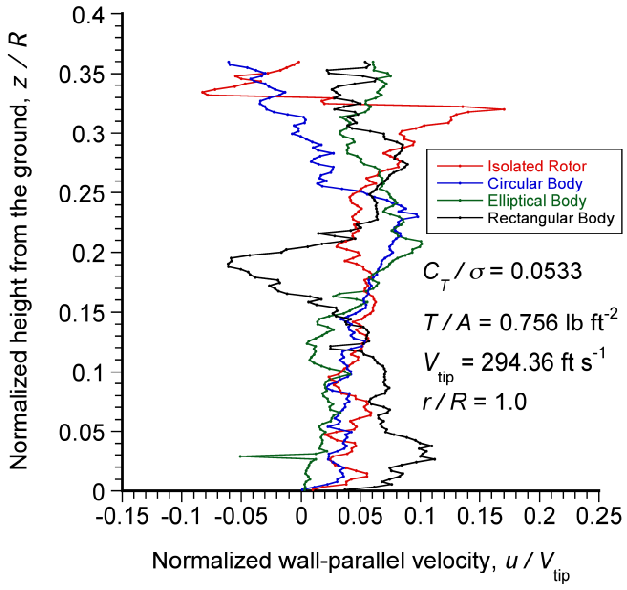

(a) $r/R = 1.0$

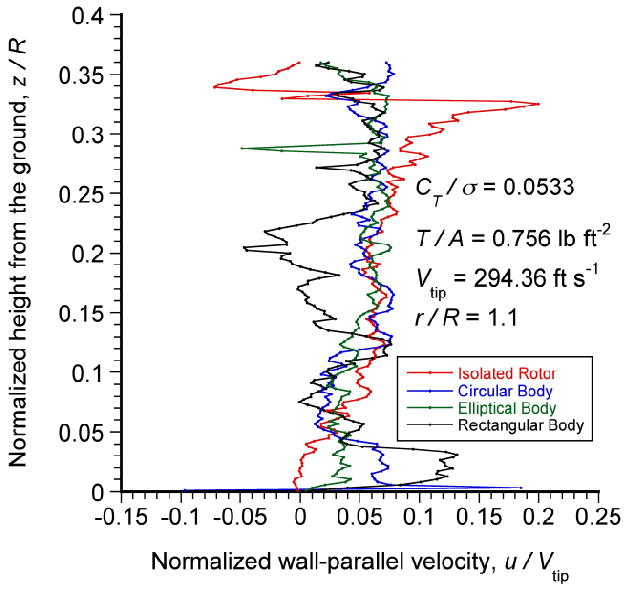

(b) $r/R = 1.1$

Figure 3.26: Instantaneous measurements of the wall-parallel flow for the isolated rotor and below the tail of each body at several downstream distances: (a) $r/R = 1.0$; (b) $r/R = 1.1$; (c) $r/R = 1.2$; (d) $r/R = 1.3$; (e) $r/R = 1.4$; (f) $r/R = 1.5$; (g) $r/R = 1.6$.

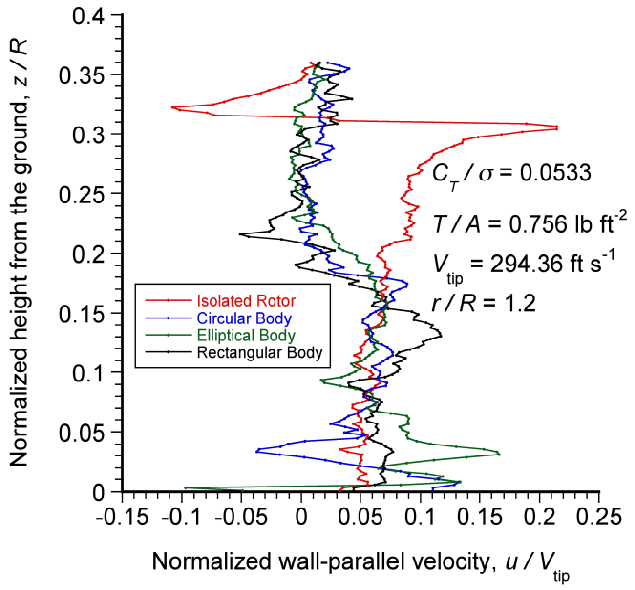

(c) $r/R = 1.2$

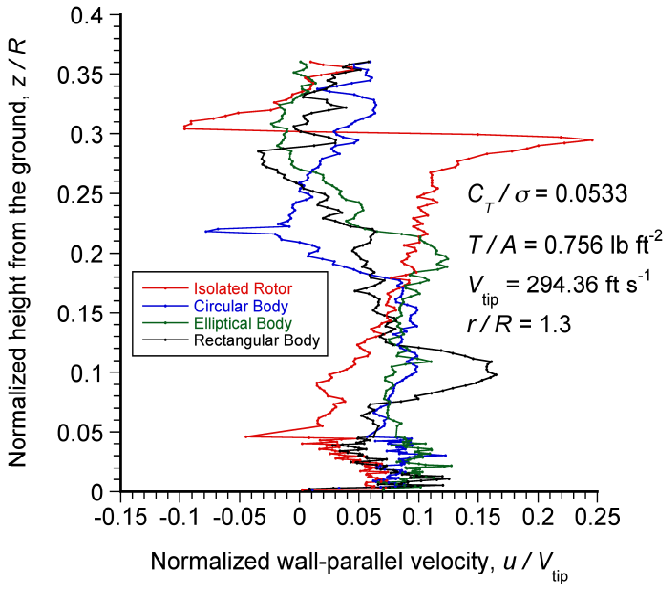

(d) $r/R = 1.3$

Figure 3.26: Instantaneous measurements of the wall-parallel flow for the isolated rotor and below the tail of each body at several downstream distances: (a) $r/R = 1.0$; (b) $r/R = 1.1$; (c) $r/R = 1.2$; (d) $r/R = 1.3$; (e) $r/R = 1.4$; (f) $r/R = 1.5$; (g) $r/R = 1.6$.

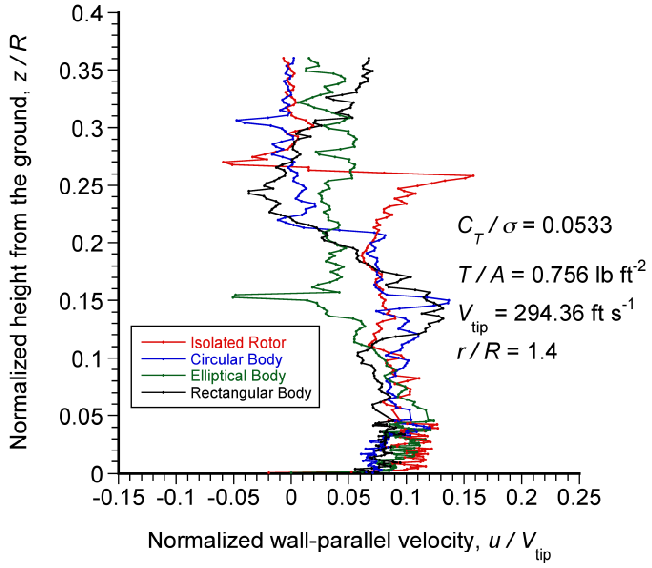

(e) $r/R = 1.4$

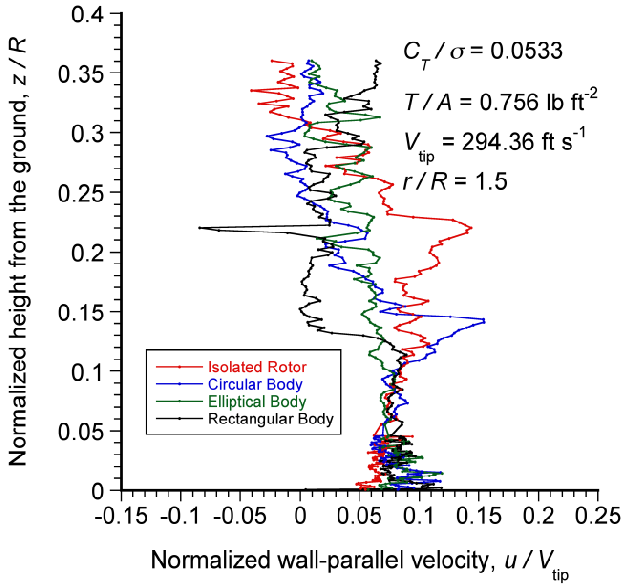

(f) $r/R = 1.5$

Figure 3.26: Instantaneous measurements of the wall-parallel flow for the isolated rotor and below the tail of each body at several downstream distances: (a) $r/R = 1.0$; (b) $r/R = 1.1$; (c) $r/R = 1.2$; (d) $r/R = 1.3$; (e) $r/R = 1.4$; (f) $r/R = 1.5$; (g) $r/R = 1.6$.

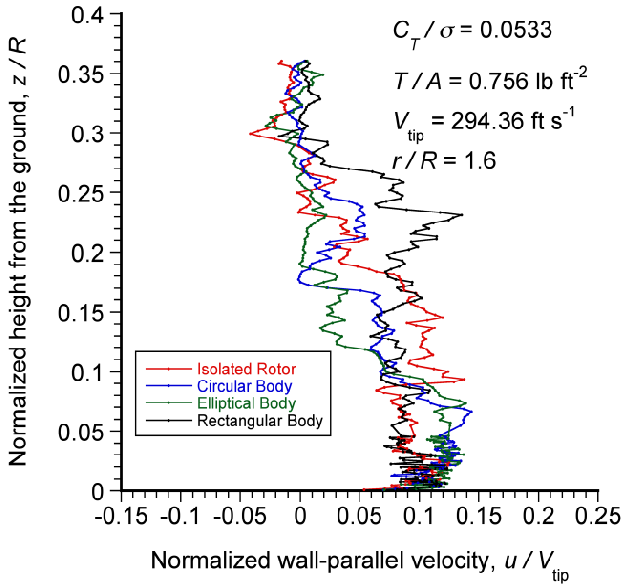

(g) $r/R = 1.6$

Figure 3.26: Instantaneous measurements of the wall-parallel flow for the isolated rotor and below the tail of each body at several downstream distances: (a) $r/R = 1.0$; (b) $r/R = 1.1$; (c) $r/R = 1.2$; (d) $r/R = 1.3$; (e) $r/R = 1.4$; (f) $r/R = 1.5$; (g) $r/R = 1.6$.

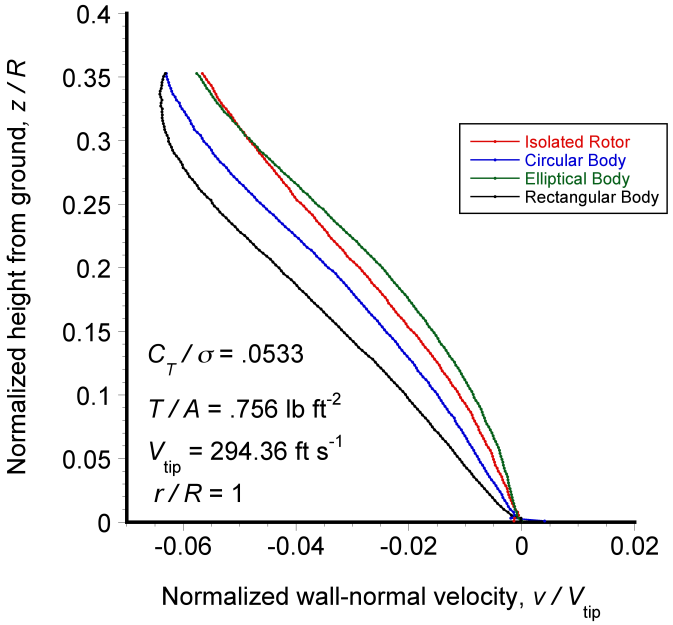

(a) $r/R = 1.0$

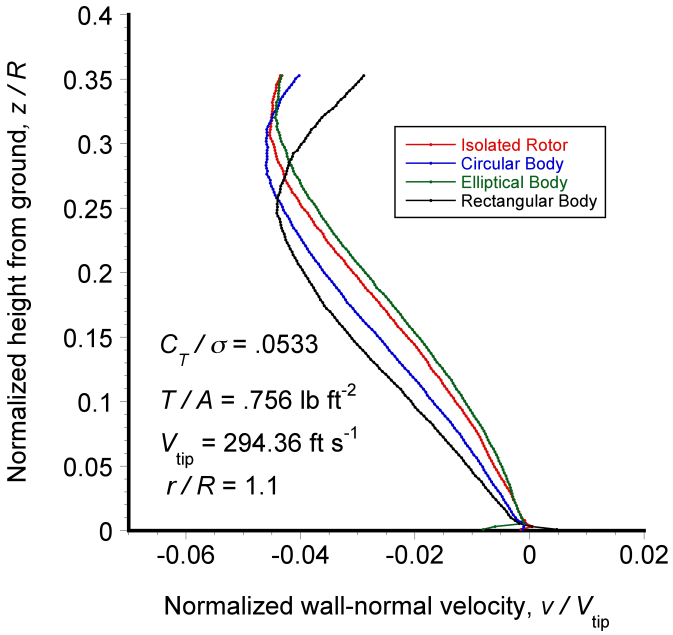

(b) $r/R = 1.1$

Figure 3.27: Time-averaged measurements of the wall-normal flow for the isolated rotor and below the nose of each body at several downstream distances: (a) $r/R = 1.0$; (b) $r/R = 1.1$; (c) $r/R = 1.2$; (d) $r/R = 1.3$; (e) $r/R = 1.4$; (f) $r/R = 1.5$; (g) $r/R = 1.6$.

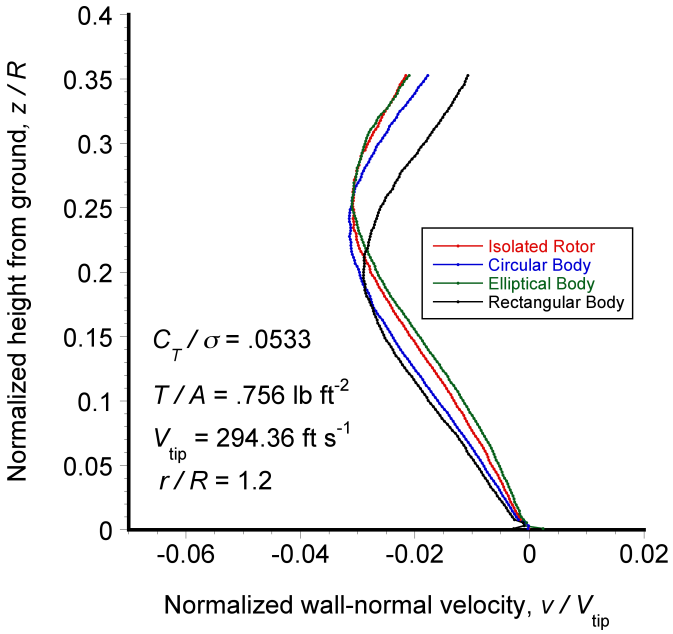

(c) $r/R = 1.2$

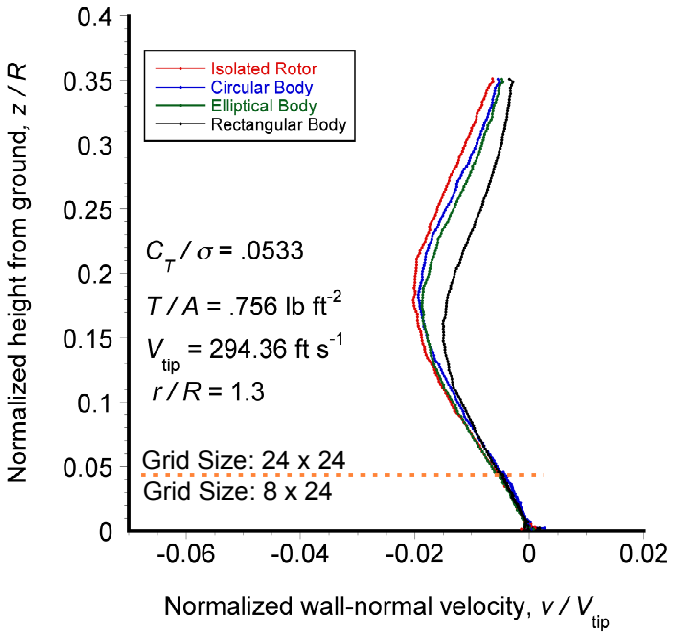

(d) $r/R = 1.3$

Figure 3.27: Time-averaged measurements of the wall-normal flow for the isolated rotor and below the nose of each body at several downstream distances: (a) $r/R = 1.0$; (b) $r/R = 1.1$; (c) $r/R = 1.2$; (d) $r/R = 1.3$; (e) $r/R = 1.4$; (f) $r/R = 1.5$; (g) $r/R = 1.6$.

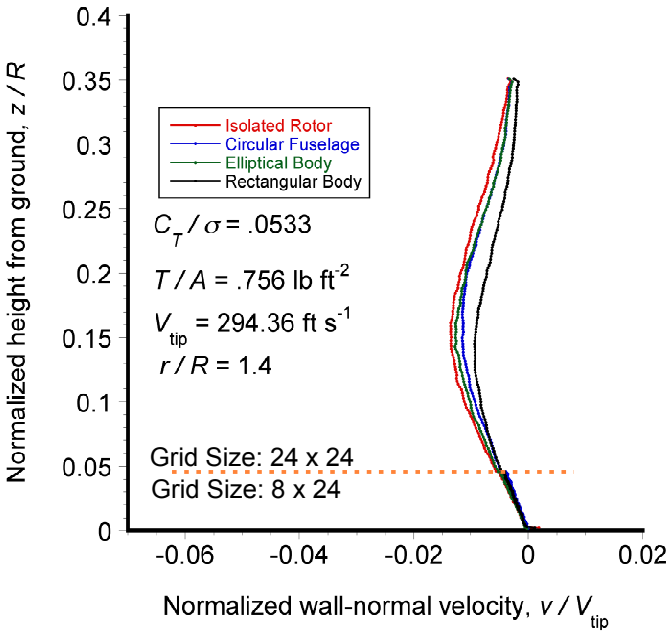

(e) $r/R = 1.4$

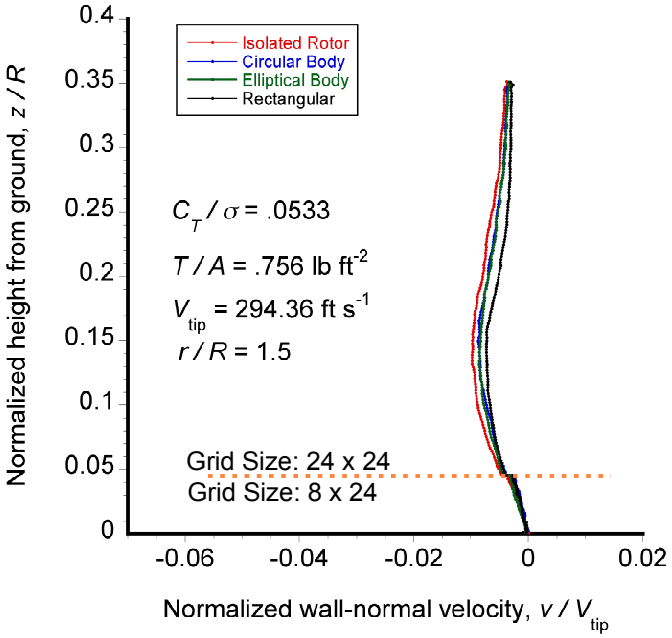

(f) $r/R = 1.5$

Figure 3.27: Time-averaged measurements of the wall-normal flow for the isolated rotor and below the nose of each body at several downstream distances: (a) $r/R = 1.0$; (b) $r/R = 1.1$; (c) $r/R = 1.2$; (d) $r/R = 1.3$; (e) $r/R = 1.4$; (f) $r/R = 1.5$; (g) $r/R = 1.6$.

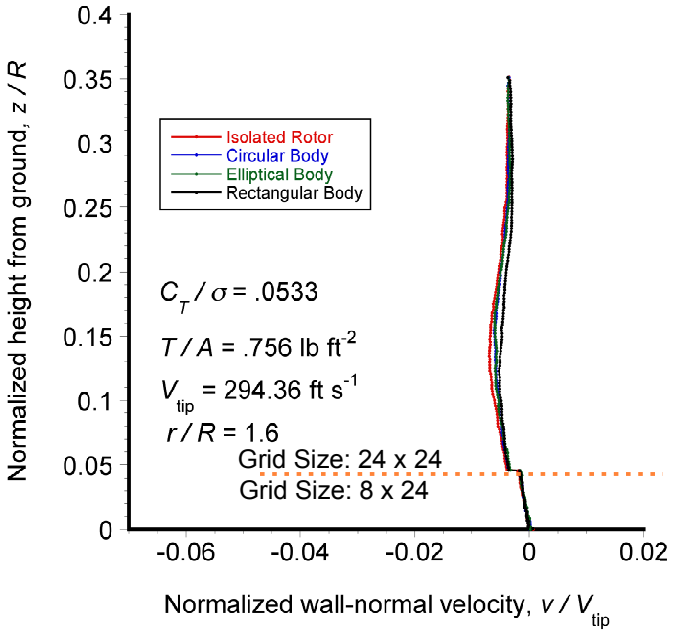

(g) $r/R = 1.6$

Figure 3.27: Time-averaged measurements of the wall-normal flow for the isolated rotor and below the nose of each body at several downstream distances: (a) $r/R = 1.0$; (b) $r/R = 1.1$; (c) $r/R = 1.2$; (d) $r/R = 1.3$; (e) $r/R = 1.4$; (f) $r/R = 1.5$; (g) $r/R = 1.6$.

produces a different profile with smaller velocity magnitudes. Interestingly, the body with the rectangular cross-section produces slightly positive velocities at various points. While the profiles become much more similar at greater downstream distances, some differences still remain, suggesting that the effects of the body shapes are longer lasting beyond the tail section.

Figure 3.30 shows the Reynolds shear stress, $-\rho\overline{u'v'}$, at at the ground plane at several radial locations downstream from the nose of the bodies. In these results, the Reynolds stress has been normalized by the tip velocity squared, i.e., by $-\overline{u'v'}/V_{\text{tip}}^2$. Previous work [70–72] has shown that the Reynolds stresses are primary contributors to the stresses acting on a sediment bed and, therefore, they have a primary effect on particle mobilization and uplift. Figure 3.30 shows a schematic of a classical wall jet with the typical Reynolds stress profile. It is important to note that in Fig. 3.30, Reynolds stress is given as $\overline{u'v'}/V_{\text{tip}}^2$ and as such the values are of opposite sign to those shown in the current experiments, meaning that the profile will be "mirrored" about its vertical axis. However, the general shape of the profile is still very similar.

The highest shear stresses occurred in the shear layer that forms along the slipstream boundary, where the high-speed flow inside the wake interacts with the low-speed flow outside the wake. Performing a simple ensemble average of the flow measurements tends to smooth the effects of coherent vortical structures, causing the averages to resemble a more classical turbulent jet flow [68, 69]. However, the average shear stress in the shear layer is still greater because of the remnants of the tip vortices [72]. It can be seen that in all the radial cuts, the bodies with the circular and elliptical cross-sectional shapes produced similar levels of Reynolds stress. These bodies showed Reynolds stress profiles

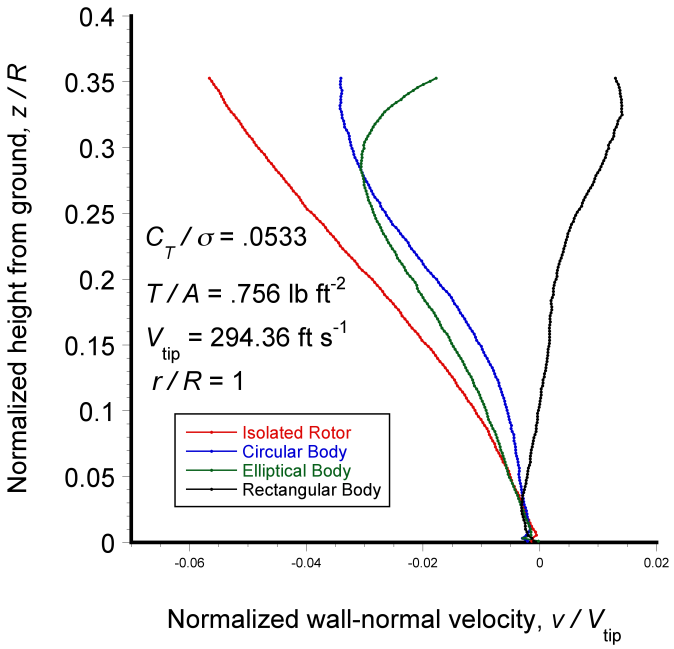

(a) $r/R = 1.0$

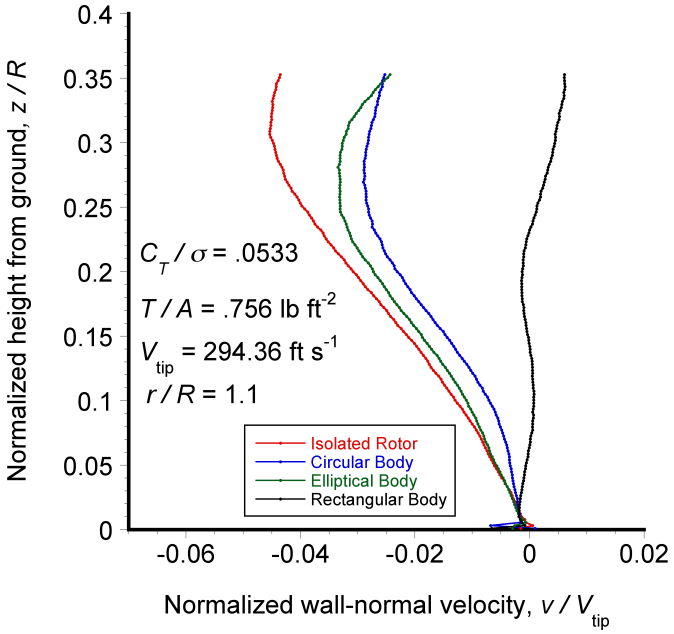

(b) $r/R = 1.1$

Figure 3.28: Time-averaged measurements of the wall-normal flow for the isolated rotor and below the tail of each body at several downstream distances: (a) $r/R = 1.0$; (b) $r/R = 1.1$; (c) $r/R = 1.2$; (d) $r/R = 1.3$; (e) $r/R = 1.4$; (f) $r/R = 1.5$; (g) $r/R = 1.6$.

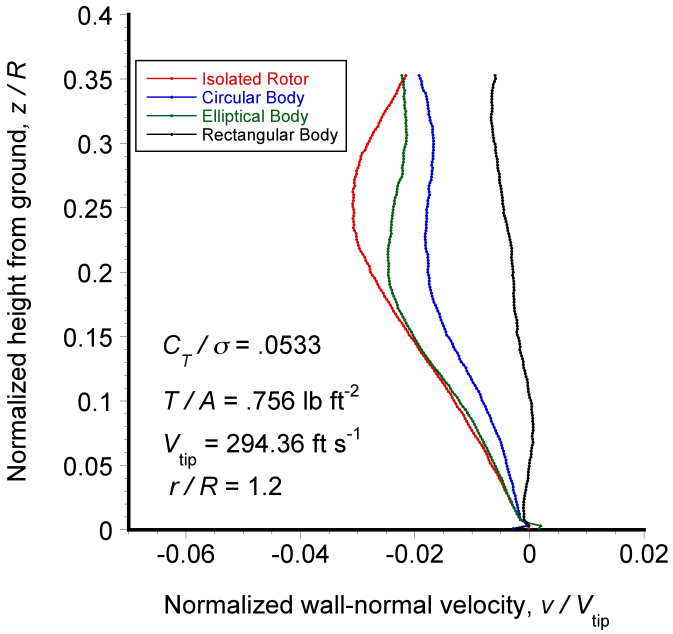

(c) $r/R = 1.2$

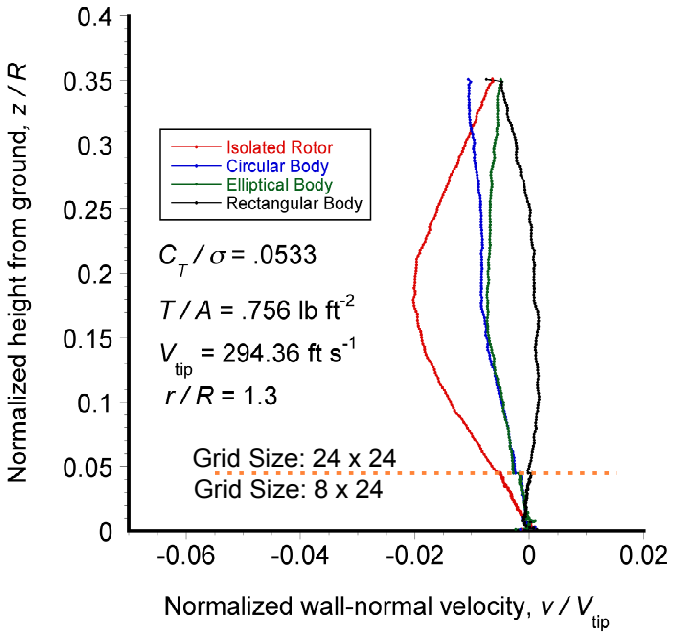

(d) $r/R = 1.3$

Figure 3.28: Time-averaged measurements of the wall-normal flow for the isolated rotor and below the tail of each body at several downstream distances: (a) $r/R = 1.0$; (b) $r/R = 1.1$; (c) $r/R = 1.2$; (d) $r/R = 1.3$; (e) $r/R = 1.4$; (f) $r/R = 1.5$; (g) $r/R = 1.6$.

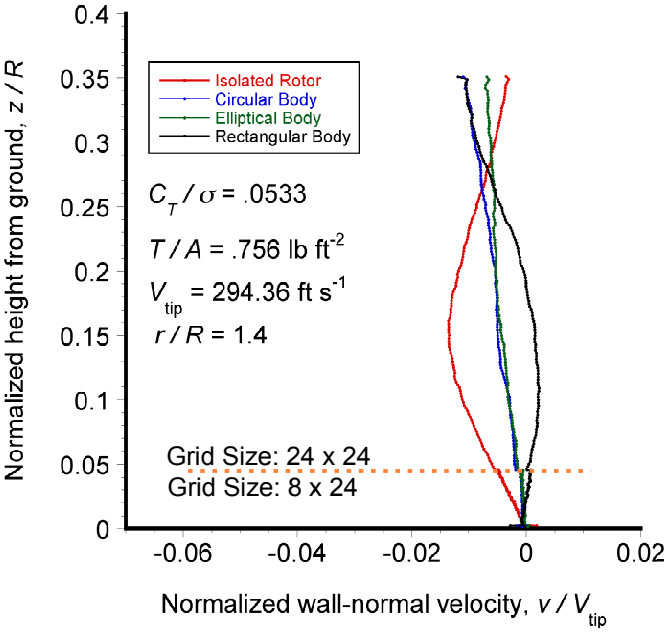

(e) $r/R = 1.4$

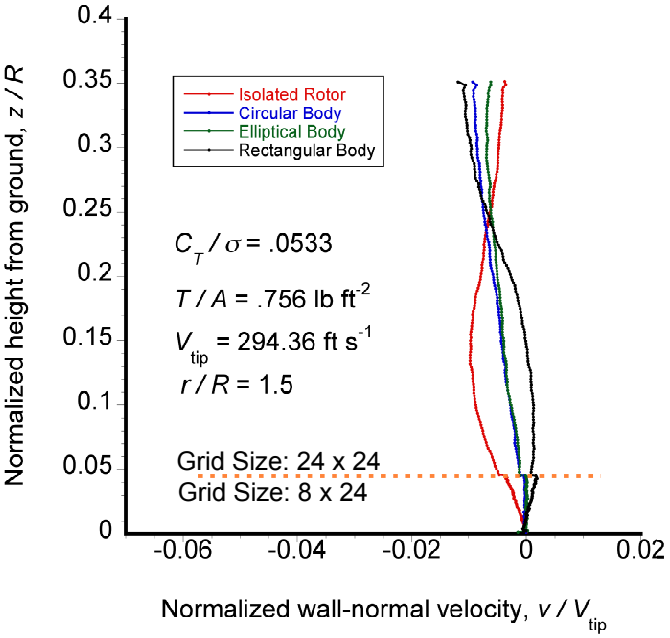

(f) $r/R = 1.5$

Figure 3.28: Time-averaged measurements of the wall-normal flow for the isolated rotor and below the tail of each body at several downstream distances: (a) $r/R = 1.0$; (b) $r/R = 1.1$; (c) $r/R = 1.2$; (d) $r/R = 1.3$; (e) $r/R = 1.4$; (f) $r/R = 1.5$; (g) $r/R = 1.6$.

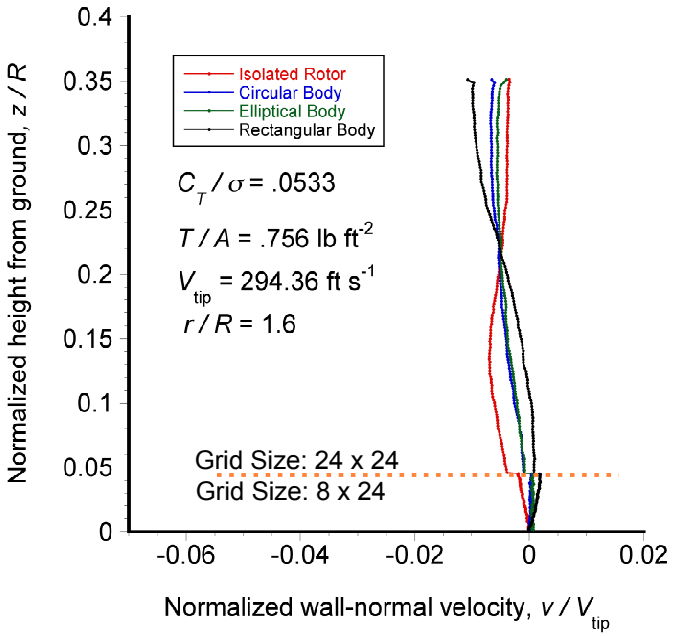

(g) $r/R = 1.6$

Figure 3.28: Time-averaged measurements of the wall-normal flow for the isolated rotor and below the tail of each body at several downstream distances: (a) $r/R = 1.0$; (b) $r/R = 1.1$; (c) $r/R = 1.2$; (d) $r/R = 1.3$; (e) $r/R = 1.4$; (f) $r/R = 1.5$; (g) $r/R = 1.6$.

that are similar to those obtained with the isolated rotor, although some differences did appear at the most inboard radial locations. However, the body with the rectangular cross-section produced noticeably different Reynolds stresses at locations inboard of $1.3R$. The difference was particularly significant at $1.0R$ and $1.1R$ where the flow was still turning and the wall jet flow had not yet fully developed. This difference is likely a result of the wake distortion by the body with the rectangular cross-section that was mentioned earlier.

Notice that the differences in Reynolds stress profiles were limited to inboard radial locations. Beginning at $r/R = 1.4$, all the Reynolds stress profiles began to converge toward a more classical wall jet profile. At $1.6R$, all body shapes produced similar values of Reynolds stress. The trends shown suggest that at downstream distances greater than about $r/R = 1.6$ the different body shapes may indeed produce similar effects near the ground in terms of sediment mobilization and uplift.

In Fig. 3.31, the normalized shear stress is shown for several radial locations below the tail of each body. At the more inboard radial locations, it can be seen that the flow velocities below the bodies produce very different values of shear stress than was obtained with the isolated rotor. In particular, the levels of shear stress in the shear layer that were obtained with the bodies with the circular and elliptical cross-sections are noticeably lower than for the other cases. There is generally a large variation in the Reynolds stresses between the isolated rotor and each body at locations inboard of $r/R = 1.3$. These differences are likely a result of the disruption of the slipstream boundary and the turbulent wake of the bodies. As the flow moves radially outward, it can be seen that the Reynolds stress profiles begin to take on the features of classical turbulent jet flow. However, this effect occurs at a slower rate than for the flow at beyond the nose of the bodies;

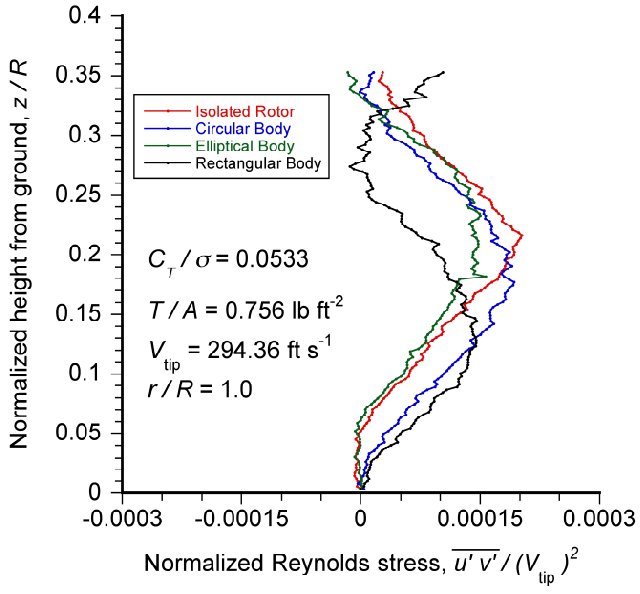

(a) $r/R = 1.0$

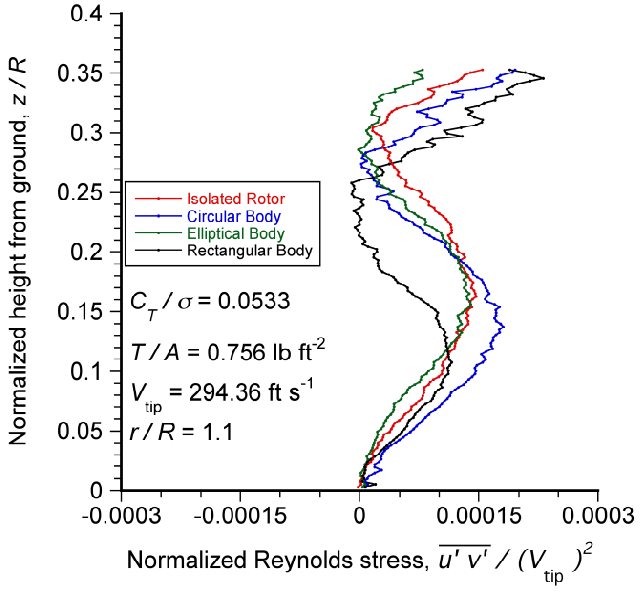

(b) $r/R = 1.1$

Figure 3.29: Measurements of normalized Reynolds stress for the isolated rotor and below the nose of each body at several downstream distances: (a) $r/R = 1.0$; (b) $r/R = 1.1$; (c) $r/R = 1.2$; (d) $r/R = 1.3$; (e) $r/R = 1.4$; (f) $r/R = 1.5$; (g) $r/R = 1.6$.

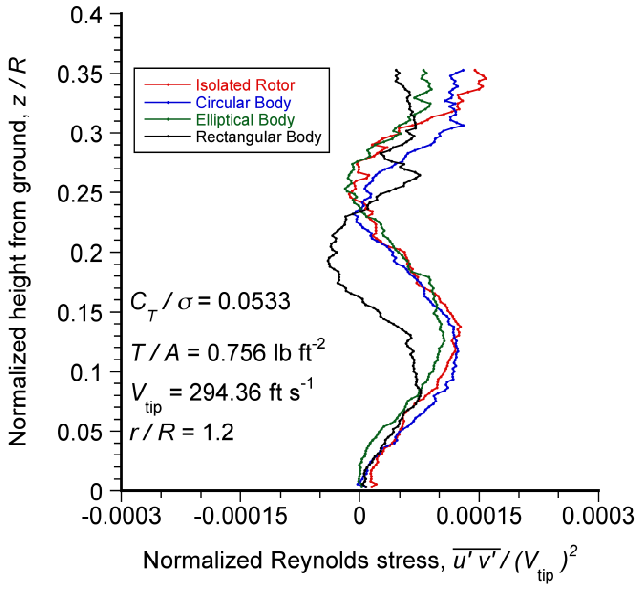

(c) $r/R = 1.2$

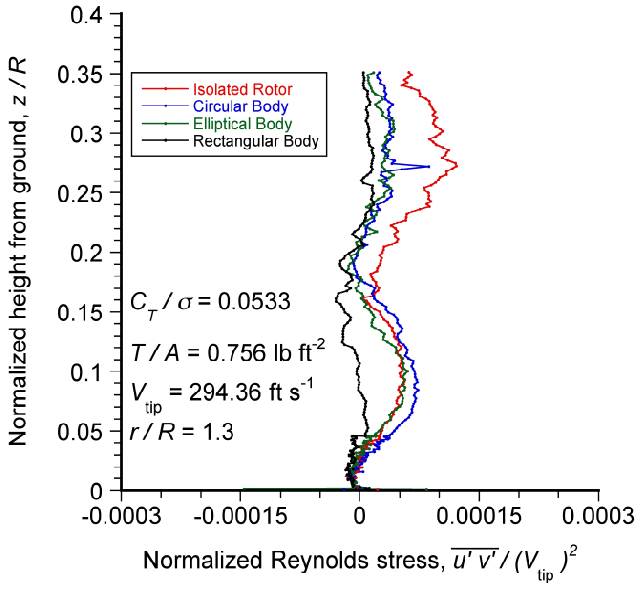

(d) $r/R = 1.3$

Figure 3.29: Measurements of normalized Reynolds stress for the isolated rotor and below the nose of each body at several downstream distances: (a) $r/R = 1.0$; (b) $r/R = 1.1$; (c) $r/R = 1.2$; (d) $r/R = 1.3$; (e) $r/R = 1.4$; (f) $r/R = 1.5$; (g) $r/R = 1.6$.

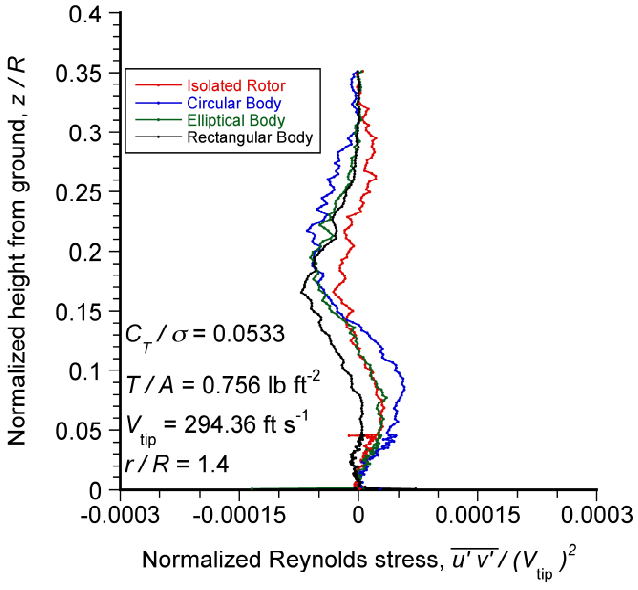

(e) $r/R = 1.4$

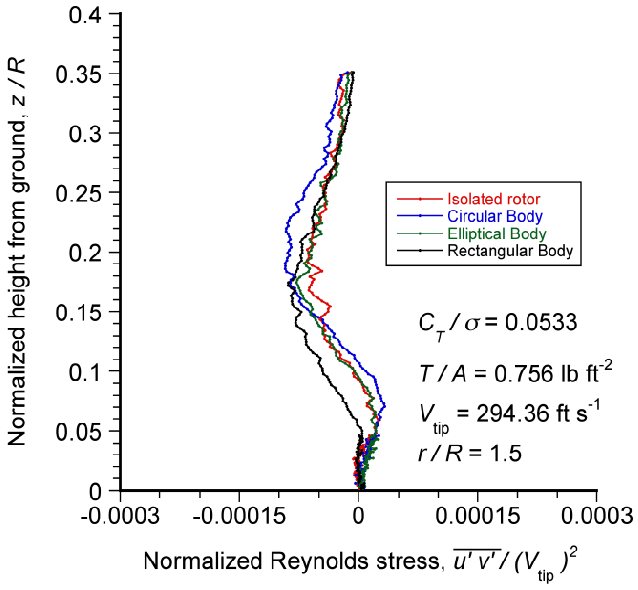

(f) $r/R = 1.5$

Figure 3.29: Measurements of normalized Reynolds stress for the isolated rotor and below the nose of each body at several downstream distances: (a) $r/R = 1.0$; (b) $r/R = 1.1$; (c) $r/R = 1.2$; (d) $r/R = 1.3$; (e) $r/R = 1.4$; (f) $r/R = 1.5$; (g) $r/R = 1.6$.

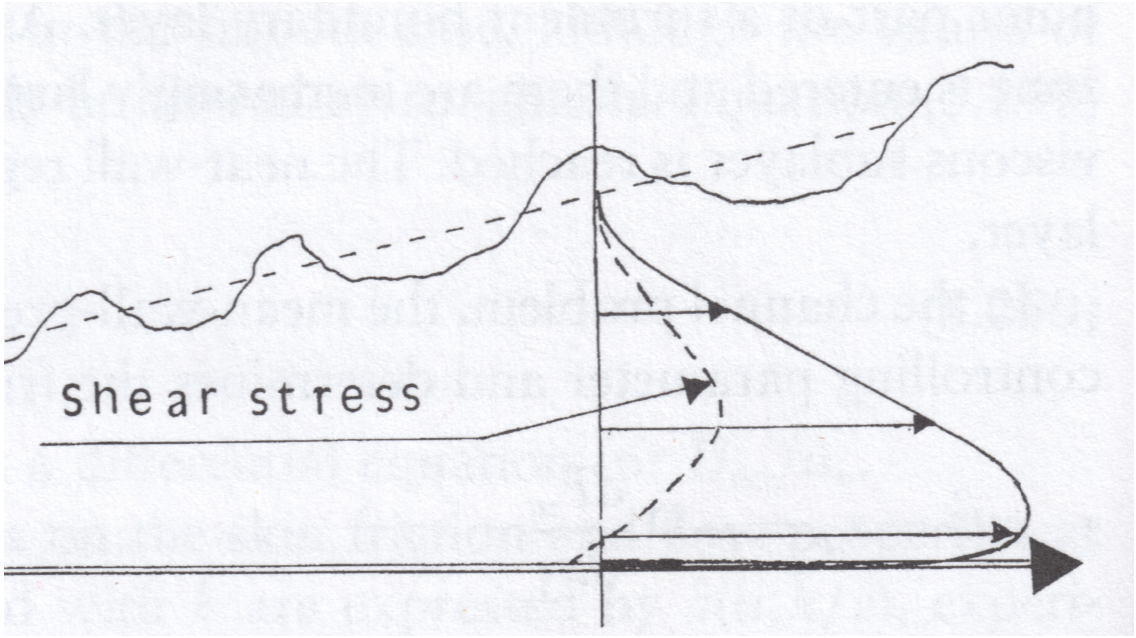

Figure 3.30: Schematic of representative flow velocities and Reynolds stresses of a classical wall jet [69].

see Fig 3.30.

At r/R = 1.6, the Reynolds stresses in the flow on the ground with each of the bodies differ from those obtained with the isolated rotor. Most notably, the body with the rectangular cross-section produced significantly higher levels of Reynolds stress compared to those produced by the isolated rotor or the other bodies. The fact that at r/R = 1.6, the Reynolds stress profiles for the various cases showed significant differences from each other suggests that the effects of the tail of the body may be experienced to larger downstream distances. Ultimately, these outcomes may affect sediment mobilization and uplift at larger downstream distances away from the rotor.

It is interesting to notice at radial positions on the ground further downstream from the rotor the velocity profile resembles a classical wall jet profile, including the formation

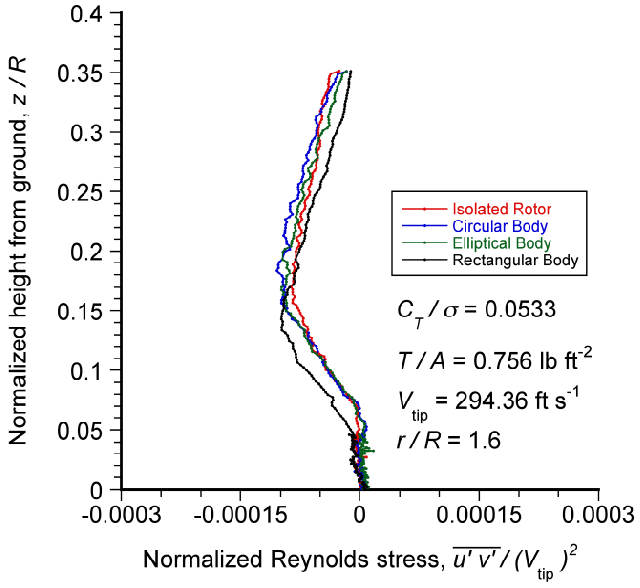

(g) $r/R = 1.6$

Figure 3.30: Measurements of normalized Reynolds stress for the isolated rotor and below the nose of each body at several downstream distances: (a) $r/R = 1.0$; (b) $r/R = 1.1$; (c) $r/R = 1.2$; (d) $r/R = 1.3$; (e) $r/R = 1.4$; (f) $r/R = 1.5$; (g) $r/R = 1.6$.

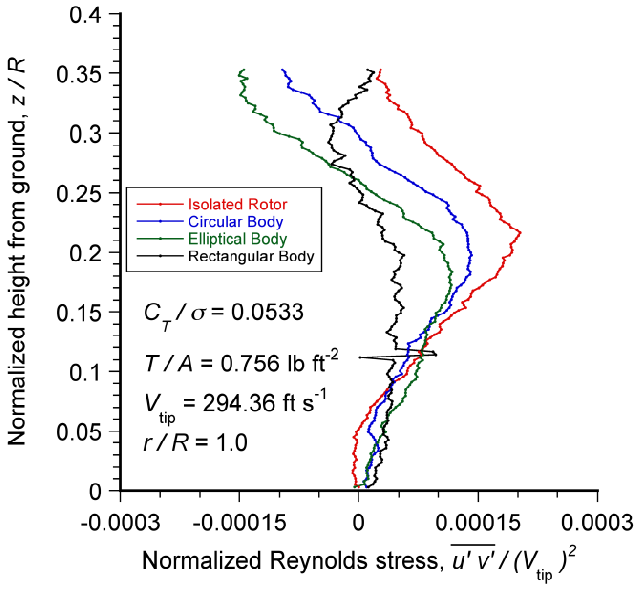

(a) $r/R = 1.0$

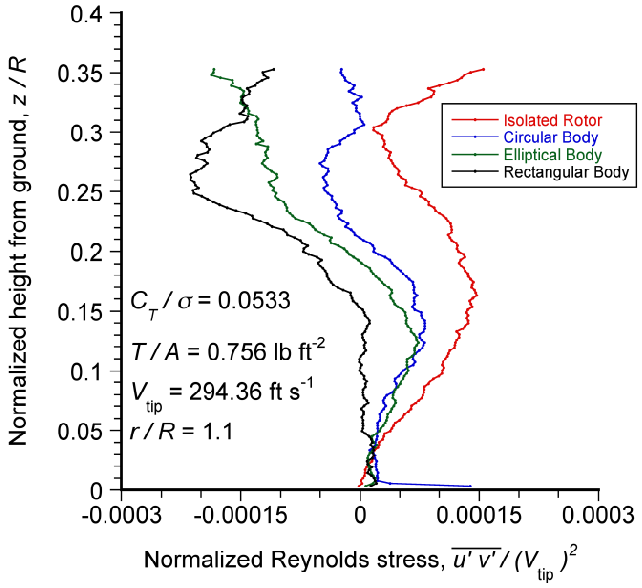

(b) $r/R = 1.1$

Figure 3.31: Measurements of normalized Reynolds stress for the isolated rotor and below the tail of each body at several downstream distances: (a) $r/R = 1.0$; (b) $r/R = 1.1$; (c) $r/R = 1.2$; (d) $r/R = 1.3$; (e) $r/R = 1.4$; (f) $r/R = 1.5$; (g) $r/R = 1.6$.

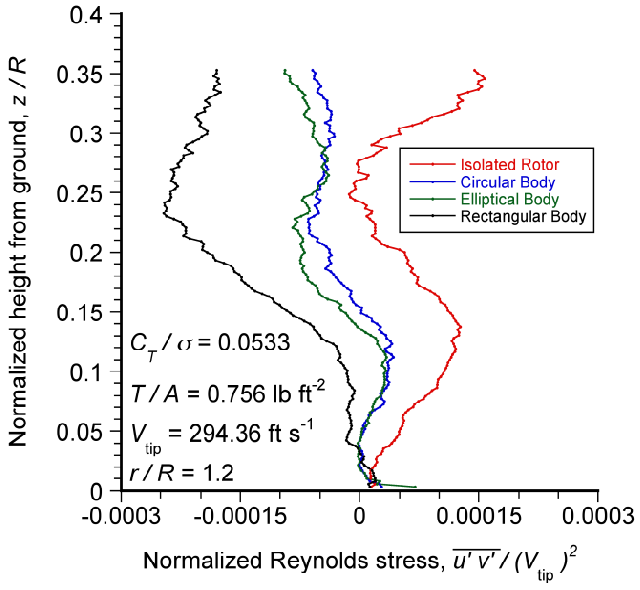

(c) $r/R = 1.2$

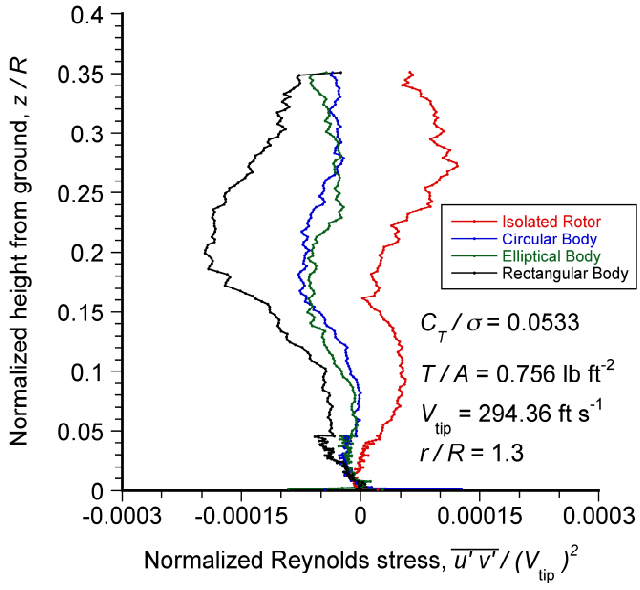

(d) $r/R = 1.3$

Figure 3.31: Measurements of normalized Reynolds stress for the isolated rotor and below the tail of each body at several downstream distances: (a) $r/R = 1.0$; (b) $r/R = 1.1$; (c) $r/R = 1.2$; (d) $r/R = 1.3$; (e) $r/R = 1.4$; (f) $r/R = 1.5$; (g) $r/R = 1.6$.

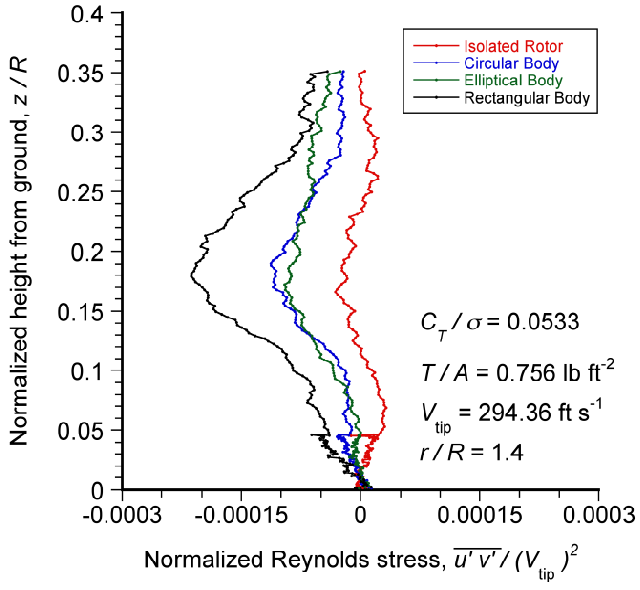

(e) $r/R = 1.4$

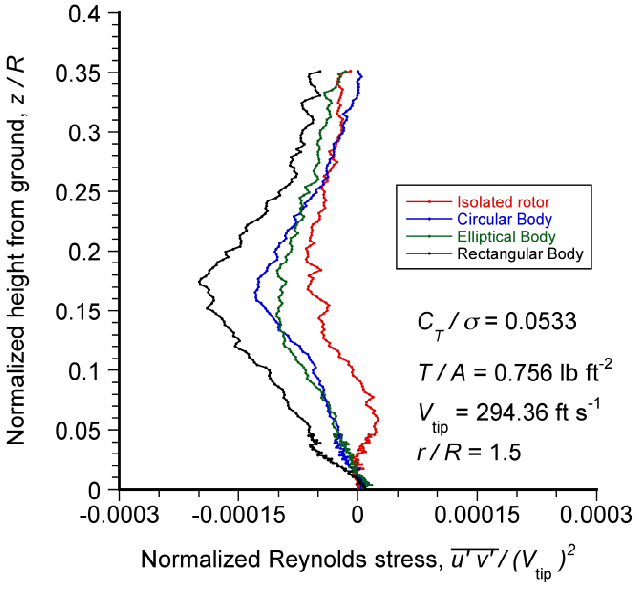

(f) $r/R = 1.5$

Figure 3.31: Measurements of normalized Reynolds stress for the isolated rotor and below the tail of each body at several downstream distances: (a) $r/R = 1.0$; (b) $r/R = 1.1$; (c) $r/R = 1.2$; (d) $r/R = 1.3$; (e) $r/R = 1.4$; (f) $r/R = 1.5$; (g) $r/R = 1.6$.

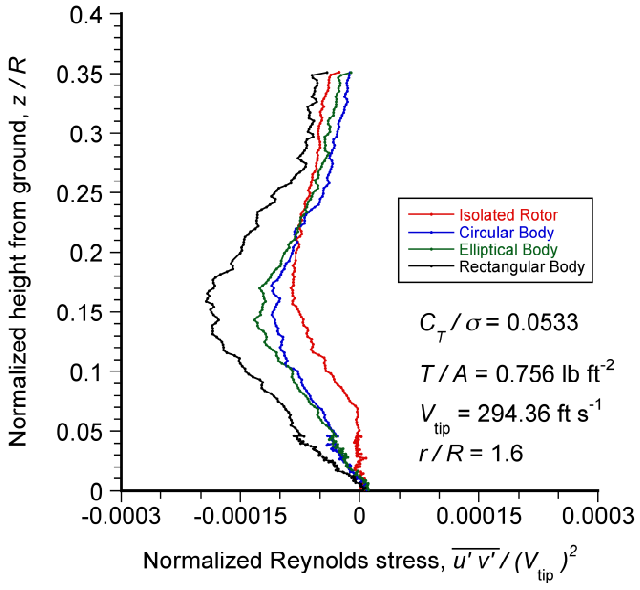

(g) $r/R = 1.6$

Figure 3.31: Measurements of normalized Reynolds stress for the isolated rotor and below the tail of each body at several downstream distances: (a) $r/R = 1.0$; (b) $r/R = 1.1$; (c) $r/R = 1.2$; (d) $r/R = 1.3$; (e) $r/R = 1.4$; (f) $r/R = 1.5$; (g) $r/R = 1.6$.

of a viscous sublayer [68]. The measurements made closest to the ground in the present experiments were determined to be in the viscous sublayer, shown by the schematic in Fig. 3.32.

To verify that the measurement point was in the viscous sublayer, the velocity profiles were converted into wall units [68] using the equations

$$z^+ = \frac{z u_\star}{\nu} \tag{3.5}$$

and

$$u^+ = \frac{u}{u_\star} \tag{3.6}$$

as shown in Fig. 3.33, where z is the height from the ground, ν is the kinematic viscosity, and $u_\star$ is the friction velocity.

Using the PIV measurements in the near-wall region, it was possible to estimate the friction velocity, $u_\star$, from the shear stress, τ_w, using

$$u_\star = \sqrt{\frac{\tau_w}{\rho}} \tag{3.7}$$

where

$$\tau_w = \mu \left(\frac{\partial u}{\partial z} \right)_{z \to 0} \tag{3.8}$$

and where $\left(\frac{\partial u}{\partial z} \right)_{z \to 0}$ is calculated using the closest reliable measurements to the ground plane. Using the assumption that the velocity gradient in the viscous sublayer is linear, an extrapolation to the no-slip condition at $z/R = 0$ was made.

Figure 3.34 shows the friction velocities on the ground plane at several radial locations for the isolated rotor and beyond the nose of each of the three body shapes. It can be seen that in all cases, the friction velocities at a given downstream distance are

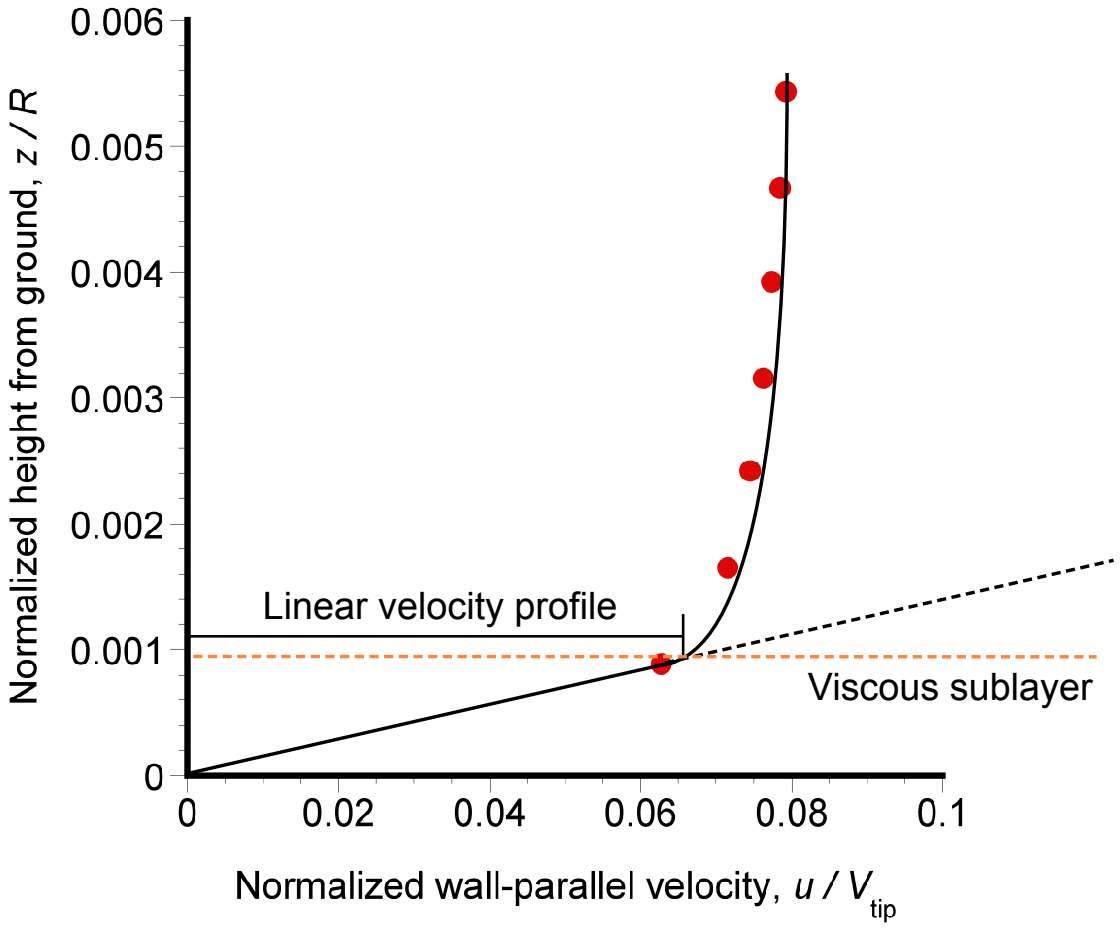

Figure 3.32: Schematic showing a velocity profile and velocity gradient at the ground.

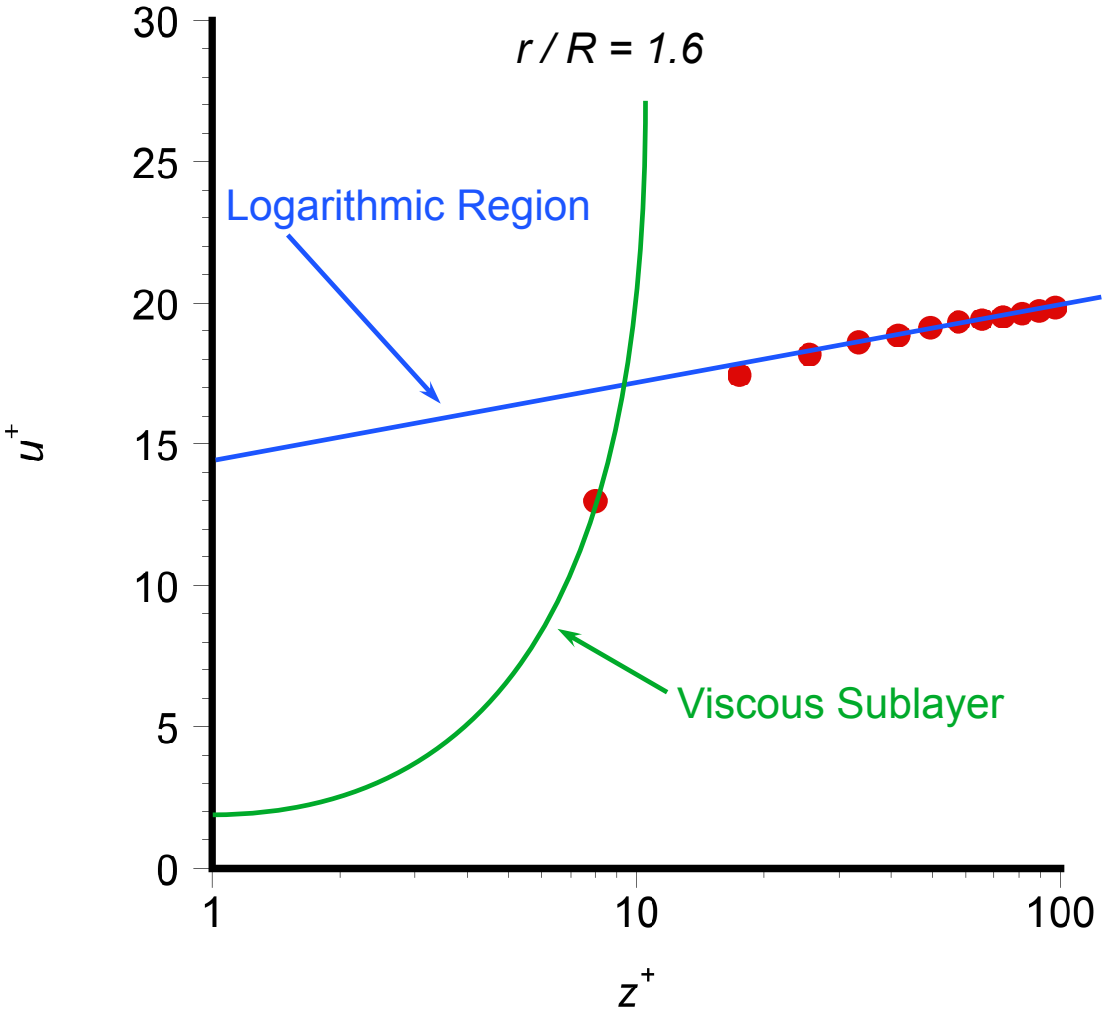

Figure 3.33: Close to the wall, showing the measurements taken in the viscous sublayer.

approximately equal. Similar results can be seen in Fig. 3.35, which shows the friction velocities on the ground plane at several downstream locations to the rear of each body. The results seem to indicate that, once the flow has developed more into a wall jet, body shape had little subsequent effects on the friction velocities and, therefore, will also have similar effects on the mobilization of sediment.

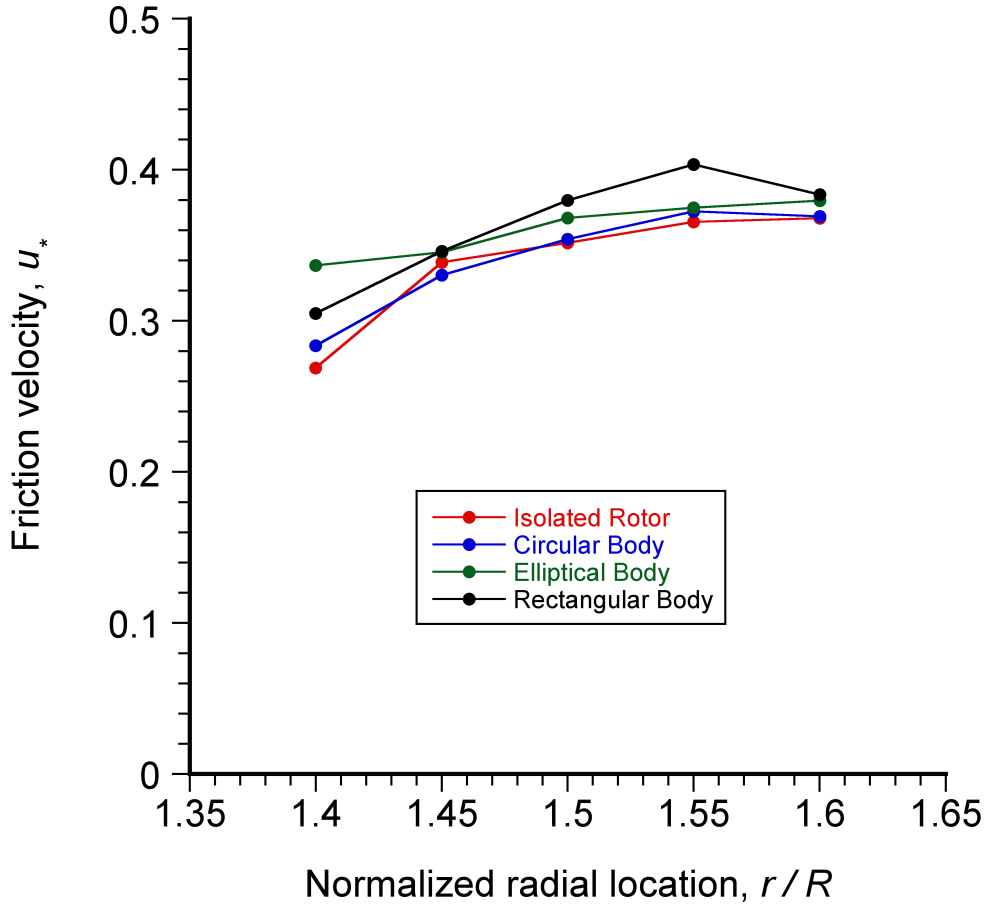

Figure 3.34: Friction velocities close to the ground of the isolated rotor and below the nose of each body at several downstream locations.

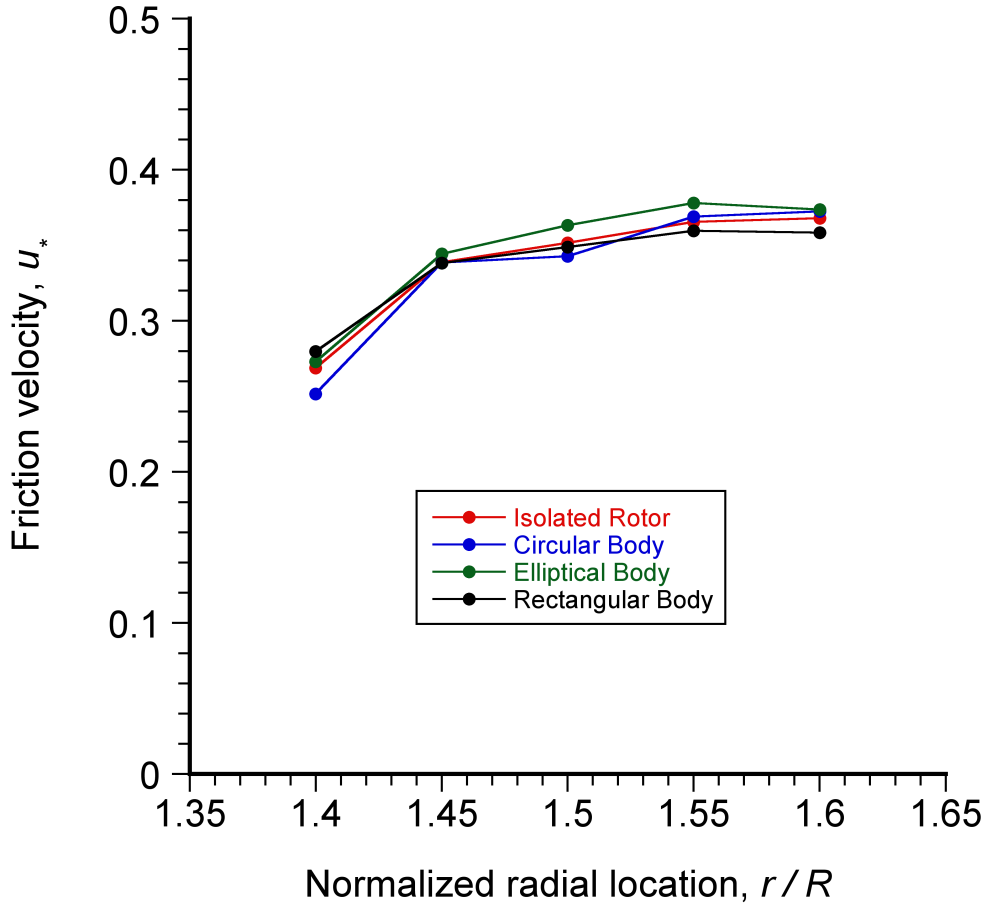

Figure 3.35: Friction velocities close to the ground of the isolated rotor and below the tail of each body at several downstream locations.

Chapter 4

Conclusions

4.1 Summary

In the present research, flow visualization and particle image velocimetry experiments were conducted on a two-bladed rotor operating over a ground plane to understand how the presence of a body beneath the rotor would affect the development of the vortical wake, as well as the flow over the ground. Bodies of three different cross-sectional shapes were used, namely circular, elliptical, and rectangular, respectively. Detailed flow measurements were made in radial planes in the rotor wake and along the longitudinal axis of each body at both its nose and its tail.

The spatial locations of the tip vortices were tracked as a function of wake age as they convected in the flow, with measurements being made of both the instantaneous (phase-resolved) and time-averaged velocity fields. Detailed wall-parallel velocity and Reynolds stress profiles were obtained at various distances along the ground plane to help understand how the body shape affected the flow there.

The longer term goals of the work were to better understand how the presence of a body (representing the airframe of a helicopter) would affect the flow at the ground, and hence influence the problem of rotorcraft brownout. To this end, future experiments with the rotor and the different body shapes could be performed in the presence of sediment (i.e., two-phase flow measurements could be done with dust particles). It is recognized,

however, that this latter goal is clearly a much more ambitious one.

The following conclusions have been drawn from the present research:

1. Performance measurements made with each body under the rotor were found to be very similar to those obtained from the isolated rotor. Comparable power polars were measured in each case, suggesting that for the configuration studied the effect of the body shape on the flow at the rotor was relatively small. However, some increase of induced power factor was noted. Furthermore, the relationship between blade collective pitch and blade loading coefficient was only minimally affected by changes in body shape. Nevertheless, the effects obtained were significant enough so that the collective blade pitch needed to be adjusted to keep the rotor thrust constant with the different body configurations.

2. The vertical force on the three bodies under the action of the rotor flow showed differences for a given rotor thrust. At lower blade loading coefficients all three bodies produced a downforce. The bodies with the circular and elliptical cross-sections, which had similar cross-sections, both showed evidence of the Fradenburgh thrust recovery effect at higher blade loading coefficients. The body with the rectangular cross-section exhibited different trends in vertical force over the same range of blade loading coefficients but showed no evidence of a thrust recovery effect. The results obtained suggest that the cross-section of the body will most likely affect the development of the wake below the body in ground effect operation, and so the Fradenburgh thrust recovery effect may not always be obtained.

3. The development of the rotor wake around the nose (i.e., the short end) of each

body was found to be similar in each case to the wake that was produced by the isolated rotor. However, the locations of the tip vortices obtained with the body with the rectangular cross-section were located noticeably more inboard with a lower overall radial expansion of the wake boundary. The different trajectories in this case occurred because the flow remained attached to the nose of the body with the rectangular cross-section to greater downstream distances compared to the other two bodies. However, at older wake ages and downstream distances, the locations of the tip vortices were found to be similar in all cases.

4. The tail of each body (i.e., the long end) severely disrupted the development of the rotor wake, and the locations of the tip vortices here differed considerably from those that were produced by the isolated rotor. In this case, the blade tip vortices impinged upon the rear of the body surface just below the rotor, followed by stretching and bursting as it wrapped around the body contour. The bursting of the vortices led to rapid diffusion of the vorticity and the creation of new turbulence. Consequently, the flow below the tail of the body was dominated by smaller-scale turbulence from the disrupted rotor wake combined with the turbulent body wake itself, with little in the way of coherent vortical structures being seen at this location in the flow.

5. Below the nose of each body, the maximum instantaneous excursions from the average wall-parallel velocity profiles were caused by the presence of the tip vortices. The peak in these excursions was found to be similar for all body shapes although the phase angle (wake age) at which they occurred was different. The excursions in the velocity field close to the ground is known to be important in regard to the

magnitude of the shear stress that is produced at the wall and, ultimately, the mobilization of any loose sediment by the boundary layer flow.

6. On the ground below the nose of each body (i.e., the short end), the flow quickly developed in a manner that resembled the development of a classical wall jet type of flow. In this regard, the flows over the ground plane in each case showed very similar wall-parallel and wall-normal velocities, Reynolds stresses, and friction velocities at further downstream distances from the rotor. This observation suggests that the nose shape of the body (at least with the ones measured in the present work) may not have much effect on the mobilization and uplift of dust as it affects the rotorcraft brownout problem.

7. The flow on the ground below the tail of each body (i.e., the long end), including wall-parallel and wall normal velocities, and Reynolds stresses, did not develop to resemble that of a classical wall jet and varied noticeably from those produced by the isolated rotor. In this case, the catastrophic disruption of the rotor wake by the presence of each body caused lasting effects on the flow that could be observed further downstream along the ground plane. In particular, the body with the rectangular cross-section shaped produced significantly higher Reynolds stress in the wall region than was shown for the other bodies or for the isolated rotor. In this case, it is likely that the resulting boundary layer flow over the ground would most likely have some effect on the mobilization and uplift of dust, if it were to be distributed there.

4.2 Suggestions for Future Work

The present study of the flow generated by a rotor operating above a body and a ground plane has yielded a greater understanding of the aerodynamic environment that might be produced by a helicopter when it was operating in-ground-effect. The path of the tip vortices as they convected in the rotor wake was determined using flow visualization and PIV, and the effects of three body shapes on the wake distortion was measured. The details of the boundary layer flow as it developed along the ground plane was also measured. However, there is clearly further research that could be pursued to expand upon the results obtained the present work and to provide more measurements that could further the understanding of the rotor in ground effect problem and, eventually, to obtain a better understanding of the brownout problem.

The measurement resolution of the PIV system used in the present research was limited by the sheer number of separate experiments that were required, by the available equipment and instrumentation, and by the volume of data that could be practically stored. In the current work, a camera with a 4 Mega-pixel resolution was used. A camera with higher resolution could better resolve the details of turbulent flow around the bodies and the flow in the cores of the vortices, with the recognition that the volume of data would commensurately increase. Data management (i.e., collection, storage and processing) is clearly an issue for these types of measurements. But the main advantage of using a camera with a higher resolution camera is that a larger region of interest could be imaged without loss of spatial resolution. The number of image pairs would be reduced, decreasing the required time for data collection and processing. While the problem of

data storage limitations can never actually be "solved," increases in drive storage space as technology progresses will raise the ceiling on the quantity of data that can be successfully stored and manipulated.

In the current work, measurements were taken at temporal increments of only 30°, which could obviously be made finer to obtain higher temporal fidelity. Such measurements would allow for a more thorough investigation of the tip vortices and turbulent structures at various stages of their development of the rotor wake. In addition, a contiguous time-history of the flow could be established using time-resolved flow visualization and PIV with a high speed laser and camera. At the cost of resolution, time-resolved methods could be used to examine the temporal evolution of the wake and track individual flow structures and eddies as they were convected in the rotor and body wake toward the ground plane. Of particular interest in would be the temporal evolution of the blade time vortices as they impinge upon the tail of a body and burst. While the present work has given a qualitative overview of the process, it does not give quantitative analysis of the actual vortex characteristics. Understanding of blade tip vortices at the nose of the body could also be expanded by examining the temporal evolution of core growth, peak swirl velocity, and circulation that occurs while the vortices interact with the body.

The rotor wake is clearly a very complex, unsteady, three-dimensional, vortically dominated flow. Further PIV experiments can be performed to better quantify aspects of the three-dimensionality, particularly in the vicinity of each of the body shapes. To better understand the overall flow field, the flow field could also be dissected into several radial cuts made at different azimuth angles around the ground plane and PIV performed. While the current experiments investigated only a single radial plane along the longitudinal axis

of the body, changes in the flow can be expected everywhere to some extent. These further experiments would be particularly useful for investigating the three-dimensional effects of a body shape in the wake of the rotor.

Further measurements could be made using three-component PIV. To this end, two cameras are required with this technique to be able to simultaneously measure all three velocity components. Such an approach would allow for the measurement of azimuthal velocities at each radial plane, and would help to quantify the three-dimensional (and perhaps aperiodic) aspects of the wake. In particular, three-component PIV could be used to more accurately resolve the turbulence characteristics in the flow. As shown in the current experiments, a body placed below the rotor significantly increases the turbulence of the flow at the ground. Turbulence is inherently three-dimensional, and is known to be an important factor in sediment mobilization. Therefore, to properly understand brownout it is necessary first to understand the nature of the turbulence at the ground.

The inflow distribution at the rotor is known to affect rotor performance as well as the wake flow and the flow at the ground. Testing rotors with different blade shapes—and hence inflow distributions—would help to increase the understanding of how the effect of a body shape on the wake is altered by changing the rotor. In particular, blade twist is known to create a more linear inflow distribution. Performing additional experiments with blades of various twist would help to quantify the evolution of the wake with a body under the rotor as inflow changes. This work would be useful as it would expand the knowledge of another parameter that may affect sediment mobilization and, therefore, the problem of brownout.

Obviously, there are many other body shapes that could be examined, as well as

more complex shapes that are more representative of actual helicopter fuselages. In particular, nose and tail shapes more representative of realistic fuselages found on actual helicopters (or rotorcraft, in general) should be examined. Examination of several different cockpit shapes, and comparison of their effects on the flow below the rotor, could yield important information on the flow at the ground and how that flow may, in turn, affect the mobilization and uplift of dust in the pilot's primary field of view.

Other investigations could be done on bodies that incorporate a long, narrow tail boom and perhaps also a tail rotor, although the latter is clearly a more ambitious goal. Several different tail structures (e.g., H-tail, fenestron, traditional tail rotor) could be investigated, as required. Ultimately, a comparison of the effects produced by a series of different body types could help to determine the effect of different candidate airframe designs on the rotor wake structure and, potentially, the potential for the mobilization of dust from a brownout perspective. At this point, based on the results of this thesis, it seems unlikely that airframe design would be a primary consideration in the minimization of brownout severity.

All bodies used in the present experiment were similar in size, i.e., they had the same lengths and similar aspect ratios. However, to further investigate the effect of body size on the rotor wake, several bodies of different size could be investigated. Body length, width, and height (i.e., to study the effect of fuselage aspect ratio) could each be varied separately to determine their effect on the rotor wake and the resulting flow at the ground plane. For each body, rotor performance and body force measurements should be taken, which will help to assess whether particular bodies may have adverse effects on rotor performance.

In the current work, measurements at a single height of one rotor radius from the ground plane were made because it was a representative operational condition for a helicopter; sustained hovering flight, especially during landing and takeoff, occurs at or about this rotor height off the ground. It is known, however, that the structure and development of the rotor wake depends critically on the height of the rotor above the ground. Therefore, additional experiments will be required to assess the effects of body shape on the rotor wake at different heights off the ground. Performance measurements should be taken at several heights above a ground plane, ranging from out-of-ground-effect conditions (i.e., with the rotor in free air) to a simulated "landing" situation. To better understand the flow effects produced by a body, time-resolved and phase-resolved flow measurements should be made at each height over a range of wake ages to quantify how the structure and development of the rotor wake is changed as the rotor is brought closer to the ground.

While further experiments can give much information about the development of the rotor wake as it interacts with a body in the vicinity of a ground plane, understanding the consequences on the development of brownout will required that future tests also be conducted in the presence of sediment. To this end, two-phase flow measurements using particle tracking velocimetry should be used in conjunction with PIV to simultaneously track the motion of both the air and the sediment particles that are mobilized by the flow field. While it is recognized that this is a much more ambitious goal, the quantification of particle density fields in the two-phase flow will help in the understanding of particle transport and sediment concentration in areas below the rotor where it would affect the pilot's visibility of the ground.

Chapter A

Q-criterion Algorithm

The Q-criterion is defined in Ref. [62] as the discriminant of the velocity gradient tensor as given by

$$Q = \frac{1}{4}S^2 - q \tag{A.1}$$

where S and q are the trace and determinate of the velocity gradient tensor, respectively. S and q are given by

$$S = \frac{\partial u}{\partial x} + \frac{\partial v}{\partial x} \tag{A.2}$$

and

$$q = \frac{\partial u}{\partial x}\frac{\partial v}{\partial y} - \frac{\partial u}{\partial y}\frac{\partial v}{\partial x} \tag{A.3}$$

The velocity gradients were calculated using Richardson extrapolation using the equation

$$\left(\frac{\partial f}{\partial x_i}\right) \approx \frac{f_{i-2} - 8f_{i-1} + 8f_{i+1} - f_{i+2}}{12\Delta X} \tag{A.4}$$

The accuracy of the Richardson extrapolation was $O(\Delta X^3)$, and the uncertainty was $\approx 0.95\varepsilon/\Delta X$.

The Q-criterion algorithm was applied to each instantaneous PIV image to identify vortex centers in each image. Vortex centers were identified using local maximum values of Q. The resulting vortex center locations were manually matched with the corresponding wake age. A mathematical mean of the vortex center locations was found for each wake age.

Bibliography

[1] Knight, M., and Hefner, R. A., "Analysis of Ground Effect on the Lifting Airscrew," NACA TN 835, 1941.

[2] Cheeseman, I. C., and Bennett, W. E., "The Effect of the Ground on a Helicopter Rotor in Forward Flight," ARC R & M 3021, 1955.

[3] Hayden, J. S., "The Effect of the Ground on Helicopter Hovering Power Required," American Helicopter Society 32th Annual National V/STOL Forum Proceedings, Washington DC, May 10–12, 1976.

[4] Fradenburgh, E. A., "The Helicopter and the Ground Effect Machine," *Journal of the American Helicopter Society*, Vol. 5, (4), 1960, pp. 26–28.

[5] Zbrozek, J., "Ground Effect on the Lifting Rotor," British ARC R & M 2347, 1947.

[6] Prouty, R. W., "Ground Effect and the Helicopter," AIAA Paper 85-4034, AIAA/AHS/ASEE Aircraft Design Systems and Operations Meeting, Colorado Springs, CO, October 14–16, 1985.

[7] Fradenburgh, E. A., "Aerodynamic Factors Influencing Overall Hover Performance," AGARD-CP-111, 1972.

[8] Curtiss, H. C., Erdman, W., and Sun, M., "Ground Effect Aerodynamics," *Vertica*, Vol. 11, (1/2), 1987, pp. 29–42.

[9] Light, J. S., and Norman, T., "Tip Vortex Geometry of a Hovering Helicopter Rotor in Ground Effect," American Helicopter Society 45th Annual Forum Proceedings, Boston, MA, May 22–24, 1989.

[10] Lee, T. E., Leishman, J. G., and Ramasamy, M., "Fluid Dynamics of Interacting Blade Tip Vortices With a Ground Plane," *Journal of the American Helicopter Society*, Vol. 55, 022005, 2010.

[11] Milluzzo, J., Sydney, A., Rauleder, J., and Leishman, J. G., "In-Ground-Effect Aerodynamics of Rotors with Different Blade Tips," 66th Annual Forum Proceedings of the American Helicopter Society, Phoenix, AZ, May 10–13, 2010.

[12] Ramasamy, M., Johnson, B., Huismann, T., and Leishman, J. G., "Digital Particle Image Velocimetry Measurements of Tip Vortex Characteristics Using an Improved Aperiodicity Correction," *Journal of the American Helicopter Society*, Vol. 54, 012004, 2009, pp. 1–13.

[13] Nathan, N. D., and Green R. B., "Measurements of a Rotor Flow in Ground Effect and Visualisation of the Brownout Phenomenon," American Helicopter Society 64th Annual Forum Proceedings, Montréal, Canada, April 29–May 1, 2008.

[14] Curtiss, H. C., Sun, M., Putman, W. F., and Hanker, E. J., "Rotor Aerodynamics in Ground Effect at Low Advance Ratios," *Journal of the American Helicopter Society*, Vol. 29, (1), 1984, pp. 48–55.

[15] Johnson, B., Leishman, J. G., and Sydney, A., "Investigation of Sediment Entrainment in Brownout Using High-Speed Particle Image Velocimetry," American Helicopter Society 65th Annual Forum Proceedings, Grapevine, TX, May 27–29, 2009.

[16] Sydney, A., Baharani, A., and Leishman, J. G., "Understanding Brownout Using Near-Wall High-Speed Dual-Phase Flow Measurements," American Helicopter Society 67th Annual Forum Proceedings, Virginia Beach, VA, May 3–5, 2011.

[17] Ramasamy, M., and Leishman, J. G., "Interdependence of Diffusion and Straining of Helicopter Blade Tip Vortices," *Journal of Aircraft*, Vol. 41, (5), September 2004, pp. 1014–1024.

[18] Ananthan, S., Leishman, J. G., and Ramasamy, M., "The Role of Filament Stretching in the Free-Vortex Modeling of Rotor Wakes," American Helicopter Society 58th Annual National Forum, Montréal, Canada, June 11–13, 2002.

[19] McAlister, K. W., "Measurements in the Near Wake of a Hovering Rotor," Proceedings of the 27th AIAA Fluid Dynamic Conference, New Orleans, June 18–20, 1996.

[20] Boisard, R., and Baeder, J. D., "Impact of Three-Dimensional and Compressible Effects of Blade Loading on BVI Noise Signature," American Helicopter Society 57th Annual National Forum, Washington D.C, May 9–11, 2001.

[21] Berry, J., and Bettschart, N., "Rotor-Fuselage Interaction: Analysis and Validation with Experiment," American Helicopter Society 53rd Annual National Forum, Virginia Beach, VA, April 29–May 1, 1997.

[22] Bagai, A., and Leishman, J. G., "A Study of Rotor Wake Development and Wake/Body Interactions in Hover," *Journal of the American Helicopter Society*, Vol. 37, October 1992, pp. 48–57.

[23] Crouse, G. L., Leishman, J. G., and Bi, N., "Theoretical and Experimental Study of Unsteady Rotor/Body Aerodynamic Interactions," *Journal of the American Helicopter Society*, Vol. 37, No. 1, January 1992, pp. 55–65.

[24] Drees, J. M., and Hendal, W. P., "The Field of Flow Through a Helicopter Rotor Obtained from Wind Tunnel Smoke Tests," *Journal of Aircraft Engineering*, Vol. 23, (266), February 1950, pp. 107–111.

[25] Landgrebe, A. J., "An Analytical Method for Predicting Rotor Wake Geometry," Presented at the AIAA/AHS VTOL Research, Design & Operations Meeting, Atlanta, GA, February 17–19, 1969.

[26] Cook, C. V., "The Structure of the Rotor Blade Tip Vortex," Paper 3, Aerodynamics of Rotary Wings, AGARD CP-111, September 13–15, 1972.

[27] Tung, C., Pucci, S. L., Caradonna, F. X., and Morse, H. A., "The Structure of Trailing Vortices Generated by Model Helicopter Rotor Blades," NASA TM 81316, 1981.

[28] Egolf, T. A., and Landgrebe, A. J., "Helicopter Rotor Wake Geometry and its Influence in Forward Flight, Vol. 1 – Generalized Wake Geometry and Wake Effects in Rotor Airloads and Performance," NASA CR-3726, October 1983.

[29] Johnson, W., "Wake Model for Helicopter Rotors in High Speed Flight," NASA CR-1177507, USAVSCOM TR-88-A-008, November 1988.

[30] Leishman, J. G., and Bi, N., "Measurements of a Rotor Flowfield and the Effects on a Body in Forward Flight," *Vertica*, Vol. 14, (3), 1990, pp. 401–415.

[31] Lorber, P. F., Stauter, R. C., Pollack, M. J., and Landgrebe, A. J., "A Comprehensive Hover Test of the Airloads and Airflow of an Extensively Instrumented Model Helicopter Rotor," Vol. 1–5, USAAVSCOM TR-D-16 (A-E), October 1991.

[32] Bagai, A., Moedersheim, E., and Leishman, J. G., "Developments in the Visualization of Rotor Wakes using the Wide-Field Shadowgraph Method," *Journal of Flow Visualization & Image Processing*, Vol. 1, (3), July–September 1993, pp. 211–233.

[33] Bhagwat, M. J., and Leishman, J. G., "Stability Analysis of Helicopter Rotor Wakes in Axial Flight," *Journal of the American Helicopter Society*, Vol. 45, (3), July 2000, pp. 165–178.

[34] Ringler, T. D., George, A. R., and Steele, J. B., "The Study of Blade-Vortex Interaction Sound Generation and Directionality," Proceedings of the AHS Technical Specialists Meeting, Philadelphia, PA, October 15–17, 1991.

[35] Leishman, J. G., "Aeroacoustics of 2-D and 3-D Blade Vortex Interaction Using the Indicial Method," American Helicopter Society 52nd Annual Forum, Washington, DC, June 4–6, 1996.

[36] Lim, J., and Tung, C., "2GCHAS Predictions of HART Blade-Vortex Interaction Loading," Proceedings of the AHS Technical Specialists, Meeting for Rotorcraft Acoustics and Aerodynamics, Williamsburg, VA, October 28–30, 1997.

[37] Bagai, A., and Leishman, J. G., "Flow Visualization of Compressible Vortex Structures Using Density Gradient Techniques," *Experiments in Fluids*, Vol. 15, No. 6, October 1993, pp. 431–442.

[38] Caradonna, F., Hendley, E., Silva, M., Huang, S., Komerath, N., Reddy, U., Mahalingam, R., Funk, R., Wong, O., Ames, R., Darden, L., Villareal, L., and Gregory, J., "An Experimental Study of a Rotor in Axial Flight," Proceedings of the AHS Technical Specialists' Meeting for Rotorcraft Acoustics and Aerodynamics, Williamsburg, VA, October 28–30, 1997.

[39] Leishman, J. G., Han, Y. O., and Coyne, A. J., "Measurements of the Velocity and Turbulence Structure of a Rotor Tip Vortex," *AIAA Journal*, Vol. 35, (3), March 1997, pp. 477–485.

[40] Martin, P. B., and Leishman, J. G., "Trailing Vortex Measurements in the Wake of a Hovering Rotor with Various Tip Shapes," Proceedings of the American Helicopter Society 58th Annual National Forum, Montréal Canada, July 11–13, 2002.

[41] Ramasamy, M., and Leishman, J. G., "Interdependence of Diffusion and Straining of Helicopter Blade Tip Vortices," *Journal of Aircraft*, Vol. 41, (5), September 2004, pp. 1014–1024.

[42] Ramasamy, M., Johnson, B., and Leishman, J. G., "Tip Vortex Measurements Using Dual Plane Digital Particle Image Velocimetry," Proceedings of the American Helicopter Society 64th Annual National Forum, Montréal Canada, April 28–30, 2008.

[43] Mapes, P., Kent, R., and Wood, R., "DoD Helicopter Mishaps FY85-05: Findings and Recommendations," U.S. Air Force, Montréal, 2008.

[44] NTSB, "Briefs: LAX01LA283, LAX01LA304, LAX04LA285, SEA05CA173, LAX08LA198," National Transportation Safety Board, 2001, 2004, 2005, 2009.

[45] Jansen, C., Wennemers, A., and Groen, E., "FlyTact: A Tactile Display Improves a Helicopter Pilots Landing Performance in Degraded Visual Environments," *Haptics: Perception, Devices and Scenarios*, Vol. 5024, 2008, pp. 867–875.

[46] Ryerson, C. C., Haehnel, R. B., Koenig, G. G., and Moulton, M. A., "Visibility Enhancement in Rotorwash Clouds," Paper AIAA-2005-263, 43rd AIAA Aerospace Sciences Meeting and Exhibit, Reno, NV, January 10–13, 2005.

[47] "Sandblaster 2 Support of See-Through Technologies for Particulate Brownout," Task 1 Technical Report, Sponsored by Defense Advanced Research Projects Agency (DOD) Strategic Technology Office, Issued by U.S. Army Aviation and Missile Command Under Contract No. W31P4Q-07-C-0215, MRI Project No. 110565, October 31, 2007.

[48] "Sandblaster 2 Support of See-Through Technologies for Particulate Brownout," Task 5 Final Technical Report, Sponsored by Defense Advanced Research Projects

Agency (DOD) Strategic Technology Office, Issued by U.S. Army Aviation and Missile Command Under Contract No. W31P4Q-07-C-0215, MRI Project No. 110565, October 31, 2007.

[49] Wong, O. D., and Tanner, P. E., "Photogrammetric Measurements of an EH-60L Brownout Cloud," 66th Annual Forum Proceedings of the American Helicopter Society, Phoenix, AZ, May 11–13, 2010.

[50] Milluzzo, J., and Leishman, J. G., "Assessment of Rotorcraft Brownout Severity in Terms of Rotor Design Parameters," *Journal of the American Helicopter Society*, Vol. 55, (3), October, 032009, 2010.

[51] Milluzzo, J. I., "Effects of Blade Tip Shape on Rotor In-Ground-Effect Aerodynamics." Master's thesis, University of Maryland, 2012.

[52] Bagnold, R. A., *The Physics of Blown Sand and Desert Dunes*, Dover Publications, Inc., Mineola, NY, 1941.

[53] Greeley, R., and Iversen, J. D., *Wind as a Geological Process on Earth, Mars, Venus, and Titan*, Cambridge University Press, New York, NY, 1985, Chapter 3.

[54] Greeley, R., Iversen, J. D., Marshall, J. R., and Pollack, J. B., "Aeolian Saltation Threshold: The Effect of Density Ratio," *Sedimentology*, Vol. 34, (4), 1987, pp. 699–706.

[55] Leishman, J. G., "Challenges in Understanding the Fluid Dynamics of Brownout: Review and Update," Proceedings of the AHS International Meeting on Advanced

Rotorcraft Technology and Safety Operations, Omiya, Japan, November 1–3, 2010.

[56] Endres, Gunter G., and Gething, M.J., "Jane's Aircraft Recognition Guide", 5th ed. Collins, London, 2007.

[57] Ramasamy, M., and Leishman, J. G., "Benchmarking PIV with LDV for Rotor Wake Vortex Flows," AIAA Journal, Vol. 45, (11), November 2007, pp. 2622–2633.

[58] Leishman, J. G., "On Seed Particle Dynamics in Tip Vortex Flows," *Journal of Aircraft*, Vol. 33, (4), 1996, pp. 823–825.

[59] Raffel, M., Willert, C., and Kompenhans, J., "Particle Image Velocimtery: A Practical Guide," *Springer*, 1st Edition, Berlin, 1998.

[60] Willert, C. E., and Gharib, M., "Digital Particle Image Velocimetry," *Experiments in Fluids*, Vol. 10, (4), January, 1991, pp. 181–193.

[61] Huang, H., Dabiri, D., and Gharib, M., "On Errors of Digital Particle Image Velocimetry," *Measurement Science and Technology*, Vol. 8, (12), December, 1997, pp. 1427–1440.

[62] Ramasamy, M., Johnson, B., Huismann, T., and Leishman, J. G., "Digital Particle Image Velocimetry Measurements of Tip Vortex Characteristics Using an Improved Aperiodicity Correction," *Journal of the American Helicopter Society*, Vol. 54, (1), 012004, 2009.

[63] Scarano, F., "Iterative Image Deformation Methods in PIV," *Measurement Science and Technology*, Vol. 13, 2002, pp. R1–R19.

[64] Theunissen R., Scarano F., and Riethmuller, M. L., "On Improvement of PIV Image Interrogation Near Stationary Interfaces," *Experiments in Fluids*, Vol. 45, pp. 557–572.

[65] Leishman, J. G., *Principles of Helicopter Aerodynamics*, Cambridge University Press, New York, NY, 2000, Chapters 1–2.

[66] Glauert, M. B., "The Wall Jet," *Journal of Fluid Mechanics*, Vol. 1, 1956, pp. 625–643.

[67] Bakke, P., "An Experimental Investigation of a Wall Jet", *Journal of Fluid Mechanics*, Vol. 2, 1957, pp. 467–472, doi:10.1017/S0022112057000270.

[68] Schlichting, H., *Boundary-Layer Theory*, McGraw-Hill Book Company, New York, NY, 1979.

[69] Eriksson, J. G., Karlsson, R. I., and Persson, J., "An Experimental Study of a Two-Dimensional Plane Turbulent Wall Jet," *Experiments in Fluids*, Vol. 25, 1998, pp. 50–60.

[70] Haehnel, R., and Dade, W. B., "Physics of Particle Entrainment Under the Influence of an Impinging Jet," Army Science Conference Proceedings, Orlando, FL, December, 2008.

[71] Haehnel, R. B., Moulton, M. A., Wenren, W., and Steinhoff, J., "A Model to Simulate Rotorcraft-Induced Brownout," American Helicopter Society 64th Annual Forum Proceedings, Montréal, Canada, April 29–May 1, 2008.

[72] Rauleder, J., and Leishman, J. G., "Measurements of the Turbulent Flow Environment on the Ground Below a Hovering Rotor," 37th European Rotorcraft Forum, Gallarate, Italy, September 13–15, 2011.